

## ABSTRACT

Title of Document: HIERARCHICAL INTERMOLECULAR  
INTERACTION MODELS OF  
N-HETEROAROMATIC STM ADLAYER  
STRUCTURES

DIANE EVANS, DOCTOR OF PHILOSOPHY,  
2007

Directed By: PROFESSOR JANICE REUTT-ROBEY,  
DEPARTMENT OF CHEMISTRY &  
BIOCHEMISTRY

The molecular scale electronic device concept was initiated in 1974 with the semi-quantitative analysis of a hemiquinone molecule. Because of the molecule's electron donor and acceptor properties, and ability to transfer electrons along the  $\pi$ -network, it was proposed that the molecule could perform as a circuit rectifier. Many investigations of molecular scale systems have occurred since then, in particular, of organic molecules with large, fused ring systems that spontaneously self-organize after deposition onto a substrate. The directionality and molecular specificity of hydrogen bonding differentiates it from the other weak interactions, driving molecules into specific arrangements and enabling spontaneous rearrangement after addition of only a small amount of enthalpic energy. A direct application of molecular recognition through self-assembly has been the design of patterned self-assembled monolayers (SAMs) for the construction of microelectrodes and supramolecular templates. However, the intermolecular interactions

that drive ordered structures to form, including molecular chains and large aggregates, has not been well understood.

To elucidate a quantitative description of the intermolecular forces of  $\pi$  network systems of aromatics that control such features as packing density and porosity, two individual model heteroaromatic systems of 9-acridinecarboxylic acid and isonicotinic acid are investigated using both experimental and computational resources. Supported by scanning tunneling microscopy (STM) topographies, x-ray diffraction (XRD) data and x-ray photoelectron (XPS) spectra, this class of N-heteroaromatics adsorbed on Ag (111) serves as a model system to systematically investigate 2-dimensional intermolecular (2-D) interactions and their impact on forming different structural phases of molecular chain domains. To approach an understanding of the dynamics of N-heteroaromatic film growth, an intermolecular interaction model of 1-D single phase chains and clusters is performed. The model considers the anisotropy of the electrostatic force interactions to determine what charge arrangements (dipole, quadrupole, etc.) better characterize the molecular interactions. Furthermore, the competition between phase chain types is shown to be length dependent and in qualitative agreement with the coverage dependent STM structural phase composition.

HIERARCHICAL INTERMOLECULAR INTERACTION MODELS OF  
N-HETEROAROMATIC STM ADLAYER STRUCTURES

By

Diane Evans

Dissertation submitted to the Faculty of the Graduate School of the  
University of Maryland, College Park, in partial fulfillment  
of the requirements for the degree of  
Doctor of Philosophy  
2007

Advisory Committee:

Professor Janice Reutt-Robey, Department of Chemistry & Biochemistry, Chair

Professor John A. Tossell, Department of Chemistry & Biochemistry

Professor Ellen D. Williams, Department of Physics

Professor Daniel Kosov, Department of Chemistry & Biochemistry

Professor Brian Eichhorn, Department of Chemistry & Biochemistry

© Copyright by  
Diane Evans  
2007

# Dedication

To

Gilbert DePaolis, Joseph Cammarano, Thomas Cammarano, Dr. Jose Saez and  
Patricia Navarro

## Acknowledgements

I thank my dissertation advisor Professor Janice Reutt-Robey for her guidance, insight and efforts on my behalf. She has provided careful and instructive suggestions both experimentally and academically for which I am very appreciative. I also thank my co-advisor Professor Daniel Kosov for the time he has invested in my development, particularly in the modeling of chemical systems. I am indebted to all members of the dissertation committee for their time, effort and patience. In particular, I thank Professor John Tossell for his helpful discussions of quantum chemistry computations and kindly providing computer resources, Professor Ellen Williams for her enlightening dialogue at surface science seminars and readily providing access to materials and assistance at MRSEC, Professor Brian Eichhorn for representing the dean and delivering insightful graduate chemistry lectures, and Professor Anthony Stone at Cambridge, U. K. for dialogue about intermolecular interactions and its implementation and development in the computational software ORIENT. Additionally, I thank Professor Ted Einstein, who although not a member of the committee, provided guidance to a 12-state Potts model of isonicotinic acid as well as fruitful discussions of phase transitions and finite scaling behavior in preparation of the written scholarly presentation.

I thank Dr. Bill Cullen for maintaining the VT-STM at MRSEC, for technical assistance with our group's RT-STM and for helpful discussion interpreting STM images. I also

thank Dr. Peter Zavalij for resolving the crystal structure of 9-acridinecarboxylic acid dihydrate and fruitful discussions of whole-molecule disorder, and Dr. Noel Whittaker for measuring the mass spectrometry of treated 9-acridinecarboxylic acid samples. I thank Dr. Bo Xu and Mr. Chenggang Tao for producing high-quality VT-STM images, Dr. Bindu Varughese for measuring the XPS spectra and Ms. Hui Li for producing IRRAS data. I thank Mr. Byron Silvera for his assistance in tracking down electronic and circuit issues with equipment in the RT-STM laboratory, and Mr. Robert Harper and Mr. Caedmon Walters for their assistance in resolving computer system issues. Their time and effort is sincerely appreciated.

I thank as well the Chemical Physics Program director, Professor Michael Coplan, and his staff for their professionalism, assistance and good-nature. Their guidance through the program has been extremely valuable. I thank the Physics Department, the Chemistry & Biochemistry Department and Library Services for their technical assistance and kindness.

Finally, I thank colleagues Dr. Jacek Klos and Dr. Xianjie Liu for many enlightening discussions of scientific merit. Their willingness to engage in conversation and debate ideas has been a source of encouragement and inspiration.

# TABLE OF CONTENTS

Dedication.....	ii
Acknowledgements.....	iii
Table of Contents.....	v
List of Tables.....	x
List of Figures.....	xv
List of Abbreviations.....	xxi

## 1. Introduction

1.1. Self-Assembled Hydrogen Bonded Structures in Perspective.....	1
1.2. Background to Intermolecular Interaction Models of N-Heteroaromatic STM Adlayer Structures: ACA/Ag (111) and INA/Ag (111).....	3
1.3. Thesis Overview.....	5

## 2. Chain Formation and Energy Distributions of 9-Acridinecarboxylic Acid

2.1. Introduction: Molecular Chain Modeling.....	10
2.2. Theory and Methodology.....	15
2.2.1. Intermolecular Theory and Intermolecular Energy Distributions.....	15
2.2.1.1. Short-Range Energy $\Delta E_{SR}$ .....	19



2.2.1.2. Atomic Multipole Integer $L^a$ .....	21
2.2.2. Chain Model Configurations and Computational Details.....	24
2.2.3. Molecular Multipole Moment Analysis.....	28
2.2.3.1. Initial HB Motifs: Initial Monomer and Dimer Blocks .....	31
2.2.4. Chain Length Dependency.....	35
2.3. Results.....	36
2.3.1. AAAIP Atom-Atom Interactions and <i>Ab Initio</i> Dimer Calculations .....	36
2.3.1.1. Dimer Geometries.....	37
2.3.1.2. Atom-Atom Partitioning of Intermolecular Interaction Energies .....	42
2.3.1.3. $\Delta E_{SR}$ and Charge Transfer .....	45
2.3.2. MMMA Molecule-Molecule Interactions and Mesoscopic Features.....	49
2.3.2.1. Monomer Building Block Approach .....	56
2.3.2.2. Dimer Building Block Approach.....	62
2.3.3. Chain Analysis.....	67
2.4. Conclusion .....	77
3. Chain Formation, Energy Distributions and Vibrational Frequencies of Isonicotinic Acid	
3.1. Introduction: Level of Theory Strategy .....	82
3.2. Theory and Methodology.....	84
3.2.1. <i>Ab Initio</i> and Intermolecular Theory.....	84

3.2.2. Chain Model Configurations and Computational Details.....	90
3.2.3. Molecular Multipole Moment Analysis Revisited.....	94
3.2.3.1. Initial HB Motifs: Initial Monomer .....	94
3.2.4. Chain Length Dependency.....	96
3.2.5. Intra- and Intermolecular Vibrational Modes .....	96
3.3. Results.....	97
3.3.1. AAAIP Atom-Atom Interactions and Ab Initio Calculations...97	
3.3.1.1. Dimer Geometries.....	98
3.3.1.2. Short-Range Energy $\Delta E_{SR}$ .....	101
3.3.2. MMA Molecule-Molecule Interactions and Mesoscopic Features.....	103
3.3.2.1. Monomer Building Block Approach .....	111
3.3.3. Chain Analysis.....	115
3.3.4. Vibrational Spectra of INA Monomer and Dimers.....	121
3.4. Conclusion .....	135
4. Molecular and Crystal Structure of Supramolecular 9-Acridinecarboxylic Acid Dihydrate: Whole-Molecule Disorder	
4.1. Introduction: Solid State 9-Acridinecarboxylic Acid .....	140
4.2. Experimental.....	141
4.2.1. Synthesis .....	141
4.2.2. X-ray Diffraction and Crystal Structure Determination Description.....	141
4.3. DFT Computations.....	143
4.3.1. DFT Geometries.....	144

4.3.2. DFT Dipole Moments .....	145
4.4. Discussion .....	146
4.4.1. Crystal Structure .....	146
4.4.2. Comparison: Crystallographic and Computational Molecular Geometries.....	150
5. STM and XPS Data of Adlayer Structures of N-Heteroaromatics on Ag (111) Perspectives	
5.1. Introduction: Supramolecular Surface Chemistry .....	157
5.2. Experimental Materials and Methods .....	159
5.2.1. Materials .....	159
5.2.2. Scanning Tunneling Microscopy (STM) .....	160
5.2.3. X-ray Photoelectron Spectroscopy (XPS) .....	161
5.3. Experimental Results .....	161
5.3.1. STM Topographies of N-Heteroaromatics .....	161
5.3.1.1. STM Images of ACA/Ag (111) .....	162
5.3.1.2. Phase Diagram of ACA/Ag (111).....	169
5.3.1.3. STM Images of INA/Ag (111) Summary .....	170
5.3.2. XPS Spectra of N-Heteroaromatics .....	171
5.3.2.1. XPS Spectra of ACA/Ag (111).....	171
5.3.2.2. XPS Spectra of INA/Ag (111) Summary.....	174
5.4. Comparison: Experiments vs. Computations.....	175
5.4.1. Experimental ACA Results Compared to its Thermodynamically Equivalent Computational Model.....	176

5.4.2. Alternative to the Growth Mode Scenario for ACA Adlayers.....	177
5.4.3. Experimental INA Results and Comparison.....	180
5.5. Conclusion .....	180
6.0 Conclusion.....	182
 <b>Appendices</b>	
A: Historical Efforts toward Modeling of Chains.....	185
B: Atomic and Molecular Multipole Integers $L_t^a$ and $L_t^m$ .....	188
C: MMMA Error Analysis.....	195
D: Calibration of INA Vibrational Spectra.....	199
E: X-ray Diffraction Details.....	205
F: Table F.1. X-ray Diffraction Data .....	207
G: Materials Preparation Details.....	209
H: Descriptive Overview of STM and XPS.....	212
 Bibliography .....	 215

## List of Tables

**Table 2.1.** Dimer geometries are calculated from HF/6-31G(d), B3LYP/6-31G(d) and DMA computations. The helicity is measured via two dihedral angles to express the non-symmetry of the tilt. For ACA T-T dimers, the H-B length is defined as  $r(\text{O}\cdots\text{H})$ , the HB angle as  $a(\text{O}\cdots\text{HO})$  and dihedral angle both as  $d(\text{C}_2\text{C}_6^\circ\text{C}_3^\circ\text{C}_7)$  and  $d(\text{C}_7\text{C}_3^\circ\text{C}_6^\circ\text{C}_2)$ , where superscript '°' refers to the second ACA molecule and are listed accordingly in absolute values. For ACA H-T dimers, the H-B length is defined as  $r(\text{N}\cdots\text{H})$ , the HB angle as  $a(\text{N}\cdots\text{OH})$  and dihedral angle both as  $d(\text{C}_2\text{C}_6^\circ\text{C}_7^\circ\text{C}_3)$  and  $d(\text{C}_7\text{C}_3^\circ\text{C}_2^\circ\text{C}_6)$ , respectively. In the case of T-T dimer conformers, the two H-B lengths and two HB angles are shown. The carbon numbering scheme provided for the dihedral angle is according to NIST Special Publication 922, Polycyclic Aromatic Hydrocarbon Structure Index, L.C. Sander and S.A. Wise. ....39

**Table 2.2a.** Total intermolecular energies are calculated from B3LYP/6-31G(d) and AAAIP computations. From *ab initio* calculations,  $\Delta E^{\text{AB}}$  is the supermolecule interaction energy, i.e.,  $\Delta E^{\text{AB}} = E^{\text{AB}} - (E^{\text{A}} + E^{\text{B}})$  based on the total electronic energies of the dimer conformer and monomer with ZPE corrections. From the AAAIP calculations,  $E_{\text{T}}$  is the total intermolecular interaction energy (electrostatic and repulsive energies) of the dimer conformer, i.e.,  $E_{\text{T}} = E_{\text{electrostatic}} + E_{\text{repulsive}}$  up to 4<sup>th</sup> multipole moment. Since  $E_{\text{repulsive}}$  is only a few percent,  $\Delta E_{\text{LR}} \cong E_{\text{T}}$  .....46

**Table 2.2b.** Total intermolecular energies are calculated from HF/6-31G(d) and AAAIP computations. From *ab initio* calculations,  $\Delta E^{\text{AB}}$  is the supermolecule interaction energy, i.e.,  $\Delta E^{\text{AB}} = E^{\text{AB}} - (E^{\text{A}} + E^{\text{B}})$  based on the total electronic energies of the dimer conformer and monomer with ZPE corrections. From the AAAIP calculations,  $E_{\text{T}}$  is the total intermolecular interaction energy (electrostatic and repulsive energies) of the dimer conformer, i.e.,  $E_{\text{T}} = E_{\text{electrostatic}} + E_{\text{repulsive}}$  up to 4<sup>th</sup> multipole moment. Since  $E_{\text{repulsive}}$  is only a few percent,  $\Delta E_{\text{LR}} \cong E_{\text{T}}$  .....49

**Table 2.3a.** The monomer molecular multipole moments  $\ell_{j,k}^m$  of order  $j$ , component  $k$  were computed at the B3LYP/6-311G(d,p) level of theory.

They are the spherical tensor form multipole moments in atomic units (a.u.) listed  $\ell_{1,0}^m$   $\ell_{1,1c}^m$   $\ell_{1,1s}^m$ , etc. ....52

**Table 2.3b.** Molecular multipole moments for N-heteroaromatic ACA H-T and T-T dimer conformers are computed. The dimer molecular multipole moments  $\ell_{j,k}^m$  of order  $j$ , component  $k$  were computed at the B3LYP/6-31G(d) level of theory. They are the spherical tensor form multipole moments in atomic units (a.u.) of order  $j = 1, 2, 3, 4$  and are listed  $\ell_{1,0}^m$   $\ell_{1,1c}^m$   $\ell_{1,1s}^m$ , etc. ....53

**Table 2.3c.** The monomer molecular multipole moments  $\ell_{j,k}^m$  of order  $j$ , component  $k$  were computed at the HF/6-31G(d,p) level of theory. They are the spherical tensor form multipole moments in atomic units (a.u.) listed  $\ell_{1,0}^m$   $\ell_{1,1c}^m$   $\ell_{1,1s}^m$ , etc. ....54

**Table 2.3d.** Molecular multipole moments for N-heteroaromatic ACA H-T and T-T dimer conformers are computed. The dimer molecular multipole moments  $\ell_{j,k}^m$  of order  $j$ , component  $k$  were computed at the HF/6-31G(d) level of theory. They are the spherical tensor form multipole moments in atomic units (a.u.) of order  $j = 1, 2, 3, 4$  and are listed  $\ell_{1,0}^m$   $\ell_{1,1c}^m$   $\ell_{1,1s}^m$ , etc. ....55

**Table 2.4a.** Geometries for ACA H-T chains from  $n=2$  to  $n=14$  were computed, where  $n$  is the number of monomers. ....70

**Table 2.4b.** Dihedral angles for H-T chains in order of increasing rotational twist along the chain growth direction. ....71

**Table 2.5a.** Geometries for ACA T-T chains from  $n=2$  to  $n=14$  were computed, where  $n$  is the number of monomers. Hydrogen bonding occurs along odd molecular pair indices of the dihedral angle plots. ....72

**Table 2.5b.** Dihedral angles for T-T chains in order of increasing rotational twist along the chain growth direction. ....73

**Table 3.1.** Dimer geometries are calculated from HF/6-31G(d), B3LYP/6-311G(d,p) and MP2/6-31+G(d,p) computations. There is no helicity at the HF and DFT level of theory. At the MP2 level of theory, there is a non-significant tilt between the two basal planes. For INA T-T dimers, the H-B length is defined as  $r(O \cdot H)$ , the HB angle as  $a(O \cdot HO)$  and dihedral angle both as  $d(C_3C_6^{\circ}C_3^{\circ}C_6)$ , where superscript '0' refers to the second INA molecule and are listed accordingly in absolute values. For INA H-T dimers, the H-B length is defined as  $r(N \cdot H)$ , the HB angle

as  $a(N \cdots OH)$  and dihedral angle both as  $d(C_3C_6 \circ C_6 \circ C_3)$ . In the case of T-T dimer conformers, the two H-B lengths and two HB angles are shown. The carbon numbering scheme provided for the dihedral angle is according to NIST Special Publication 922, Polycyclic Aromatic Hydrocarbon Structure Index, L.C. Sander and S.A. Wise. ....99

**Table 3.2a.** Total intermolecular energies are calculated from B3LYP/6-31(d) and AAAIP computations. From DFT calculations,  $\Delta E^{AB}$  is the supermolecule interaction energy, i.e.,  $\Delta E^{AB} = E^{AB} - (E^A + E^B)$  based on the total electronic energies of the dimer conformer and monomer with ZPE corrections. From the AAAIP calculations,  $E_T$  is the total intermolecular interaction energy (electrostatic and repulsive energies) of the dimer conformer, i.e.,  $E_T = E_{\text{electrostatic}} + E_{\text{repulsive}}$  up to 4<sup>th</sup> multipole moment. Since  $E_{\text{repulsive}}$  is only a few percent,  $\Delta E_{LR} \cong E_T$  .....102

**Table 3.2b.** Total intermolecular energies are calculated from HF/6-31(d), MP2/6-31G(d,p) and AAAIP computations. From *ab initio* calculations,  $\Delta E^{AB}$  is the supermolecule interaction energy, i.e.,  $\Delta E^{AB} = E^{AB} - (E^A + E^B)$  based on the total electronic energies of the dimer conformer and monomer with ZPE corrections. From the AAAIP calculations,  $E_T$  is the total intermolecular interaction energy (electrostatic and repulsive energies) of the dimer conformer, i.e.,  $E_T = E_{\text{electrostatic}} + E_{\text{repulsive}}$  up to 4<sup>th</sup> multipole moment. Since  $E_{\text{repulsive}}$  is only a few percent,  $\Delta E_{LR} \cong E_T$  .....103

**Table 3.3a.** The monomer molecular multipole moments  $\ell_{j,k}^m$  of order  $j$ , component  $k$  were computed at the B3LYP/6-311G(d,p) level of theory. They are the spherical tensor form multipole moments in atomic units (a.u.) listed  $\ell_{1,0}^m$   $\ell_{1,1c}^m$   $\ell_{1,1s}^m$ , etc. ....105

**Table 3.3b.** Molecular multipole moments for N-heteroaromatic INA H-T and T-T dimer conformers are computed. The dimer molecular multipole moments  $\ell_{j,k}^m$  of order  $j$ , component  $k$  were computed at the B3LYP/6-311G(d,p) level of theory. They are the spherical tensor form multipole moments in atomic units (a.u.) of order  $j = 1, 2, 3, 4$  and are listed  $\ell_{1,0}^m$   $\ell_{1,1c}^m$   $\ell_{1,1s}^m$ , etc. ....106

**Table 3.3c.** The monomer molecular multipole moments  $\ell_{j,k}^m$  of order  $j$ , component  $k$  were computed at the HF/6-31G(d) level of theory. They are the spherical tensor form multipole moments in atomic units (a.u.)

listed  $\ell_{1,0}^m$   $\ell_{1,1c}^m$   $\ell_{1,1s}^m$ , etc.....107

**Table 3.3d.** Molecular multipole moments for N-heteroaromatic INA H-T and T-T dimer conformers are computed. The dimer molecular multipole moments  $\ell_{j,k}^m$  of order  $j$ , component  $k$  were computed at the HF/6-31G(d) level of theory. They are the spherical tensor form multipole moments in atomic units (a.u.) of order  $j = 1, 2, 3, 4$  and are listed  $\ell_{1,0}^m$   $\ell_{1,1c}^m$   $\ell_{1,1s}^m$ , etc.....108

**Table 3.3e.** The monomer molecular multipole moments  $\ell_{j,k}^m$  of order  $j$ , component  $k$  were computed at the MP2/6-31+G(d,p) level of theory. They are the spherical tensor form multipole moments in atomic units (a.u.) listed  $\ell_{1,0}^m$   $\ell_{1,1c}^m$   $\ell_{1,1s}^m$ , etc.....109

**Table 3.3f.** Molecular multipole moments for N-heteroaromatic INA H-T and T-T dimer conformers are computed. The dimer molecular multipole moments  $\ell_{j,k}^m$  of order  $j$ , component  $k$  were computed at the MP2/6-31+G(d,p) level of theory. They are the spherical tensor form multipole moments in atomic units (a.u.) of order  $j = 1, 2, 3, 4$  and are listed  $\ell_{1,0}^m$   $\ell_{1,1c}^m$   $\ell_{1,1s}^m$ , etc.....110

**Table 3.4.** IR active modes of INA monomers and dimers are listed. From quantum chemistry methods, two different fields of theory are used for gas phase INA: HF/6-31G(d), denoted HF, and MP2/6-31+G(d,p), denoted MP2. Frequencies from specific monomer and dimer conformer HF calculations are indicated, i.e., monomer (M), head-to-tail INA dimer (H) and tail-to-tail INA dimer (T). Frequency  $\nu_0$  is the mid-range value of the HF values for that mode, and only MP2 INA monomer frequencies are calculated. Ref<sup>a</sup> is Li, H. PhD thesis (2006) of adsorbed INA on Ag(111) in vacuum, and Ref<sup>b</sup> is P. Koczoń, *et al.* J of Molecular Structure **655** (2003), 89 of INA pellets in air. Scaling factors were used for the calculations, i.e., 0.88 (HF), 0.995 (MP2). .....123

**Table 5.1.** Crystal packing arrangement of the ordered structural phases of ACA and INA determined from STM measurements are shown. The unit cell was determined from molecularly resolved STM topography images of ordered structures. For instance, for the ACA  $\alpha$ -phase, there are 2 ACA molecules per unit cell and 8 Ag atoms per ACA molecule. The later is determined from the atomic spacing of Ag (111) and the lateral dimensions of ACA.....175

**Table B.1.** Electrostatic energies  $E(L_i^a)$  are tabulated for atomic multipole



moment integer $L_t^a$ . Energies in kJ/mol. ....	190
<b>Table D.1a.</b> The IR normal mode frequencies for a single 3-pyridine carboxylic acid molecule was calculated using GAUSSIAN 94's UHF/6-31(d) level of theory. ....	202
<b>Table D.1b.</b> The IR frequency gas phase modes for 3-pyridine carboxylic acid (niacin) are extracted from NIST Chemistry WebBook spectrum ( <a href="http://webbook.nist.gov/chemistry">http://webbook.nist.gov/chemistry</a> ). ....	203
<b>Table F.1.</b> X-ray Diffraction Data.....	207

## List of Figures

- Figure 2.1.** From the optimized geometries of H-T ACA, (a) distance 'R' between monomer backbone center to its partner monomer backbone is  $7.9 \text{ \AA}$ , while (b) distance 'R' between dimer backbone center to its neighboring dimer backbone is  $15.8 \text{ \AA}$ . For the T-T dimer, 'R' for the monomer and dimer scenario is  $9.8 \text{ \AA}$  and  $16.6 \text{ \AA}$ , respectively. ....33
- Figure 2.2.** Formation of gas phase 9-acridinecarboxylic acid dimer conformer 1 (head-to-tail) and conformer 2 (tail-to-tail) through self-association.....37
- Figure 2.3.** Optimized geometries of ACA (a)-(b) H-T and (c)-(d) T-T dimers display helical twist about the line that connects their geometric centers. In the x-y plane are the projected views onto the plane where chain growth occurs in the (b) x-direction and (d) y-direction. Views (a) and (c) are projected views at  $45^\circ$ .....40
- Figure 2.4.** Orientation of the ACA dimer basal planes from edge-on view using Gaussian optimization for (a) H-T and (c) T-T, and using Orient optimization for (b) H-T and (d) T-T conformers.....41
- Figure 2.5.** Pairwise electrostatic and repulsive energies for the ACA dimer were computed using Orient 4.5 for both (a) H-T and (c) T-T configurations with  $L^a = 4$  where atoms of one ACA molecule is labeled 1-26 and its partner is labeled 27-52. From HF/6-31G(d) computational results, (d) the ACA H-T dimer configuration is shown using GaussView where distances, angles and dihedral angles are drawn to scale and the numbering scheme is the same for both the H-T and T-T ACA dimer. The (b) absolute energy scale is kJ/mol.....44
- Figure 2.6.** The (a) normalized APT residual charge for the ACA H-T and T-T dimer conformers is shown. The H-T dimer conformer (blue) baseline is intentionally displaced. The (b) atom numbering scheme of the H-T dimer is shown and corresponds to the atoms referenced in the APT plot. The atom numbering is the same for the T-T dimer. The APT residual is the change in the charge around the atom after forming a

dimer relative to its monomeric state.....47

**Figure 2.7.** The molecular moment electrostatic energy distribution for ACA HB motifs is computed from the multipolar electrostatic energy  $\ell_{jv}^m S_{jv,kw}^m \ell_{kw}^m / R^{j+k+1}$  for pairwise molecular moments. The monomer building block is used and the fractional total electrostatic energy contribution for pairwise moments  $L^m=4$  is shown for the (a) T-T dimer and (b) H-T dimer conformer. A negative fractional total electrostatic energy signifies a repulsive electrostatic contribution. The cross-hatched area represents the molecular separation of increasing molecular orbital repulsion beyond optimized geometries. ....57

**Figure 2.8.** Displaced anti-parallel dipoles create a repulsive dipolar interaction. ....58

**Figure 2.9.** The probability density factor  $(\Theta_{m,l})^2$  plotted in angular coordinates for single electron hydrogen-like atoms. [From H. E. White, *Physical Review* **37**, 1416 (1931). Reproduced with permission.].....60

**Figure 2.10.** The molecular moment electrostatic energy distribution for the ACA dimer-dimer short chain is computed from the multipolar electrostatic energy  $\ell_{jv}^m S_{jv,kw}^m \ell_{kw}^m / R^{j+k+1}$  for pairwise molecular moments. The dimer building block is used and the fractional total electrostatic energy contribution for pairwise moments  $L_t^m=4$  is shown for the short H-T type chain. The cross-hatched area represents the dimer-dimer separation of increasing ‘molecular’ repulsion beyond optimized geometries. ....64

**Figure 2.11.** Optimized geometries of 3-, 6- and 12-monomer length ACA chains of (a)-(c) H-T type and (d)-(e) T-T type. Chains display helical twist about the ‘S’ shaped curve that connects their geometric centers. ....68

**Figure 2.12.** Average (a) twist angle and (b) HB geometries for pairwise ACA molecules along the chain growth direction. The twist angle is the averaged dihedral angle. ....73

**Figure 2.13a.** Intermolecular energy  $E_n$  for ACA chain lengths of n monomers were calculated for n=2 through n=14. ....75

**Figure 2.13b.** Intermolecular energy for ACA chain lengths of n monomers were calculated for both (a)  $\Delta E_s$  and (b)  $\Delta E_r$ . For the T-T configuration,  $\Delta E_r$  splits into  $\Delta E_{r,e}$  and  $\Delta E_{r,o}$  where the former

corresponds to an even number of monomers and for the latter to an odd number, shown as T-T,e and T-T,o respectively. The trends are for chain lengths n=2 through n=14. ....75

**Figure 3.1** The supermolecule interaction energy differences between random planar orientations about their average is shown. Of the 8 dimer configurations, 6 were above (blue) and 2 (red) were below, indicating that the directional dependence of intermolecular forces skews (uniformly distributed) random selection. All of the dimer configurations are in-plane. Units are kJ/mol above or below the configuration at 0. ....92

**Figure 3.2.** Formation of gas phase isonicotinic dimer conformer **1** (head-to-tail) and conformer **2** (tail-to-tail) through self-association. ....98

**Figure 3.3.** Optimized geometries of INA (a)-(b) H-T and (c)-(d) T-T dimers display no helical twist about the line that connects their geometric centers. ....100

**Figure 3.4.** The INA dimer multipolar electrostatic energy  $\ell_{jv}^m S_{jv,kw}^m \ell_{kw}^m / R^{j+k+1}$  for pairwise molecular moments is computed. The fractional total electrostatic energy contribution for pairwise moments  $L^m=4$  is shown for the (a) T-T dimer conformer and (b) H-T dimer conformer. A negative fractional total electrostatic energy signifies a repulsive electrostatic energy contribution. The cross-hatched area represents the molecular separation of increasing molecular orbital repulsion beyond optimized geometries. Because the flat parallel geometries required more accurate multipole moment values, the MP2 calculations were used in the T-T case. ....112

**Figure 3.5.** Optimized geometries of 3-, 6- and 12-monomer length INA chains of (a)-(c) H-T type and (d)-(e)T-T type. Chains display linearity for the H-T chain type and high curvature for the T-T chain types. ....117

**Figure 3.6a.** Intermolecular energy  $E_n$  for INA chain lengths of n monomers were calculated for n=2 through n=14. ....119

**Figure 3.6b.** Intermolecular energy for INA chain lengths of n monomers were calculated for both (a)  $\Delta E_s$  and (b)  $\Delta E_r$ . For the T-T configuration,  $\Delta E_r$  splits into  $\Delta E_{r,e}$  and  $\Delta E_{r,o}$  where the former corresponds to an even number of monomers and for the latter to an odd number, shown as T-T,e and T-T,o respectively. The trends are for chain lengths n=2 through n=14. ....119

**Figure 3.7.** IR frequencies for INA monomer and dimer conformers computed from HF *ab initio* calculations. The (a) H-T dimer compared

to the monomer shows a new mode at  $3266\text{ cm}^{-1}$ , while the **(b)** T-T dimer compared to the monomer shows a new mode at  $3337\text{ cm}^{-1}$ . The frequencies correspond to the acceptor-donor HB. The spectra was scaled specific for this system.....122

**Figure 4.1.** **(a)** Molecule 9-acridinecarboxylic acid with two water molecules labeling scheme and **(b)** superimposed molecules 9-acridinecarboxylic from the whole molecule disorder are shown. Atomic displacement ellipsoids of both (a) and (b) are shown at the 30 % probability level.142

**Figure 4.2a.** Results of the optimized molecular orbital calculation ( $\text{\AA}^{\circ}$ ) for the 9-acridinecarboxylic acid H-T dimer. ....144

**Figure 4.2b.** Results of the optimized molecular orbital calculation ( $\text{\AA}^{\circ}$ ) for the 9-acridinecarboxylic acid H-T dimer. ....145

**Figure 4.3a.** Packing diagram shown looking down the c-axis is shown. Chains of H-bonded molecules are equally directed. ....148

**Figure 4.3b.** Packing diagram shown looking down the c-axis with alternating chains of H-bonded molecules is shown. This is a plausible arrangement of consecutive chains in the 3:2 ratio of alternating chains. ....149

**Figure 4.4a.** H-T molecular chains along the a-axis direction.....153

**Figure 4.4b.** In the b-c plane, herringbone structure of ACA and water molecules form a 2-dimensional hydrogen bonding network.....153

**Figure 5.1.** STM topography scans of different areas of Ag (111) after sputtering and annealing. **(a)** Relatively "smooth" surface characterized by irregular steps and silver islands are shown, whereas **(b)** "rough" surface characterized by step bunches and a wide terrace. Image **(c)** shows a magnified image of (b), and **(d)** a further magnification revealing the "frizzled" crystallographic step indicative of thermal edge motion. The corresponding line profiles indicate monatomic free steps. ....160

**Figure 5.2.** Early ACA chain formation along the Ag (111) step edge. **(a)-(b)** ACA is seen to decorate both the upper and lower step edge indicated by the evanescent ripple and protrusions. **(c)** Some ACA molecule adsorb onto the step edge while others remain in the 2-D gas. Line profile shows damping of the ripples. ....164

**Figure 5.3.** Vicinal  $\beta$ -phase of ACA is shown on regions with narrow Ag (111) terraces. The **(a)** line profile emphasizes the dimer arrangement arranged in a zig-zag pattern, shown **(b)** magnified. ....165

<b>Figure 5.4.</b> Large terrace areas are occupied by ordered ACA adlayers forming (a) long H-T chains in the $\alpha$ -phase, and (b) ordered arrays of T-T dimers in the $\beta$ -phase. The line profiles show the molecular periodicity and minimum number of protrusions per unit cell. ....	166
<b>Figure 5.5.</b> (a) ACA islands are formed over large terraces at coverage $\theta = 0.7$ ML. The (b) step edge region is magnified, showing ACA molecules forming at both the upper and lower step. ....	167
<b>Figure 5.6.</b> The unit cells of the ordered structural phases of ACA are shown. For the (a) $\alpha$ -phase, the H-T dimer forms the unit cell, while for the (b) $\beta$ -phase, two T-T dimers (4 molecules) form the unit cell. For the (c) the vicinal $\beta$ -phase, two T-T dimers (4 molecules) form the unit cell but are less densely packed. ....	169
<b>Figure 5.7.</b> ACA phase diagram for low-index surfaces.....	170
<b>Figure 5.8.</b> Ordered phase structures of INA showing that (a) 12 orientational domains form (6-fold rotational domains and two reflection domains). Magnification of (b) boxed area I, and of (c) boxed area II are shown. Over a large terrace area, the (d) rhombic shapes of INA islands form where the H-B direction is indicated by the sharp boundaries.....	171
<b>Figure 5.9.</b> XPS core level shifts of ACA of atoms involved in acceptor-donor hydrogen bonding. ....	172
<b>Figure 5.10.</b> XPS core level shifts of INA of atoms involved in acceptor-donor hydrogen bonding. ....	174
<b>Figure B.1.</b> The cumulative atomic multipole moment $L^a$ distribution for ACA H-T and T-T conformers is displayed. The total electrostatic and repulsive energy $E$ per cumulative multipole moment $L^a$ (labeled $L$ ) is the numerical value shown for both the H-T and T-T ACA dimer. For the H-T conformer, $E(L^a = 2) \approx E(L^a = 4)$ while for the T-T conformer, $E(L^a = 1) \approx E(L^a = 4)$ . The bar graph height grows with increasing attractive energy, showing which specific $L^a$ values contribute to, or detract from, the change. Energies are in kJ/mol.....	189
<b>Figure C.1.</b> Relative potential error of ACA monomer between DFT and AAAIP, and between AAAIP and MMMA methods. ....	196
<b>Figure C.2.</b> Relative electrostatic energy error between DMA and MMMA methods of ACA HB motifs using monomer building blocks. ....	197

<b>Figure D.1.</b> IR frequency of relative intensities of <i>ab initio</i> (blue) and NIST (red) data for gas phase modes of niacin.....	200
<b>Figure D.2.</b> Low and high frequencies from <i>ab initio</i> and NIST data with comparable relative intensities are plotted against each other.....	201
<b>Figure D.3.</b> IR frequency of relative intensities of <i>ab initio</i> (blue) (after scaling) and NIST (red) data for gas phase modes of niacin. ....	204
<b>Figure H.1.</b> Electron tunnel from the negatively biased tip to the molecule on the surface. ....	213

## List of Abbreviations

AAAIIP	anisotropic atom-atom interaction potential
ACA	9-acridinecarboxylic acid
APT	atomic polar tensor
AES	auger electron spectroscopy
DFT	density functional theory
DMA	distributed multipole analysis
HB	hydrogen bond
HF	Hartree-Fock
HOMO	highest occupied molecular orbital
H-T	head-to-tail
INA	isonicotinic acid
IR	infrared
LEED	low energy electron diffraction
LUMO	lowest unoccupied molecular orbital
ML	monolayer
MMMA	molecular multipole moment analysis
MO	molecular orbital
MS	mass spectroscopy
RT	room temperature



STM	scanning tunneling microscopy
T-T	tail-to-tail
VT	variable temperature
XPS	x-ray photoelectron spectroscopy
XRD	x-ray diffraction

# Chapter 1

## Introduction

### 1.1. Self-Assembled Hydrogen Bonded Structures in Perspective

Research and development of self-assembled organic structures covers a broad range of disciplines under different scientific objectives. From investigating the molecular self-assembly of biological systems to designing self-assembled molecular scale electronics, each discipline is concerned with the interacting energies and conformations of the molecular components, both individually and collectively. Research efforts range from a bottom-up approach starting with the molecular ab initio calculations or synthesis of small monomer proteins to a top-down approach, starting with the band structure measurements or crystal nucleation via micron size contact printing, for example. As system length scales decrease and charge density delocalization increases, the path approaches a middle ground in our surface science study efforts. Self-organized aromatic molecules explored at the molecular level offer an opportunity to simultaneously investigate long-range order and stability at the mesoscopic scale.

The molecular scale electronic device concept was initiated in 1974 with the semi-quantitative analysis of a hemiquinone molecule. Because of the molecule's electron

donor and acceptor properties, and ability to transfer electrons along the  $\pi$ -network, it was proposed that the molecule could perform as a circuit rectifier[1]. In 1997, a practical molecular rectifier was claimed[2]. Investigations of other molecular scale devices such as resonant tunneling diodes[3, 4], logic devices[5] and wires[6] have been explored and are under active investigation. Organic layered material intercalated between metal oxide/insulator films have already shown good performance at optimal insulator thickness, leading to: external quantum efficiency, electroluminescence efficiency, conductivity state switching[4, 7]. These elements were developed through film fabrication, involving various stages of vapor deposition and 'self-assembly' to produce the overall layered structure[8].

Even though the physical sciences are recognized for the historical development of molecular scale electronic devices, it is ironic that molecular self-assembly is a term borrowed from biological systems, explicitly defined as “ the spontaneous association of molecules under equilibrium conditions into stable aggregates, joined by noncovalent bonds, with well-defined composition and structure”[9, 10]. The weak interaction force credited for this spontaneous association is typically 'hydrogen bonding', though there exist other noncovalent, weak bonding interactions as well, e.g., van der Waals, dipole-dipole, dispersion and  $\pi$ - $\pi$  interactions. For the purpose of understanding biological systems, the study of organic molecular self-assembly in solution has been undertaken. Synthesized cyanuric acid-melamine molecules have been observed via Rayleigh scattering to form lattice structures in solution[11] and confirmed by conventional methods after re-crystallization[10, 12]. In living systems, DNA (deoxyribonucleic acid)

provides a well-known demonstration of the ability of hydrogen bonds to affect supramolecular structure formation. The directionality and molecular specificity of hydrogen bonding differentiates it from the other weak interactions, driving molecules into specific arrangements and enabling spontaneous rearrangement after addition of only a small amount of enthalpic energy. The dynamics of hydrogen bonding between similar amino acids on a crystalline surface has been observed to form ordered structures with binding site selectivity and chiral specificity[13-15], creating a packing arrangement. A direct application of molecular recognition through self-assembly has been the design of patterned self-assembled monolayers (SAMs)[16] for the construction of microelectrodes, microcrystals[17], and microstructures of silicon. Molecular recognition and supramolecular structures remain highly active areas of research in both the solution and solid phase.

## 1.2. Background to Intermolecular Interaction Models of N-Heteroaromatic

### STM Adlayer Structures: ACA/Ag (111) and INA/Ag (111)

This thesis will focus on the hierarchical intermolecular interaction models of N-heteroaromatic STM adlayer structures of isonicotinic acid and 9-acridinecarboxylic acid to elucidate an explanation of the self-assembled molecular chain formation. Supported by XPS and XRD data, this class of N-heteroaromatics adsorbed on Ag (111) serves as a

model system to systematically investigate 2-dimensional intermolecular interactions and their impact on forming different structural phases of molecular chain domains.

There is a wide application of these N-heteroaromatic derivatives: versatility of its derivatives as fluorescence probes[18, 19], dopants in C<sub>60</sub> fullerene films[20, 21], photosensitive binding agents to DNA[22], and medicinal application[23]. Perhaps of even more significance, has been the production of acridine in the troposphere due to incomplete combustion of propane gas, diesel and coal exhaust, which in turn has turned up as particulates in the human respiratory tract[24].

Acridine derivatives, particularly functionalized acridine orange, remains as an important tool to identify DNA binding sites of the adducts formed from the fluorescence signature. These are usually performed in solution with pH and solvent dependency. Nonetheless, a current interest of acridine has been its importance in studying surface sites on inorganic oxides, not only because of its potential use as active catalysts, adsorbents and insulators, but to monitor acridine particulates. For instance, acridine adsorbed on SiO<sub>2</sub>, Al<sub>2</sub>O<sub>3</sub> and MgO solids normally found in the troposphere have been studied using time-resolved fluorescence measurements to characterize the different acridine species (neutral, hydrogen-bonded and protonated) and make atmospheric particulate matter models[24]. As in the case of our study of 9-acridinecarboxylic acid, the lone pair of the heteroatom is the effective binding site for a hydrogen donor, but in this particulate study there is usually more than one type of hydroxyl group that binds to it. Study of the surface growth of the acridine derivative in their case may not be available, although

understanding acridine intermolecular interactions is of interest[25]. To date, neither the morphology nor chain growth of adsorbed acridine or its derivatives have been investigated, except by our group at University of Maryland.

In the case of isonicotinic acid and its derivatives, XPS, STM and XAS measurements of these 2-dimensional films have been made. However, only pyridine and pyridazine and not isonicotinic were adsorbed on Ag (111) prior to our study and their orientation determined[26]. The self-assembly of molecular chains occurs predominately through intermolecular interactions, minimization of substrate interactions is important. Thus Ag (111), which offers a 9 coordination number with no exposure to second row atoms to which to bind, is the optimum choice. However, although planar chain formation of these derivatives was not investigated, the interestingly fact that pyridine undergoes a compressional phase transformation from a  $\pi$ -bonded to a more weakly bound, nitrogen-lone pair bonded species upon excitation[27] provides insight to our investigation. Monolayer adsorption of isonicotinic acid on TiO<sub>2</sub> (110) is reactive, known to deprotonate the carboxylic groups[28]. Lateral chain growth of isonicotinic acid, or its derivatives, on Ag (111) has not been studied[29].

### 1.3. Thesis Overview

Chapter 2 will discuss the intermolecular interaction model developed in a hierarchical, systematic manner to analyze chain growth of ACA. These interaction models include both the anisotropic atom-atom intermolecular potential (AAAIP) and the molecular multipole moment analysis (MMMA). Both are based on the anisotropic electrostatic potential that dictates the geometrical structure of crystal packed structures to a good approximation.

The MMMA is discussed in detail since it is a novel method developed to provide a much needed physical and intuitive description of computational results, and is a method that has a direct analogue to the atomic orbital picture for molecule-molecule interactions. Then from the AAAIP method, the intermolecular energies of n-monomer length chains are provided. These energies are length and growth mode dependent, showing a crossover for the H-T type chain at low monomer number grown via association.

Quantum chemistry calculations using both Density Field Theory and Hartree-Fock level of theory for the ACA monomer and dimer conformers are included as well. They not only provide geometrical and energetic information for these motifs, but serve as an integral part of the AAAIP and MMMA method, and provide an upper limit of the short-range energy of the ACA dimers.

Chapter 3 will discuss the results of the intermolecular interaction model for INA, analogous to Chapter 2. Some comparisons with the ACA analysis will be made as a consistency check to maintain a systematic approach, particularly in establishing initial

configurations. The AAAIP and MMMA computations, atomic orbital molecule-molecule description and chain length dependent energies will be presented. From the intermolecular energies of n-monomer length chains, a similar crossover of the H-T type chain grown via association occurs. However, an anomaly occurs at n=14 monomer length T-T type chains grown via attachment. The departure from ACA trends such as the T-T type chain preference for large n, and the multipole moment modes are discussed.

Analogous to Chapter 2, quantum chemistry calculations are performed for the monomer and dimer conformers. Now in addition to Density Field Theory and Hartree-Fock computations, the Møller-Plesset level of theory is used as well, to obtain more accurate energies, geometries and vibrational spectra of INA. This suite of INA computations will serve as a benchmark for other N-heteroaromatic systems, in particular ACA.

The infrared (IR) active vibrational mode calculations associated with inter- and intramolecular vibrations are presented and compared to our IR experimental data. By calibrating vibrational data of a similar N-heteroaromatic molecule, the HF computational results were scaled for this INA study and in very good agreement with MP2 calculations. Limitations of the MMMA method are discussed.

Chapter 4 will discuss the crystallographic compound  $C_{13}H_9NO_2 \cdot 2H_2O$  built up of 9-acridinecarboxylic acid and water molecules. This new crystal produced in our laboratory is the first for hydrogen bonded H-T acridinecarboxylic acid, and is an unusual type of crystal formation (whole molecule disorder). The acridine derivatives form linear



chains of head-to-tail hydrogen bonding networks along the a-axis and  $\pi$ - $\pi$  intermolecular bonding in the transverse directions. Diffraction data shows that the direction of the head-to-tail chains flipped randomly to form two different packings in about a 3:2 ratio, representing the case of so called whole-molecule disorder.

Density functional theory is used to compute the monomer and H-T dimer geometries, and the results are compared to the crystallographic data. Small differences plausibly attributed to electronic density shifts leading to better hydrogen bonding are discussed.

Chapter 5 will discuss the adlayer structures of N-heteroaromatics isonicotinic acid (INA) and 9-acridinecarboxylic acid (ACA) formed on Ag (111) at room temperature observed via scanning tunneling microscopy (STM) and supported with x-ray photoelectron spectroscopy (XPS). Details of the four structural phases of ACA/Ag (111) and the single structural phase of INA/Ag (111) observed are discussed. In each structural phase, domains are molecular chain arrangements with distinguishing features present in the STM topographies.

The dynamics involved during the self-assembly process are discussed in terms of the chain type computations and multipole moment analysis. The multipole moments that drive ACA and INA to form ordered structures electrostatically and predict the dynamics of these self-organized organic monolayers are consistent with the experimentally determined phase diagram.

## Chapter 2

### Chain Formation and Energy Distributions of 9-Acridinecarboxylic Acid

#### ABSTRACT

Anisotropic atom-atom intermolecular potential (AAAIP) calculations were performed for the Head-to-Tail (H-T) and Tail-to-Tail (T-T) type chains of  $n$ -monomers of 9-acridinecarboxylic acid (ACA) ranging from  $n=2$  to  $n=14$  using ORIENT, popularly known as Distributed Multipole Analysis (DMA). An alternative single dimer and dimer-dimer molecular multipole moment analysis (MMMA) dependent upon molecular electrostatic properties was performed as well for the short length chains and compared to AAAIP. Hartree-Fock (HF) and Density Functional Theory (DFT) calculations were performed for the H-T and T-T dimer conformer, as well, in part to assess the long-range electrostatic effects and assign the energy partitioning.

Comparison of *ab initio* and AAAIP calculations are in reasonable agreement with the qualitative description of the long-range electrostatic and repulsive model of these ACA dimer conformers and from the supermolecule interaction energy, revealing  $\sim 25\%$  of the dimerization energy is attributed to non-additive many-body effects brought about by

redistribution of the electron density, about half the short-range energy percentage assigned to other hydrogen bonded systems. From AAAIP and MMMA multipolar electrostatic energy analysis, long and short chain-length intermolecular features are obtained and demonstrate the cooperative features of H-T type chains, which crossover from T-T type chains at low monomer number,  $n$ . The correlation between electrostatic moments and electron orbitals suggests an explanation for these definitive features.

## 2.1. INTRODUCTION: MOLECULAR CHAIN MODELING

Assemblies of rigid aromatic molecules involving hydrogen bonding (HB) have a wealth of experimental data[20, 21, 30-33] prompting an ever-growing need for cost effective computations. Structural models of low-dimensional/disordered chemical systems are often proposed, based upon general HB features of a single dimer or of a 3D crystal structure. Vinogradov, *et al.*[34] reports that only two mechanisms are responsible for HB systems—cooperative hydrogen bonding and conjugation of a H bond with a  $\pi$ -electron system. If no further study ensued to explain the driving forces that govern the organization of these systems illustrated with structural models, precise molecular architectural design would rely heavily upon this phenomenological generality to detail a complex structure. As early as 1931, there was already a study for atomic systems

establishing unwittingly that it is atomic orbitals that govern their geometric orientation[35]. The long history of computational studies of large atomic systems has since become more definitive and expansive, leading to the emergence of highly accurate intermolecular potential methods[36-38] to reflect real systems.

With growing interest in 2-D molecular chains systems known to occur within liquid-air interfaces[39-41], liquid phase[42, 43] and thin films formed in particular from Langmuir-Blodgett techniques or vapor deposition[31, 44], computations of molecular chain formation and development of molecular models using site-site interaction methods has been applied to the study of these predominately organic systems[42, 45-53]. Often the 'site' is the location of an individual atom or bond, and can be the coordinates of any charge density region within the molecular system. By fitting *ab initio* data to a parameterized site-site interaction type potential in a perturbation type scheme[46] or by imposing a sensitivity coefficient[48], the number of coordinates is reduced to allow a more tractable site-site interaction potential that can be used in a molecular dynamics (MD) simulation or in a mean field approximation. Rowley *et al.*[48] methodically sampled the relative orientation of dimer polymorphs of ethane-ethane for latter use in MD simulations. Wurger[46] calculated the mean field approximation as a function of the lattice distortion parameter expressed in the potential and computed the three phases of ordered alkane. Boeyens *et al.*[47] as well used the Buckingham (exp-6) potential, in this case, to methodically sample only the rotation of individual monomers rather than of all coordinates from a single thermodynamically stable state to estimate the high rotation energy of crystalline pyrene before disorder occurs.

Roszak *et al.*[49] studied molecular chains of formic acid by fitting *ab initio* data to site-site interaction potential terms in a decomposition scheme that comprise the two-body potential. Initial configurations of the MD simulation were a crystalline formic acid dimer surrounded by randomly oriented formic acid molecules, and evolution of the system through isobaric incremental time produced insights to the HB motifs of formic acid dimers, trimers and complexes. Open *cis-cis* dimers were found to readily transform to 6-membered cyclic complexes, while open *cis-trans* dimers were present as chain fragments in the high pressure regime. The energy of the *cis-trans* complex was found to be 1 kcal/mol higher than the *cis-cis* isomer.

Despite the insights which these and semi-empirical methods have offered, interest in a more definitive prescription of the molecular interactions and a pictorial description of the electronic and/or orbital assign of molecules making up the chain remains. Molecular chain formation using the united-atom (UA) approach as been used to predict thermodynamic state functions, order parameters and/or molecular models for systems of polymer fluids[54], electrolytes, crystal structures and 2-D monolayer films[55]. In general, UA approximates the influence of groups of atoms or molecular fragments by treating them as single atoms and has gained popularity in molecular mechanics programs. The Gay-Berne model in the UA approach uses a Lennard-Jones (LJ) type function containing parameters that characterize the ellipsoidal shape of the pseudo-molecule together with a single-site description to reasonably predict dimer interactions and model mesoscopic behavior[56], for polar molecules particularly.

A more rigorous treatment of the assignment of atomic charges has been Bader's atoms-in-molecules (AIM) theory designed to assign atomic charges determined from the molecular electrostatic potential (MEP)[57]. MEP is computed from the electron probability distribution determined explicitly from the appropriate electronic wavefunction and has found wide application, particularly for computing the classical Coulomb effects known to be the most influential on chemical reactivity (as opposed to quantum effects) of intra- and intermolecular interactions for numerous systems[58, 59]. Although it does rely upon an *ab initio* computation of the wavefunction, MEP is found to be not strongly affected by choice of basis set nor by inclusion of electron correlation[57].

AIM together with MEP has been used to prescribe a multipole moment description of the field due to individual atoms while maintaining the overall potential. The atomic electrostatic potential (AEP) and AIM moments have been investigated by Kosov *et al.*[38], providing a multipole moment description that lends readily to an anisotropic site-site model. This partitioning method of AEP has been successful for small size systems, in part due to the assignment of multipoles as integrations over finite volumes in the context of AIM, formally avoiding convergence problems. However, similar to the AEP approach is the anisotropic atom-atom intermolecular potential (AAAIP) computed using A. J. Stone's ORIENT program. Widely known as distributed multipole analysis (DMA), it requires less computational effort and is particularly well suited for larger, more rigid systems such as large, conjugated molecular architectures inherent in photovoltaic, LED, transistor and chemical sensors application systems.

The ORIENT program uses local moments obtained from the electron density of molecules. Charges and multipoles are distributed solely on the basis of the relative positions of the basis functions with respect to the nuclei, and local moments of  $L^{\text{th}}$  order depend strictly upon the  $L^{\text{th}}$  spherical tensor representation and the atomic density also of  $L^{\text{th}}$  order[60]. This implementation of distributed multipole moments does not present a ‘shape’ convergence problem and has been used extensively with reasonable success[61-63].

Specifically, AAAIP is a perturbative method that relies upon how the electron density eventually is distributed among the multipole moments centered at atomic nuclei of each atom. By summing all two-body (i.e., two-atom) interactions perturbatively in terms of energy  $E^{(n)}$ , the intermolecular energy is obtained. The zero order term,  $E^{(0)}$  is the electrostatic energy of a point charge positioned at the atom due to the uniform field imposed by a second atom. It itself is expressed as an expansion of pairwise multipole moments undergoing coulomb attraction (or repulsion). The first order term,  $E^{(1)}$  is the multipolar electrostatic energy of an atom due the non-uniform electric field imposed by a second atom. The next higher order terms correspond to induction and dispersion that occur between the excited and ground states, and between different excited states, respectively. They are the coulomb interactions between relaxed and perturbed multipole moments. In this study, AAAIP will include only the dominant  $E^{(0)}$  and  $E^{(1)}$  terms, along with the repulsion energy of an atom due to a second atom[64].

The caveat of this description is that the partitioning of this non-additive repulsion term into additive terms depends upon the chemical structure of the interacting molecules[65], and the perturbative series of energy terms due to different contributing interactions types, e.g., induction, charge-transfer and electrostatics, are treated separately. Since the multipolar electrostatic and repulsion energy comprise most of the molecular interaction energy for small organic dimers[66] and aromatics[67], the intermolecular model of these interaction types treated perturbatively can still provide reasonable results. This AAAIP model up to first order terms will be used in this paper for the study of intermolecular interactions of the N-heteroaromatic molecule 9-acridine carboxylic acid (ACA). An excellent discussion of AAAIP including a larger number of interaction types and series treatment beyond the scope of this thesis is written by A. J. Stone[66] and others[65].

## 2.2. THEORY AND METHODOLOGY

### 2.2.1. Intermolecular Theory and Interatomic Energy Distributions

The AAAIP intermolecular potential model for this ACA chain study is the multipole expansion up to first order (in energy), including repulsion. It is the sum of the coulomb point charge, multipolar electrostatic and repulsive interaction energy terms between



pairwise atoms. Explicitly, the atom-atom multipolar electrostatic energy  $E_{\text{electrostatic}}$  is the perturbative expression up to  $\ell = 4$  of the electrostatic energy of an atom due to the non-uniform field imposed by a second atom, i.e.,

$$E_{\text{electrostatic}} = \sum_{l,m} (-1)^m \hat{Q}_{l,-m} V_{lm} \quad (2.1a)$$

$$V_{lm} = [(2l+1)!!]^{-1} R_{lm} \nabla V_{\mathbf{r}=0} \quad (2.1b)$$

where  $\hat{Q}_{l,-m}$  are the spherical-tensor forms of the multipole moments and  $R_{lm}$  are the regular spherical harmonics. Expressing potential  $V_{lm}$  as the second expansion of multipole moments, the multipole electrostatic energy becomes,

$$\begin{aligned} E_{\text{electrostatic}}(\mathbf{R}) &= \sum_{m_1 m_2 m} (-1)^l \left( \frac{(2l_1 + 2l_2 + 1)!}{(2l_1)!(2l_2)!} \right)^{1/2} \hat{Q}_{l_1 m_1}^{A(G)} \hat{Q}_{l_2 m_2}^{B(G)} I_{l_1+l_2, m}(\mathbf{R}) \begin{pmatrix} l_1 & l_2 & l_1+l_2 \\ m_1 & m_2 & m \end{pmatrix} \\ &= \sum_{l_1, l_2} \sum_{\kappa_1 \kappa_2} \begin{pmatrix} l_1+l_2 \\ l_1 \end{pmatrix} \hat{Q}_{l_1 \kappa_1}^A \hat{Q}_{l_2 \kappa_2}^B S_{l_1 l_2 l_1+l_2}^{\kappa_1 \kappa_2} R^{-l_1-l_2-1} \end{aligned} \quad (2.2)$$

and,

$$S_{l_1 l_2 j}^{\kappa_1 \kappa_2} = \mathbf{i}^{-l_1-l_2-j} \begin{bmatrix} l_1 & l_2 & j \\ 0 & 0 & 0 \end{bmatrix}^{-1} \sum_{m_1 m_2 m} [D_{m_1 \kappa_1}^{l_1}(\Omega_1)]^* [D_{m_2 \kappa_2}^{l_2}(\Omega_2)]^* C_{jm}(\theta, \varphi) \begin{pmatrix} l_1 & l_2 & j \\ m_1 & m_2 & m \end{pmatrix} \quad (2.3)$$

where  $\hat{Q}_{l\kappa_1}^A$  is the multipolar moments of order  $l$  component  $\kappa_1$  of site 'A',  $C_{jm}$  is the renormalized spherical harmonic component,  $D_{m\kappa}^l$  is the Wigner rotation matrix and the (3 x 2) matrix is the Wigner 3j symbol. The exchange-repulsion energy term is the atom-atom modified Born-Mayer potential,

$$E_{er} = C e^{-\alpha(R-\rho)} \quad (2.4)$$

that models the exchange-repulsion interaction adequately for closed electron shell systems[65, 68]and for prediction of crystalline properties including elastic constants[69]. In this expression,  $C$ ,  $\alpha$  and  $\rho$  are parameters of individual atoms and are often fit to the density obtained in monomer calculations[70]. In this study,  $\alpha \approx 25 \text{ bohr}^{-1}$  and  $C \approx 0.001 \text{ hartree}$ , giving a sharp slope lending the name 'pseudo-hard-sphere potential'. Multipolar electrostatic potentials have been found to be more sensitive to orientation than to short distance forces[66], therefore not requiring a more extensive exchange-repulsion model. In fact, dimer geometries, and cyclic or planar structures of  $n$ -monomers, have long been known to be determined primarily by long-range electrostatic forces[71, 72].

Multipole moments provide information as to how the electronic charge is distributed, providing insight as to the bonding nature of certain constituents, particularly for the molecular multipole moment. For instance, two adjacent and symmetric  $p_x$  ( $p_y$ ) atomic orbitals form a molecular  $\pi_u$  orbital, whereas two adjacent and antisymmetric  $p_x$  ( $p_y$ )

atomic orbitals form a molecular  $\pi_g^*$  orbital, where the latter in the united atom limit is the atomic  $d_{xz}$  orbital. The d-orbital has the same electron probability distribution as the quadrupole moment. By rotating the basal plane of a system relative to another component, such as benzene, the two most adjacent p orbitals in the separate atom limit can be chosen to be either symmetric or antisymmetric[73], forming a  $d_{xz}$  orbital in the united atom limit. It is well known that the electrostatic quadrupole moment is the  $\ell=2$  moment, and that quadrupole moments are the leading terms of rotated pi systems that govern their geometric shape. These affects would have more significance when considering short-range order, however in the case of long-range order, the largest energy contribution is the electrostatic monopole energy term and thus the quadrupole contribute is negligibly. It is interesting to note that the functional form of the  $\ell=2$  moment is similar to the functional form for the electron distribution of the d-orbital for hydrogenic atoms.

It has been shown that there is a correlation between the atomic and molecular moments of small molecules[74]. From orbital information (natural atomic orbitals), atomic and molecular properties have been calculated. One such property is the multipole moments[75-77]. However, the actual correlation between atomic and molecular multipoles has been rather vague and difficult. One important difference is probably due to the different convergence radii used for atomic and molecular systems.

From *ab initio* calculations, inclusion of the intermolecular energy of a system of molecules is not determined explicitly by the summation of electrostatic and exchange-

repulsion terms, but rather deduced from the total energy (supermolecule) wavefunction of the system. It is well known that Hartree-Fock (HF) and Density Functional Theory (DFT) with moderate basis sets can provide reasonable geometries of small molecular clusters[78, 79]. Using these chemistry models, ACA dimer conformers are shown to be stable gas phase clusters having geometries consistent with hydrogen bonded (HB) system features. Subsequently, the supermolecule energy is widely used to deduce the supermolecule intermolecular energy based upon reasonably good *ab initio* calculations.

#### 2.2.1.1. Short-Range Energy $\Delta E_{\text{SR}}$

The supermolecule interaction energy,  $\Delta E^{\text{AB}}$  of the dimer is the intermolecular energy deduced from the supermolecule energy,  $E^{\text{AB}}$  and the electronic energies of the two non-interacting molecules,  $E^{\text{A}}$  and  $E^{\text{B}}$ . This approximation of the interaction energy is,

$$\Delta E^{\text{AB}} = E^{\text{AB}} - (E^{\text{A}} + E^{\text{B}}) \quad (2.5)$$

where  $E^{\alpha}$  is the electronic energy for given  $\alpha$  structure, i.e., dimer or monomer structure[80], from computational *ab initio* single point energies of the optimized geometries. Using a simple approach for assigning the long- and short-range energy contributions of the supermolecule interaction energy of this intermolecular hydrogen bonded dimer, the technique reveals an upper limit that differs by approximately 50% obtained by other methods for dissimilar hydrogen-bonded systems[81]. In fact, these N-

heteroaromatic dimers have been observed to be non-planar, rotated oligomers in the condensed phase[30]. To determine the long range electrostatic energy contribution to the supermolecule interaction energy of the dimer, the potential energy due to one of the monomers would be evaluated throughout the charge region of its dimer partner. Since the charge assignment depends upon the model chosen, the complexity of the field charge-interaction can vary.

Using AAAIP, the long-range electrostatic energy contribution to the intermolecular energy is obtained by summing over orientationally dependent pairwise atomic multipole moments. Since hydrogen bonding (HB) occurs within these ACA molecular dimers and is a mechanism for which networks of similar structure occur[82], the treatment of HB in this energy assignment approach justifies further explanation.

The long-range effects of hydrogen bonding (HB) are predominantly electrostatic, where significant attractive interaction occurs between the hydrogen atom attached to an electronegative atom and a second electronegative atom. A complete HB model would include charge-transfer and induction effects, however, these effects are known to contribute much less to the total energy compared to the Coulomb term. In this particular application of AAAIP, the hard-sphere radii model is used in addition to the pairwise atomic multipole moment terms. Reasonably good predictions of the geometries of small hydrogen bonded systems are known to occur so long as the Van der Waals radii are not too different from the hard-sphere radii[66]. Thus long-range effects of HB for the ACA

dimers are adequately captured by atomic multipole moment treatment of the molecular system.

The long-range energy contribution,  $\Delta E_{\text{LR}}$ , is explicitly the pairwise atomic multipole moments summation with no charge-transfer or induction effects. The short-range interaction energies are thus defined as

$$\Delta E_{\text{SR}} = \Delta E^{\text{AB}} - \Delta E_{\text{LR}} \quad (2.6)$$

analogous to A.V. Morozov, *et al.* is deduction of short-range order energy terms for chain-length dependent cooperativity[81]. From the supermolecule interaction energy of an ACA dimer conformer, as well as the electrostatic interaction energy, an upper bound on the short-range contributions of a single dimer due to electron redistribution is estimated. However, because *ab initio* computations of longer chains are more expensive, an alternative to describing electron charge redistribution for any chain length may be to find the *change* in the charge density modes described by AAAIP. For the ACA dimer, charge redistribution is known from the atomic polar tensor (APT) of the total electronic density.

#### 2.2.1.2. Atomic Multipole Integer $L^a$

Reasonable results from configuration to configuration are inherent in the framework of the atomic multipolar electrostatic interactions. From the electrostatic interaction terms in the expansion series alone, the relative error decreases as the order of the cumulative moments increases for overall compact systems. This is because the next higher atomic moment energy term contributes a smaller proportion to the already evaluated sum due to the  $1/R^{\ell+1}$  dependence. Errors due to the orbital configurations alone are often ignored; it is intuitive that more disperse orbital configurations (d, f, etc.) can produce larger errors than more compact orbital configurations at a moderately small intermolecular separation, particularly if most of the charge resides within these modes.

In fact, from AAAIP calculations using ORIENT4.5, the cumulative atomic multipole moment distribution of electrostatic and repulsive energies are computed by summing over all (j,k) pairwise atomic multipole moments  $\hat{Q}_{l_j^{\kappa_j}}^j \hat{Q}_{l_k^{\kappa_k}}^k$  interactions. For all  $\ell^{\text{th}}$  order atomic multiple moment integers of the  $j^{\text{th}}$  and  $k^{\text{th}}$  atoms of different molecules without regard to the  $\kappa^{\text{th}}$  component, i.e.  $l_j^a$  and  $l_k^a$ , the energies are computed according to their cumulative atomic multipole moment integer,  $L^a$ . It is worth mentioning that the term ‘cumulative’ means that  $L^a$  includes all multipole moment integers less than its maximum value, i.e.,

$$L^a \geq l_j^a + l_k^a, \quad \forall j \neq k. \quad (2.7)$$

(This is not to be confused with the summation over *all* pairwise interactions (Eq 2.2).)

These  $L^a$  terms are used to determine the relative strength of local (atomic) orbital modes via  $E(L^a)$ .

By defining

$$L_{\max}^a = \ell_j^a + \ell_k^a, \quad \forall j \neq k \quad (2.8)$$

we can see that  $L^a$  values range from 0 to  $L_{\max}^a$ . For instance, for a two atom interaction whose only pair of  $\ell^{\text{th}}$  order atomic multipole moment is 0 or 1, i.e.,  $(l^1 = 0, l^2 = 0)$ ,  $(l^1 = 0, l^2 = 1)$ ,  $(l^1 = 1, l^2 = 0)$ ,  $(l^1 = 1, l^2 = 1)$  or  $(l^1 = 1, l^2 = 1)$ , then  $L^a = \{0,1,2\}$  and  $L_{\max}^a = 2$ . From this, the dipole-dipole orbital interaction would be one of three modes that describe the electrostatic interaction outside the charge region, and the highest order since  $L^a = L_{\max}^a$ .

Cumulative atomic multipole moment,  $L^a$  is a manifestation of the multipole moment expansion of (generally) two well-spaced atoms. It is not a physical description of the molecule as a whole per se, but rather a mathematical expression of the sum of  $\ell^{\text{th}}$  order expansion terms of the charge distribution of both *atoms*. Of course, the distance between atomic centers is less than the radius of convergence.



### 2.2.2. Chain Model Configurations and Computational Details

Quantifying molecular chain-length structure features is of interest to predict molecular chain formation. However when optimizing such systems, the task becomes daunting since the number of ensembles of such systems increase with chain length. The complexity of assigning quantitative information to initial chain-length structures has resulted in an "averaging" of the many energetically stable stereoisomer chains after sampling phase space, all having the same n-conformer types for a particular molecule[83, 84], leaving the reader with less insight to details of particular configuration paths the ensemble may have followed, e.g., the cooperative effect and fragmentation. By choosing local characteristics in initial configurations such as monomer-monomer geometries, as well as long-range features, all consistent with experimental data, a more specific patterning can be obtained to give meaningful results without resorting to the need for a full statistical treatment. Using a novel approach for studying ACA n-monomer length conformer chains, the order of multipole moment terms that contribute strongly to the electrostatic energy as well as the preferred chain-length types can be determined. To our knowledge, no such approach has been taken previously.

Initial configurations of the ORIENT4.5 optimization were 1-D arrays of in-plane ACA dimers. The fact that dimers often form while in the gas phase[34, 85] suggests that dimer-(cluster)<sub>n</sub> is a reasonable starting geometry for optimization for an associated, non-dilute phase. By modeling the initial configuration in a linear fashion found to occur in 2-D ribbons[30] or 1-D chains[31], and tuned to the intermolecular geometries from dimer

*ab initio* calculations, parameters for n-monomer length chains can be found.

Furthermore, these parameters should correlate to 3D crystalline structure parameters.

Since optimization is often sensitive to initial conditions, the coordinates chosen are described below. In lieu of a computationally expensive, full statistical treatment of ACA clusters, select ACA dimer configurations that were likely to form H-T and T-T bonding were optimized. The selection was based on our results of a related N-heteroaromatic dimer molecules where a moderate sampling of phase space was performed. Initial ACA chain configurations were comprised of n-ACA monomers arranged in a stamp-like fashion, making a linear chain with relative repetitive coordinates chosen to replicate the ACA dimer. The geometries were intentionally offset from the corresponding dimer values to avoid being trapped in a local minimum during optimization.

For H-T type chains of n-monomers, there were n/2 replicas of a H-T dimer with each monomer oriented to its nearest neighbor with similar HB features as two ACA molecules have within the H-T dimer and lying flat within the plane. Corresponding dimer values are written in parenthesis. Each monomer was rotated in the plane at  $\alpha(\text{N}\cdots\text{H}-\text{O}) \approx 167^\circ$  ( $162.9^\circ$ ) and approximately  $8 \text{ \AA}$  ( $7.9 \text{ \AA}$ ) from its neighbor with a HB length  $r(\text{N}\cdots\text{H}) \approx 2 \text{ \AA}$  ( $2.0 \text{ \AA}$ ). In the case of T-T type chains of n-monomers, there were n/2 replicas of the T-T dimer each monomer also oriented to its nearest neighbor with similar HB features as two ACA molecules have within the parent T-T dimer type, with

every other monomer lying flat within the plane while its dimer partner lies out-of-the-plane at approximately  $98^\circ$  ( $69.5^\circ$ ). Within the T-T type chain, each monomer was approximately  $12 \text{ \AA}$  ( $9.8 \text{ \AA}$ ) from its neighbor with HB length  $r(\text{O}\cdots\text{H}) \approx 4 \text{ \AA}$  ( $1.8 \text{ \AA}$ ) at the carboxylic acid dimer tails and carbon hydrogens within  $\approx 8 \text{ \AA}$  of each other. These initial configurations for both H-T and T-T type chains were a repetitive, linear 1-D array, where each monomer was oriented to have slightly offset HB lengths and angles from each other.

Thus these initial configurations for both H-T and T-T type chains were a repetitive, linear 1-D array where each monomer was weakly hydrogen bonded to its neighbor, having slightly off-set HB lengths and angles from their respectively optimized parent dimer results and/or having weak hydrogen bonds to the neighboring fused ring  $\pi$  system. This offset was selected to allow optimization to occur without being trapped within a local minimum. There were no fixed parameters during optimization of the chains. The fact that dimers often form while in the gas phase suggests that dimer-dimer interactions are the next cluster arrangement to consider.

To compute the electrostatic and repulsive energy terms to a given order, the atomic pairwise electrostatic and repulsive energies are calculated. Our pairwise sites are chosen as any two atomic positions throughout the molecular structure in which atomic multipole moments  $\hat{Q}_{l_j^{\kappa_j}}^j$  and  $\hat{Q}_{l_k^{\kappa_k}}^k$  are assigned, representing the  $\ell^{\text{th}}$  order multipole moment integer of the  $j^{\text{th}}$  and  $k^{\text{th}}$  atoms of two different ACA molecules. By carefully choosing the

initial chain-like configuration, features of the optimized structure can be obtained that characterize the n-monomer structure without resorting to an extensive ensemble distribution often used in Monte Carlo simulations. During optimization of an n-monomer chain, there were no fixed parameters while stepping-through variation of 6n redundant coordinates to find the lowest intermolecular energy. These 6 coordinates correspond to the center of mass and Euler angles for a rigid molecule.

The computations were performed using Orient4.5 in conjunction with GDMA and Gaussian03. The wavefunction and single point energy of a single ACA monomer were obtained at the B3LYP/6-311G(d,p) level of theory using Gaussian03. The atomic multipole moments were then extracted from the wavefunction using GDMA software. Using the atomic multipole moments obtained from of a single monomer, Orient4.5 was used to optimize the molecular arrangement of any initial configuration by calculating pairwise atomic multipole moment  $\hat{Q}_{l_j^a k_j}^j$ ,  $\hat{Q}_{l_k^a k_k}^k$  interactions for all  $\ell^{\text{th}}$  order moment integers of atom 'j' ( $\ell_j^a$ ) and all  $\ell^{\text{th}}$  order moment integers of atom 'k' ( $\ell_k^a$ ).

From *ab initio* calculations, the wavefunctions, single point energies and geometries of a single ACA monomer and both ACA dimer conformers, i.e., Head-Tail (H-T) and Tail-Tail (T-T), were obtained at the HF/6-31G(d) level of theory using Gaussian03. For these same molecules, *ab initio* calculations were also performed but at the B3LYP/6-31G(d) level of theory using Gaussian03. For a single ACA molecule, the same node cluster produced the wavefunction, single point energy and geometries at the

B3LYP/6-311G(d,p) level of theory using Gaussian03. The AAAIP geometries and energies using ORIENT4.5 were computed as well.

### 2.2.3. Molecular Multipole Moment Analysis

Until now in this study, only atomic (local) moments and pairwise atomic multipole moment electrostatic interactions have been considered. For quantifying molecular orbitals particularly for structures in the mesoscopic regime, a more coarse grained approach is required. This methodology is similar to the atomic moment analysis and obtains the electrostatic energy distribution of pairwise *molecular* multipole moments for molecules and dimer conformers. The method as well applies to the electrostatic energy distribution of pairwise *dimer* multipole moments for dimer motifs and larger clusters. This non-local approach to multipole analysis is the molecular multipole moment analysis (MMMA).

In MMMA, molecular multipole moment tensors are not different for the same type of molecule, only their orientation within the cluster. Different  $\ell^{\text{th}}$  molecular moments from different molecules are involved in electrostatic calculation, requiring nonetheless that indices be specified. Thus, molecular multipole moments  $\hat{Q}_{i_j^m \kappa_j}^j$ ,  $\hat{Q}_{i_k^m \kappa_k}^k$  represent the  $\ell^{\text{th}}$  order multipole moment integer of the  $j^{\text{th}}$  and  $k^{\text{th}}$  ACA molecules, computed directly from the total molecular (or dimer) electronic density. Both dimers and dimer-dimer molecular moment analysis for both conformer types was determined via pairwise

multipolar electrostatic interactions separated by a characteristic distance ‘R’. Since repulsive energy terms are a minor fraction (few percent) of the total energy compared to the electrostatic energies, they have not been included in MMMA and the intermolecular energy can be approximated as,

$$E_{\text{electrostatic}}(\mathbf{R}) = \sum_{l_j^m l_k^m} \sum_{\kappa_j \kappa_k} \binom{l_j^m + l_k^m}{l_j^m} \hat{Q}_{l_j^m \kappa_j}^j \hat{Q}_{l_k^m \kappa_k}^k S_{l_j^m l_k^m l_j^m + l_k^m}^{\kappa_j \kappa_k} R^{-l_j^m - l_k^m - 1} \quad (2.9)$$

Since MMMA is similar in structure to atomic multipole moment analysis, there is an analogue to several parameters defined previously. With MMMA, the cumulative molecular multipole moment distribution of electrostatic and repulsive energies is also obtained by summing over all pairwise molecular multipole moments interactions.

This analogue to the cumulative atomic multipole moment integer,  $L^a$  exists for MMMA. For all  $\ell^{\text{th}}$  order molecular multiple moment integers of the  $j^{\text{th}}$  and  $k^{\text{th}}$  molecule without regard to the  $\ell^{\text{th}}$  component  $\kappa$ , denoted  $\ell_j^m$  and  $\ell_k^m$ , the energies are computed according to their cumulative molecular multipole moment integer,  $L^m$ . As before,

$$L^m \geq \ell_j^m + \ell_k^m, \quad \forall j \neq k \quad (2.10)$$

and

$$\mathbf{L}_{\max}^m = \ell_j^m + \ell_k^m \quad \forall j \neq k \quad (2.11)$$

Even for dimers, the number of molecular multipole moment pairs is far less the number of atomic multipole moment pairs, especially when the number of atoms in a single monomer is moderate, as in the case of ACA. One approach is to ignore the directional dependence. If the individual  $\kappa$  components were not considered but only the magnitude of the  $\ell^{\text{th}}$  order multipole moment, then the directional dependence is averaged out and an approximation of the direction of the lobe is given, i.e.,

$$Q_{l^m} = \sqrt{\sum_{\kappa} (\hat{Q}_{l^m \kappa})^2} \quad (2.12a)$$

Furthermore, if the direction of the two lobes of the interacting pairwise multipole moments is ignored, then there is no 'S' tensor. In that case, the molecular multipolar electrostatic interaction,  $E_{\text{electrostatic}}$ , i.e.,

$$E_{\text{electrostatic}}(\mathbf{R}) = \sum_{l_j, l_k} Q_{l_j^m}^j Q_{l_k^m}^k / R^{-l_j^m - l_k^m - 1} \quad (2.12b)$$

is much easier to compute. However, directional dependence can be shown to be important for even small dimer molecules.

By choosing suitable multipole moment tensors that characterize a monomer or aggregate, the MMMA method can determine the anisotropic monomer-monomer potential or anisotropic aggregate-aggregate potential, respectively. This provides a direct, physical interpretation of intermolecular electrostatic features and molecular orbital interpretation.

#### 2.2.3.1. Initial HB Motifs: Initial Monomer and Dimer Blocks

To adapt AAAIP methodology to MMMA applications,  $\ell_j^m$ ,  $\ell_k^m$  and  $\mathcal{S}_{l_j^m l_k^m l_j^m + l_k^m}^{\kappa_j \kappa_k}$  must be parameterized as a function of  $\ell_j^a$ ,  $\ell_k^a$  and  $\mathcal{S}_{l_j^a l_k^a}^{\kappa_j \kappa_k}$  terms. The complexity of the task can be circumvented by introducing 'united atoms' with a known orientational dependence. The united atoms contain the molecular electrostatic moments of any desired molecular or atomic cluster obtained from *ab initio* methods to find the electrostatic properties of even larger clusters. This cost effective computational method is implemented using ORIENT4.5 software.

In this study, ACA H-T and T-T dimers and ACA 4-monomer short chains are the clusters of interest in obtaining electrostatic properties. Electrostatic moment ensembles form units (or blocks) from which to build these hydrogen bonding dimer and short



chains. Monomer units are used to build dimer motifs, and dimer units are used to build 4-monomer short chains. For the monomer block, the electrostatic moments of a single frozen ACA molecule are employed. For the dimer building block, the electrostatic moments of a frozen ACA dimer (in either H-T or T-T arrangement ) are employed.

In the case of the monomer building block, the position and orientation of the units are important parameters in forming a HB motif. The molecular multipole moments of a single ACA along with orientation and position parameters are used to compute the multipolar electrostatic interactions between two ACA molecules to form a dimer. This is analogous to forming the molecular interaction between two united atoms and summing over the pairwise atomic multipole moment electrostatic interactions. For different dimer conformers, the global axis system of each monomer is different. By maintaining the same local axis system for each monomer and changing only its relative orientation to the global system, the new molecular multipole moments for each dimer conformer is obtained. The origin of each molecule's local axis system is the center of its electronic charge. Then for a distance 'R' between the two molecule's local axis system and two sets of molecular multipole moments, the molecular multipole electrostatic energy to form a dimer conformer via MMMA is obtained.

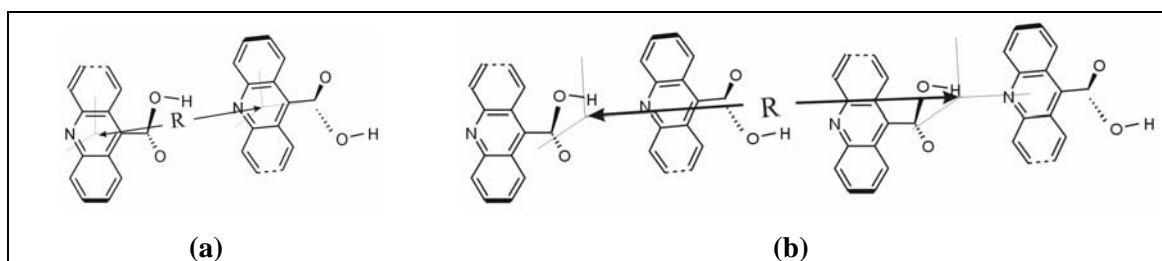


**Figure 2.1.** From the optimized geometries of H-T ACA, **(a)** distance 'R' between monomer backbone center to its partner monomer backbone is  $7.9 \text{ \AA}$ , while **(b)** distance 'R' between dimer backbone center to its neighboring dimer backbone is  $15.8 \text{ \AA}$ . For the T-T dimer, 'R' for the monomer and dimer scenario is  $9.8 \text{ \AA}$  and  $16.6 \text{ \AA}$ , respectively.

The distance 'R' between dimer partners was not arbitrarily selected but rather the measured distance from the monomer molecular backbone center to its partner's monomer backbone center determined from *ab initio* dimer calculations (Figure 2.1). For the ACA H-T HB motif  $R \approx 7.9 \text{ \AA}$ , and for the ACA T-T HB motif  $R \approx 9.8 \text{ \AA}$ . From the optimum intermolecular distance 'R' and optimum global axis coordinate system of each molecule, paired order moments of the ACA molecule and its dimer partner at the new axis configuration form the corresponding molecular moments. Thus the electrostatic interaction energy due to two (possibly different) static electron density distribution modes can be found and the pairwise summation of all molecular multipole electrostatic interactions (Eq 2.9) is straightforward.

A similar approach can be obtained for dimer building blocks (Figure 2.1). Here the molecular multipole moments assignment and the multipolar electrostatic interaction energy represents the charge distribution of a *pair* of ACA dimers positioned apart by a distance ‘R’ equal to the displacement between from one dimer molecular backbone center to the next nearest ‘expected’ dimer molecular backbone center. Here, an individual dimer cannot associate nor dissociate and so the molecular moments are in one fixed frame. Since the pairwise molecular moments represent two dimers that *can* associate with each other, their ‘inter-dimer’ distance must be even further apart. Thus for a *pair* of ACA H-T dimers,  $R \approx 2 \times 7.9 \text{ \AA} = 15.8 \text{ \AA}$ , since for a single ACA H-T dimer  $R \approx 7.9 \text{ \AA}$ . In the case of a pair of ACA T-T dimers, the determination of R is slightly different. For a single ACA T-T dimer,  $R \approx 9.8 \text{ \AA}$ , and the distance between adjacent molecules not involved in the O··HO bonding is  $R \approx 6.8 \text{ \AA}$ , making the distance between pairs of ACA T-T dimers  $R \approx 9.8 + 6.8 = 16.6 \text{ \AA}$ . These computations yield energies of 4 associated ACA molecules forming a 4-monomer short chain, i.e., dimer-dimer pairs.

In addition to the wavefunction, geometries and single point energies obtained from *ab initio* HF and B3LYP model chemistries for the ACA monomer and dimer units, the molecular electrostatic moments were computed as well. The electrostatic moments and wavefunction were used to determine the molecular multipole moment tensor for the MMA analysis and provide wavefunction coefficients for the ORIENT4.5 program.

To validate the MMMA approach, relative errors of the electrostatic potential of a single ACA molecule between *ab initio* and AAAIP and between AAAIP and MMMA calculations were performed. The multipolar electrostatic potential  $E_{\text{electrostatic}}$ , i.e.,

$$E_{\text{electrostatic}}(\mathbf{R}) = \sum_{l_j} \sum_{\kappa_j} \hat{Q}_{l_j \kappa_j}^j R^{-l_j-1} \quad (2.13)$$

was computed for both AAAIP and MMMA in addition to *ab initio* electrostatic potentials. For both the monomer and dimer units, molecular moments were computed both with the HF and B3LYP chemistry models.

#### 2.2.4. Chain Length Dependency

From the AAAIP computation using ORIENT4.5, the chain length dependent energies were computed for H-T and T-T type chains. Chain length dependency was computed for two energies  $\Delta E_r(n)$  and  $\Delta E_s(n)$ , similar to Karpfen's chain length analysis of cyclic and linear chains but with a different interpretation of  $\Delta E_r(n)$  for linear chains, i.e.,

$$\Delta E_r(n) = E_n - E_{n-1}, \quad n \geq 2 \quad (2.14a)$$

$$\Delta E_s(n) = E_n / (n - 1), \quad n \geq 2 \quad (2.14b)$$

that characterize chain growth.  $\Delta E_r$  is the energy due to the attachment of a monomer to an already formed chain.  $\Delta E_s(n)$  is the average energy due to the insertion of a monomer anywhere and gives equal weight to bulk and edge association.

Explicitly, from the additive pairwise intermolecular energies, E-repetitive energy  $\Delta E_r(n)$  is the difference in energy between chains that differ in length by only one monomer for a given length while E-scale energy  $\Delta E_s(n)$  is the average intermolecular energy of chain per monomer for a given length. A decrease in the total interaction energy indicates the cooperative effect. The attractiveness of  $\Delta E_r(n)$  and  $\Delta E_s(n)$  is that it provides a quantitative method to track the dynamics of a chain growth system.  $E_n$ , on the other hand, provides no dynamical information but the most energetically favorable n-monomer length chains representative of a thermodynamically, stable system .

## 2.3. RESULTS

### 2.3.1. AAAIP Atom-Atom Interactions and *ab initio* Dimer Calculations

From *ab initio* and AAAIP calculations, the ACA H-T and ACA T-T dimer conformers were confirmed to be stable, brought about by self-association confirming previous

experimental models (Figure 2.2). For the *ab initio* computations, optimized structures and non-imaginary frequency modes were the criteria used to determine stability from a starting geometry. For the AAAIP computation, optimized molecular orientation and non-imaginary frequency modes were the criteria used for ORIENT4.5, providing details as well to the relative strengths of intermolecular interactions.

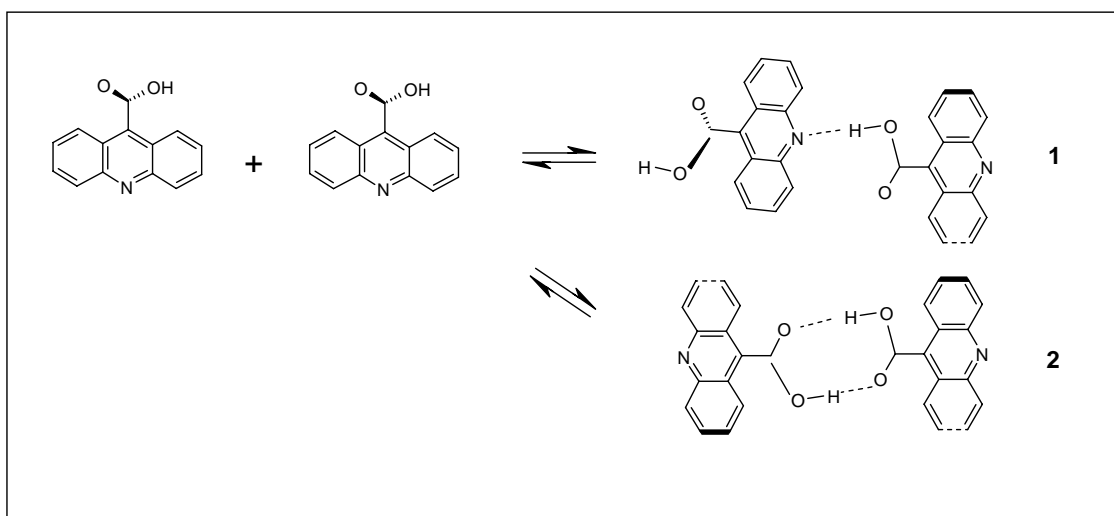


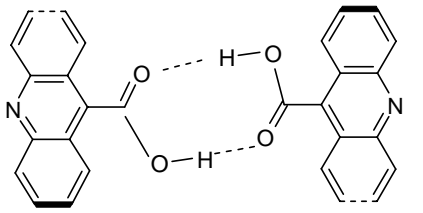
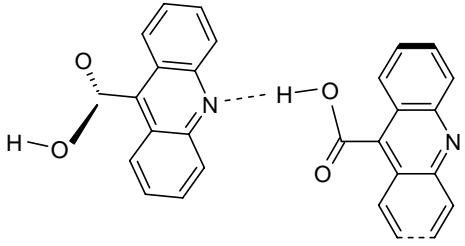
**Figure 2.2.** Formation of gas phase 9-acridinecarboxylic acid dimer conformer **1** (head-to-tail) and conformer **2** (tail-to-tail) through self-association.

#### 2.3.1.1. Dimer Geometries

*Ab initio* calculations for both ACA HB dimer motifs were performed, and at two different levels of theory and compared to the AAAIP generated dimers. Both HF and DFT *ab initio*, and ORIENT computational methods produced similar ACA dimer structures that showed strong HB features and a pronounced twist of the relative aromatic

planes for both the H-T and T-T conformers (Figure 2.3). The hydrogen bonding geometries for these HB motifs are similar for all three methods (Table 2.1).

**Table 2.1.** Dimer geometries are calculated from HF/6-31G(d), B3LYP/6-31G(d) and DMA computations. The helicity is measured via two dihedral angles to express the non-symmetry of the tilt. For ACA T-T dimers, the H-B length is defined as  $r(\text{O}\cdots\text{H})$ , the HB angle as  $a(\text{O}\cdots\text{HO})$  and dihedral angle both as  $d(\text{C}_2\text{C}_6^\circ\text{C}_3^\circ\text{C}_7)$  and  $d(\text{C}_7\text{C}_3^\circ\text{C}_6^\circ\text{C}_2)$ , where superscript '°' refers to the second ACA molecule and are listed accordingly in absolute values. For ACA H-T dimers, the H-B length is defined as  $r(\text{N}\cdots\text{H})$ , the HB angle as  $a(\text{N}\cdots\text{OH})$  and dihedral angle both as  $d(\text{C}_2\text{C}_6^\circ\text{C}_7^\circ\text{C}_3)$  and  $d(\text{C}_7\text{C}_3^\circ\text{C}_2^\circ\text{C}_6)$ , respectively. In the case of T-T dimer conformers, the two H-B lengths and two HB angles are shown. The carbon numbering scheme provided for the dihedral angle is according to NIST Special Publication 922, Polycyclic Aromatic Hydrocarbon Structure Index, L.C. Sander and S.A. Wise.

N-Heteroaromatic Dimer Species	H-B Length (Å)			H-B Angle (deg.)			Dihedral Angle (deg.)		
	HF	DFT	AAAIP	HF	DFT	AAAIP	HF	DFT	AAAIP
	1.83480	1.68728	1.85854	175.338	178.524	177.277	69.469	85.584	82.689
	1.83480	1.68753	1.85854	175.338	178.646	177.277	69.184	86.387	84.811
	1.98982	1.81445	2.00324	162.890	164.053	158.236	76.154	65.508	81.659
							62.551	52.682	68.438



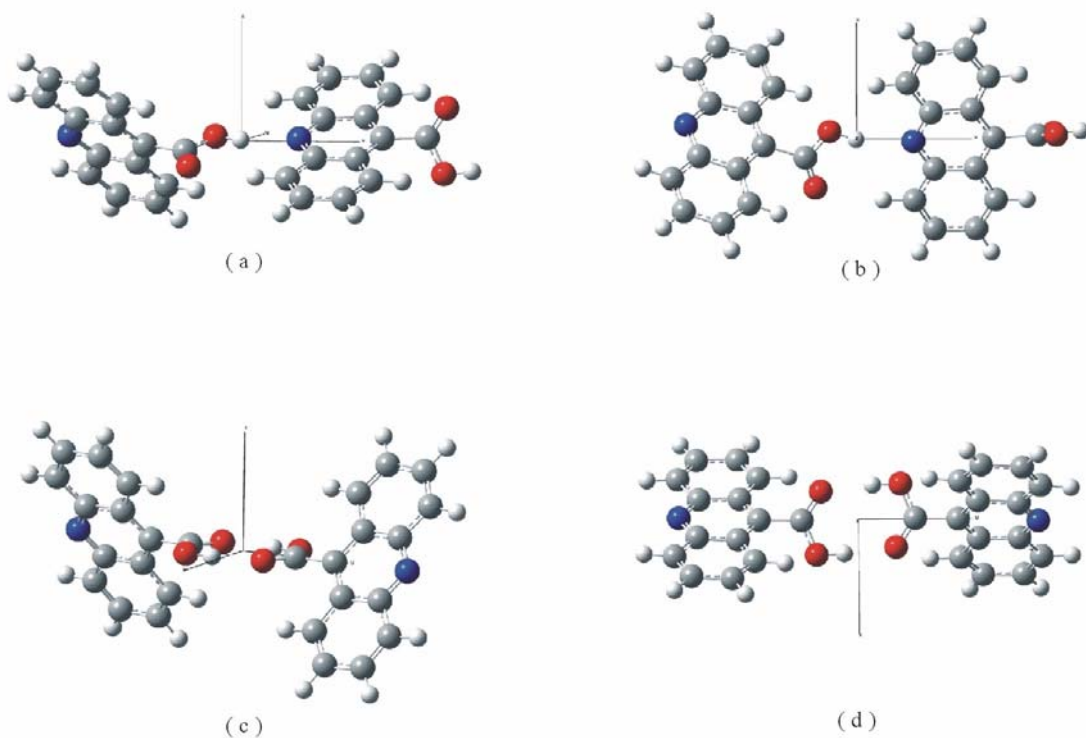


**Figure 2.3.** Optimized geometries of ACA (a)-(b) H-T and (c)-(d) T-T dimers display helical twist about the line that connects their geometric centers. In the x-y plane are the projected views onto the plane where chain growth occurs in the (b) x-direction and (d) y-direction. Views (a) and (c) are projected views at 45°.

The HF and AAAIP HB lengths for H-T and T-T conformers are in good agreement.

Since HF bond lengths are characteristically underestimated by as much as a few tenths of an angstrom[86], this suggests that the atomic charge distribution in the HF calculation is similar to that in the AAAIP multipole moment distribution. This would not be expected since the AAAIP calculation relies on a wavefunction produced from an *ab initio* computation at a level of theory having electron correlation and a larger basis set.

A flaw in concluding similar charge distributions for HF and AAAIP is however apparent when the amount of helical twist is observed. In the case of the H-T conformer, the HF

and ORIENT4.5 dihedral angles differ by  $\approx 5^\circ$  while for T-T conformers they differ by  $\approx 13^\circ$  (Figure 2.4).

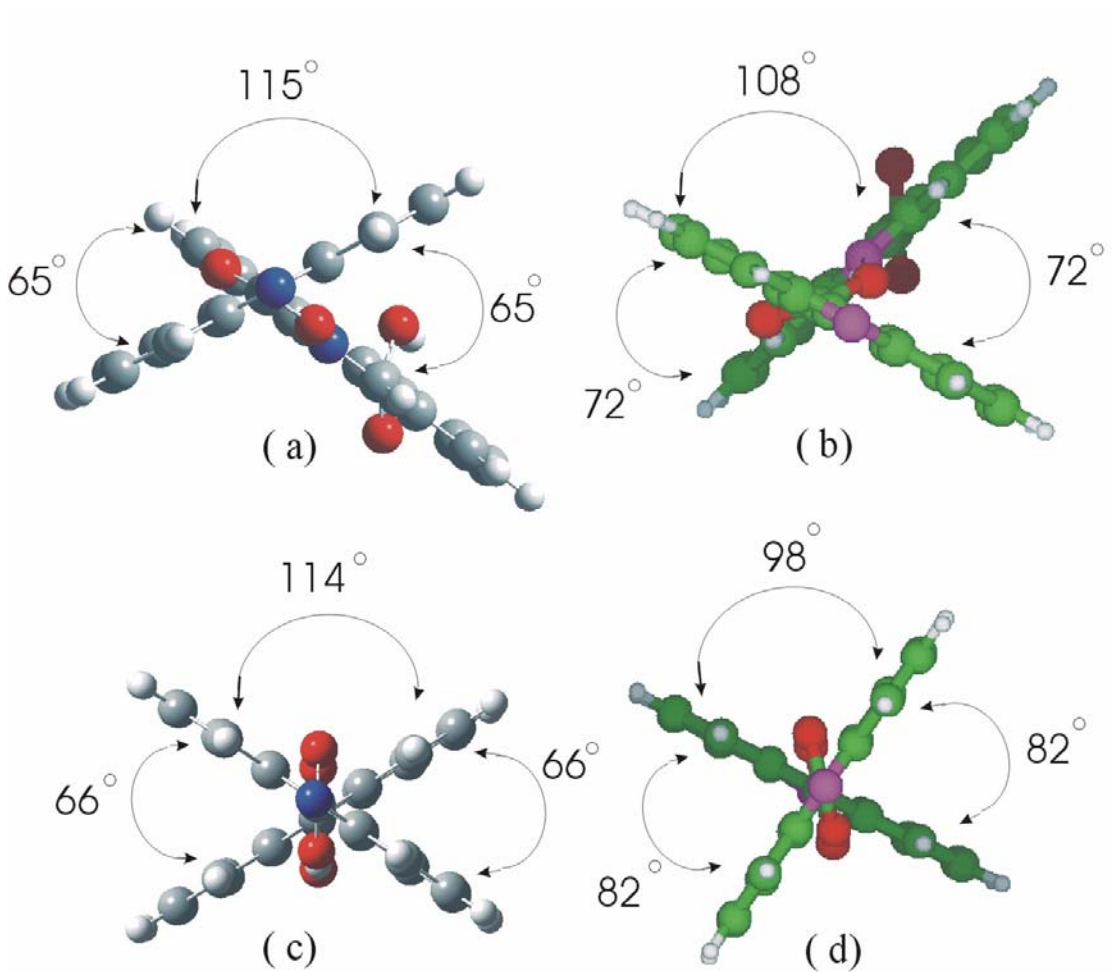


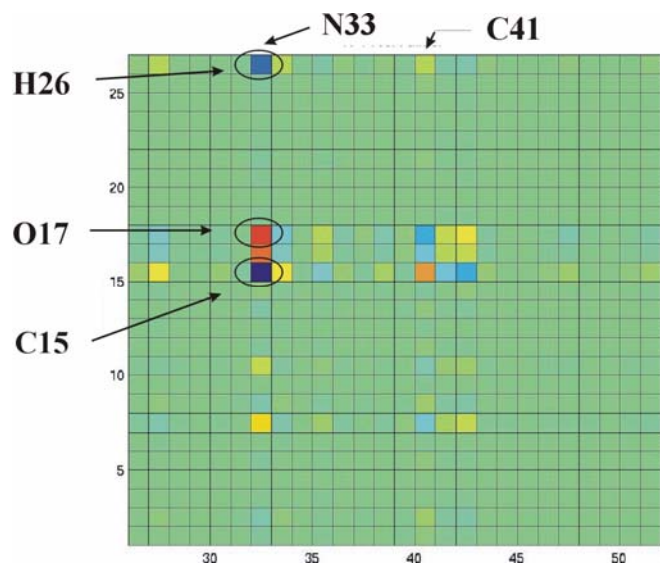
**Figure 2.4.** Orientation of the ACA dimer basal planes from edge-on view using Gaussian optimization for (a) H-T and (c) T-T, and using Orient optimization for (b) H-T and (d) T-T conformers.

DFT ACA dimer calculations further underestimate the HB length by a few tenths of an Angstrom compared to the HF calculation. It has been observed that DFT calculations have difficulty correctly predicting energies for systems with very localized or very delocalized electron density distributions[78] and for optimizing systems with  $\pi$ -conjugated substituents, such as that due to the rotational barrier around the C(sp<sup>2</sup>)-C(aryl) bond[79]. In the case of DFT heat of formation calculations for some systems, such as trimethylaluminum Al(CH<sub>3</sub>)<sub>3</sub>, the difference from experimental results is  $\approx 57\%$ . For some of these computations, more expensive basis sets have been used, however the energy accuracy has only been about 1 kcal/mol better over smaller basis sets. In our case of ACA dimers, the system does not have a floppy backbone and contains no heavy atoms. Thus the DFT dimer energy error, even with a moderate basis set, is assumed to be less severe and that larger differences existing between dihedral angles calculated from the DFT and HF computation may be attributed to rotation of the carboxylic acid about the C-C bond during optimization. For the H-T case, the dihedral angle decreases  $\approx 13^\circ$  from both the HF and ORIENT4.5 computation, while for the T-T case, the dihedral angle is very close to the AAAIP values.

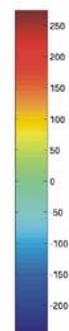
### 2.3.1.2 Atom-Atom Partitioning of Intermolecular Interaction Energies

From the ORIENT4.5 calculation, the atomic multipole moments were computed for the ACA monomer and ACA dimer conformers. The strength of the electrostatic and repulsive intermolecular energies per pair of atoms is shown in a 2-D color coded display

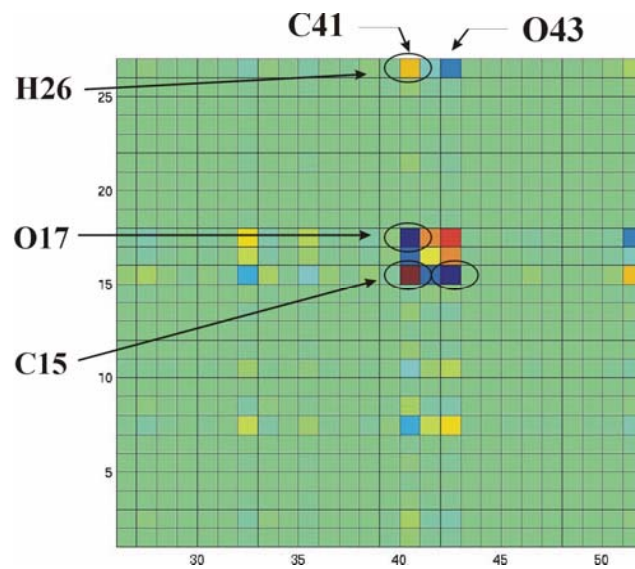
(Figure 2.5) for both dimer conformers up to  $L^a = 4$ . The total energy  $E(L^a)$  only changes  $\approx 5\%$  as  $L^a$  goes from  $3 \rightarrow 4$  for both H-T and T-T ACA conformers. Near the multipole moment order cut-off, both attractive and repulsive contributions occur in the higher moment terms.



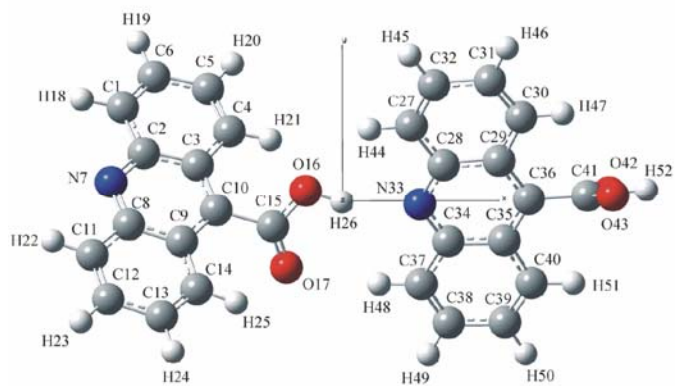
(a)



(b)



(c)



(d)

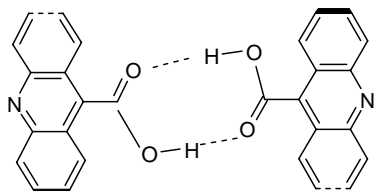
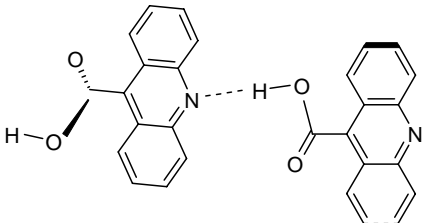
**Figure 2.5.** Pairwise electrostatic and repulsive energies for the ACA dimer were computed using Orient 4.5 for both (a) H-T and (c) T-T configurations with  $L^a = 4$  where atoms of one ACA molecule is labeled 1-26 and its partner is labeled 27-52. From HF/6-31G(d) computational results, (d) the ACA H-T dimer configuration is shown using GaussView where distances, angles and dihedral angles are drawn to scale and the numbering scheme is the same for both the H-T and T-T ACA dimer. The (b) absolute energy scale is kJ/mol.

In the 2-D color display (Figure 2.5), the green color signifies a range of mild attractive and repulsive forces considered as neutral to relative atom-atom strengths belonging to different molecules. Blue (red) signifies attractive (repulsive) forces, while yellow signifies a weak attractive force. For the H-T ACA dimer, a strong interaction is between nitrogen and hydroxyl hydrogen N33-H26 as expected through hydrogen bonding, but only second to that between nitrogen and carboxyl carbon N33-C15. The atoms in the dimer conformer are balanced by a strong repulsive atom-atom interaction between nitrogen and carbonyl carbon N33-O17. Long-range electrostatic interaction between individual atoms is evident between carboxyl carbon and hydroxyl hydrogen C41-H26.

For the T-T ACA dimer, the strongest atom-atom interaction is between carbonyl oxygen and carboxyl carbon O17-C41 and a moderately strong interaction is between carbonyl oxygen and hydroxyl hydrogen O17-H52. The subordinate attractive interaction strength for hydrogen bonding occurs as well for the T-T as the H-T conformer. A strong repulsive interaction occurs between the carbonyl oxygens O17-O43, second to interactions between carboxyl carbons C15-C41. The symmetry of the T-T dimer conformer provides a doubling of the strength of O-H atom-atom interaction type, contributing to the overall increase in dimer energy compared to the H-T conformer.

### 2.3.1.3. $\Delta E_{SR}$ and Charge Transfer

The total intermolecular energy calculated from the DFT and AAAIP methods shows that the values differ significantly enough to capture the short-range energy between the two ACA monomers (Table 2.2a).

N-Heteroaromatic Dimer Species	Intermolecular Energy (kJ/mol)	
	DFT	AAAIP
	-75.7562	-57.1594
	-51.4152	-40.5911

**Table 2.2a.** Total intermolecular energies are calculated from B3LYP/6-31G(d) and AAAIP computations. From *ab initio* calculations,  $\Delta E^{AB}$  is the supermolecule interaction energy, i.e.,  $\Delta E^{AB} = E^{AB} - (E^A + E^B)$  based on the total electronic energies of the dimer conformer and monomer with ZPE corrections. From the AAAIP calculations,  $E_T$  is the total intermolecular interaction energy ( electrostatic and repulsive energies ) of the dimer conformer, i.e.,  $E_T = E_{\text{electrostatic}} + E_{\text{repulsive}}$  up to 4<sup>th</sup> multipole moment. Since  $E_{\text{repulsive}}$  is only a few percent,  $\Delta E_{\text{LR}} \cong E_T$ .

From the atomic polar tensor (APT)[74] and atomic hard-sphere radii, a coarse grain electron density distribution difference was computed based on this charge partitioning scheme of APT charges in a hard sphere radius of van der Waal volume  $\sim \pi R_{\text{van der Waal}}^3$  where maximum changes occur along the HB direction of the hydroxyl atoms for both

conformer types. The largest residual charge for the H-T dimer is at the vicinity of the hydroxyl hydrogen (Atom Number 52), while for the T-T dimer is equal between both hydroxyl hydrogens (Atom Number 26, 52). This means that after dimer formation, there is *less* electron charge at the hydroxyl hydrogens and has redistributed elsewhere within the dimer (Figure 2.6). This leads us to conclude that the total energy  $E_T$  difference between the DFT and the AAAIP calculation is an upper limit on the amount of energy due to short-range effects, attributed predominately to electron correlation and charge density redistribution, the latter brought about by local shifting of charge to other nearby atoms. This is confirmed by the APT residual calculation. It is interesting to note that unlike the T-T dimer, the H-T residual charge shows small fluctuations among most of the aromatic atoms (Figure 2.6).

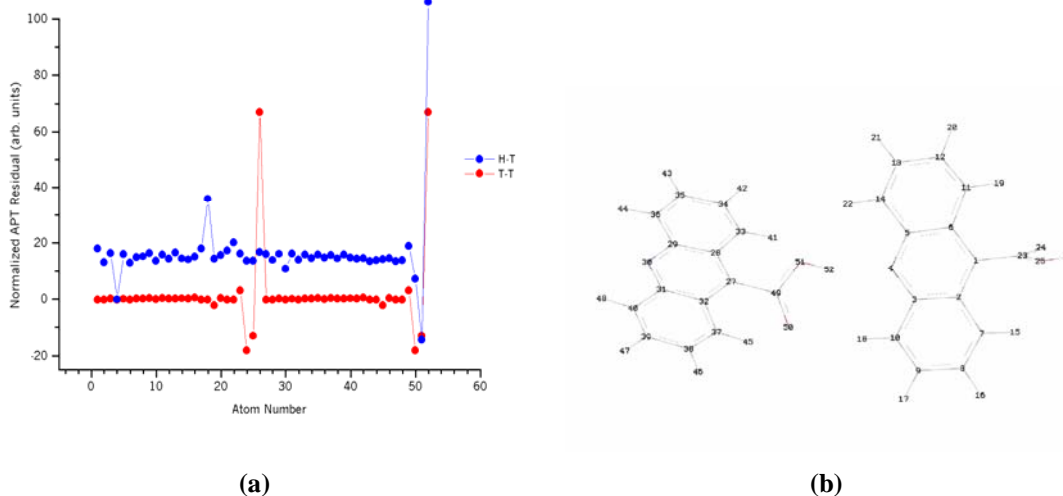


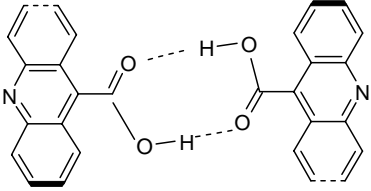
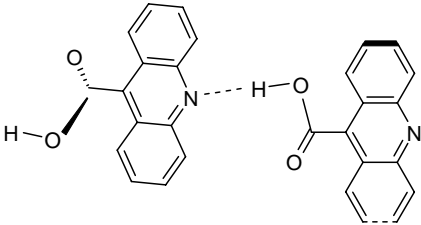
**Figure 2.6.** The (a) normalized APT residual charge for the ACA H-T and T-T dimer conformers is shown. The H-T dimer conformer (blue) baseline is intentionally displaced. The (b) atom numbering scheme of the H-T dimer is shown and corresponds to the atoms referenced in the APT plot. The atom numbering is the same for the T-T dimer. The APT residual is the change in the charge around the atom after forming a dimer relative to its monomeric state.



By definition of short-range energy  $\Delta E_{\text{SR}}$  (Eq 2.6) and calculation of the interaction energies (Table 2.2a), the short range energy values are easily tabulated[87]:

$$\Delta E_{\text{SR}} |^{\text{T-T}} \approx 24 \%, \quad \Delta E_{\text{SR}} |^{\text{H-T}} \approx 21 \%$$
 of the total supermolecule interaction energy.

Although DMA computation of  $E_{\text{T}}$  includes a hard sphere repulsion term, the contribution is negligible and  $E_{\text{T}} \sim E_{\text{LR}}$ , characterized by the intermolecular Coulomb interactions. With roughly  $0.2 \text{ \AA}$  error in the HB length of the *ab initio* calculation, this would account for roughly a 10 % error in the interaction energy  $E_{\text{T}}$ , and thus only a 10% error in  $\Delta E^{\text{AB}}$ . Since  $E_{\text{LR}}$  does not contain long-range dispersion nor induction effects, and higher order multipoles are ignored,  $\Delta E_{\text{LR}}$  is underestimated. Thus,  $\Delta E_{\text{SR}}$  is an upper limit on the short-range values of the individual ACA HB motifs. For completeness, the total intermolecular energy calculated from the HF and AAAIP methods are shown in Table 2.2b.

N-Heteroaromatic Dimer Species	Intermolecular Energy (kJ/mol)	
	HF	AAAIP
	-57.8529	-57.1594
	-35.2972	-40.5911

**Table 2.2b.** Total intermolecular energies are calculated from HF/6-31G(d) and AAAIP computations. From *ab initio* calculations,  $\Delta E^{AB}$  is the supermolecule interaction energy, i.e.,  $\Delta E^{AB} = E^{AB} - (E^A + E^B)$  based on the total electronic energies of the dimer conformer and monomer with ZPE corrections. From the AAAIP calculations,  $E_T$  is the total intermolecular interaction energy (electrostatic and repulsive energies) of the dimer conformer, i.e.,  $E_T = E_{\text{electrostatic}} + E_{\text{repulsive}}$  up to 4<sup>th</sup> multipole moment. Since  $E_{\text{repulsive}}$  is only a few percent,  $\Delta E_{LR} \cong E_T$ .

### 2.3.2. MMMA Molecule-Molecule Interactions and Mesoscopic Features

For ACA dimers, atomic pairwise electrostatic interactions and their orbital distribution have been considered using AAAIP. The atomic moments correlate directly with the charge of the atomic orbitals, and the intermolecular energies up to the fourth order of multipole moments converge to within  $\approx 5\%$  ( $\Delta E(L^a) \approx 0.05$  at  $L^a = 4$ ). Although the AAAIP intermolecular interaction energies have predicted ACA dimer geometries very well, there is a need for obtaining moment distribution information over larger atomic

regions. For characterizing larger clusters however, a more coarse grained approach is required to obtain electrostatic interactions and their *molecular* distribution. This alternative approach for describing multipole moments of entire molecules and the pairwise multipolar electrostatic interactions between them is MMMA.

MMMA depends upon the electrostatic properties resulting from *ab initio* computations, found to be sensitive to the level of theory used. Multipolar moments for both HF and DFT were computed and are in relatively fair agreement for ACA H-T dimers and relatively good agreement for ACA monomer multipole moments, for the latter up to third order. For ACA T-T dimer multipole moments, the agreement is poor. At each level of theory, the monomer (and dimer) was optimized, suggesting that the differences in the multipole moments are due to differences in the calculated electronic density of non-identical geometries. Only the DFT electrostatic moments were used in the MMMA analysis.

An error analysis of MMMA shows excellent agreement with DMA for ACA monomers at intermolecular separations of  $15 \text{ \AA}$  or higher. For ACA H-T dimers, the agreement is reasonable for dimer separations of  $28 \text{ \AA}$  or higher. At shorter distances, the molecular orbital repulsion increases and the charge is no longer well separated from the region of interest.

The total molecular electronic density resulting from B3LYP/6-311G(d,p) calculations were used to compute the monomer multipole moments (Table 2.3a), and the total dimer electronic density from B3LYP/6-31G(d) calculations used to compute the dimer multipole moments (Table 2.3b). A HF/6-31G(d) level of theory calculations were also used to produce monomer (Table 2.3c) and dimer multipole moments (Table 2.3d).

**Table 2.3a.** The monomer molecular multipole moments  $\ell_{j,k}^m$  of order  $j$ , component  $k$  were computed at the B3LYP/6-311G(d,p) level of theory. They are the spherical tensor form multipole moments in atomic units (a.u.) listed  $\ell_{1,0}^m$   $\ell_{1,1c}^m$   $\ell_{1,1s}^m$ , etc.

$j$	B3LYP/6-311G(d,p) $\ell_{j,k}^m$ (a.u.)				
1	.34509877	.31891264	.39118010		
2	-13.316531	-2.9891792	5.5138759	6.6524927	4.8741401
3	-37.672378	-12.164221	-13.339603	-55.684500	-44.138228
	-61.424119	-82.838396			
4	-3587.0098	159.75508	-473.79181	-4108.5983	278.26366
	143.98640	-468.25717	289.05191	-577.86412	

**Table 2.3b.** Molecular multipole moments for N-heteroaromatic ACA H-T and T-T dimer conformers are computed. The dimer molecular multipole moments  $\ell_{j,k}^m$  of order  $j$ , component  $k$  were computed at the B3LYP/6-31G(d) level of theory. They are the spherical tensor form multipole moments in atomic units (a.u.) of order  $j = 1, 2, 3, 4$  and are listed  $\ell_{1,0}^m$   $\ell_{1,1c}^m$   $\ell_{1,1s}^m$ , etc.

$j$	H-T $\ell_{j,k}^m$ (a.u.)					T-T $\ell_{j,k}^m$ (a.u.)				
1	.67215033	-1.798232	.45405046			-.000196593	-.000393185	.017811296		
2	-14.472432	-11.017714	-2.0095499	-6.1221541	-3.7435671	-.86546870	.52133761	-.012998049	-12.090628	-.006305985
3	-244.80655	234.91771	-3.3355244	308.34167	-732.38377	.19214979	-.21349488	-8.9643776	-.25150840	1198.8886
	-187.31118	-10.591583				-.21146092	14.669504			
4	5764.9835	4048.5738	392.60441	-10126.337	692.64664	3785.8447	-212.35587	-2.0838102	-5640.8712	.17146550
	-3891.6789	-1869.8825	-1970.4448	-2609.6821		22.483085	-1.9879644	-4723.3337	-3.4675582	

**Table 2.3c.** The monomer molecular multipole moments  $\ell_{j,k}^m$  of order  $j$ , component  $k$  were computed at the HF/6-31G(d,p) level of theory. They are the spherical tensor form multipole moments in atomic units (a.u.) listed  $\ell_{1,0}^m$   $\ell_{1,1c}^m$   $\ell_{1,1s}^m$ , etc.

$j$	HF/6-31G(d,p) $\ell_{j,k}^m$ (a.u.)				
1	.45731388	-.30464001	.40356543		
2	-15.119598	3.0436028	6.9482940	7.4301898	-4.4005477
3	-47.154483	10.581624	-19.092618	-68.204452	44.985470
	55.385773	-81.813729			
4	1870.4754	-151.19560	-562.10373	-3115.9876	-200.08605
	-130.96811	-578.42493	290.62151	514.82643	

**Table 2.3d.** Molecular multipole moments for N-heteroaromatic ACA H-T and T-T dimer conformers are computed. The dimer molecular multipole moments  $\ell_{j,k}^m$  of order  $j$ , component  $k$  were computed at the HF/6-31G(d) level of theory. They are the spherical tensor form multipole moments in atomic units (a.u.) of order  $j = 1, 2, 3, 4$  and are listed  $\ell_{1,0}^m$   $\ell_{1,1c}^m$   $\ell_{1,1s}^m$ , etc.

$j$	H-T $\ell_{j,k}^m$ (a.u.)					T-T $\ell_{j,k}^m$ (a.u.)				
1	-32909614	1.5841045	.43340823			.02142860	.00000000	.00000000		
2	-12.807201	-20.432935	-2.0512467	-3.3464824	.82955868	20.427162	.00000000	.00000000	.096977717	-.16961811
3	157.16196	-292.37587	21.944231	-221.01905	963.98244	-4.7182357	.00000000	.00000000	-24.052088	-1229.9658
	181.97916	-38.861187				.00000000	.00000000			
4	6583.2142	6520.7715	432.15235	-10938.606	-126.94738	3213.3300	.00000000	.00000000	-35155.308	-536.62185
	-5848.9658	-2272.5869	-1456.9898	1710.5924		.00000000	.00000000	-672.37692	-8.6430254	



### 2.3.2.1. Monomer Building Block Approach

The monomer multipole moments were used to compute the electrostatic energies of the monomer building block, and of thus larger ensembles. From the moment terms listed (Table 2.3a), the quadrupole moment magnitude  $|Q_2|$  is nearly a factor of 30 larger than the dipole moment magnitude  $|Q_1|$ . The dominant multipole contribution cannot be determined solely upon magnitude, since directional dependence of the ‘S’ factor and ‘L<sup>th</sup>’ order dependence of the pairwise molecular separation (Eq 2.9) must be taken into account. From AAAIP optimized geometries, consistent with DFT and HF dimer structure geometries, the relative orientation and position of each molecule in a single ACA dimer conformer were determined. From these coordinates and the molecular multipole moments, the electrostatic energy of the monomer unit of a dimer was computed directly.

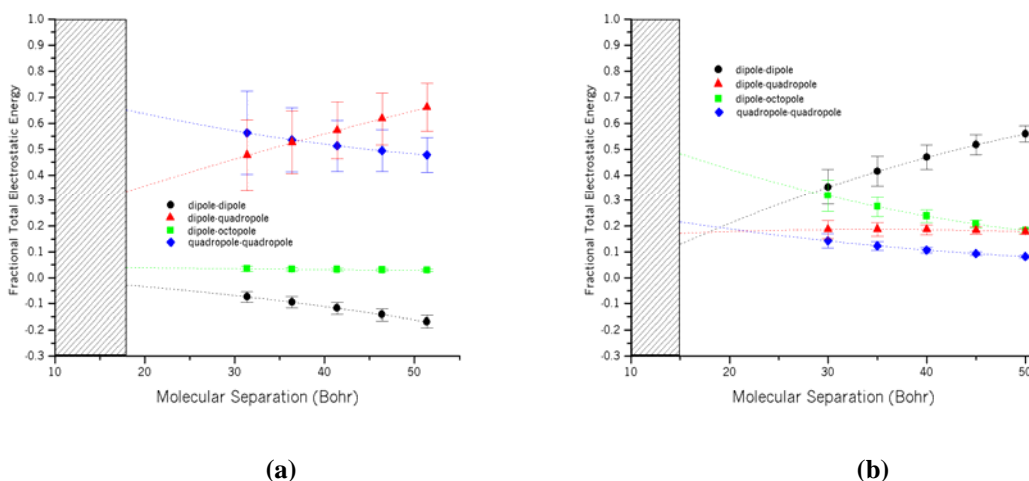


**Figure 2.7.** The molecular moment electrostatic energy distribution for ACA HB motifs is computed from the multipolar electrostatic energy  $\ell_{j\nu}^m S_{j\nu,k\nu}^m \ell_{k\nu}^m / R^{j+k+1}$  for pairwise molecular moments. The monomer building block is used and the fractional total electrostatic energy contribution for pairwise moments  $L^m=4$  is shown for the (a) T-T dimer and (b) H-T dimer conformer. A negative fractional total electrostatic energy signifies a repulsive electrostatic contribution. The cross-hatched area represents the molecular separation of increasing molecular orbital repulsion beyond optimized geometries.

MMMA prescribes qualitatively which pairwise molecular moment interactions influence dimer formation and is shown to be intermolecular distance dependent. Figure 2.7 summarizes the MMMA calculation for the monomer unit in a T-T (a) and H-T (b) arrangement. At large separation, the dominant H-T dimer multipole-multipole interaction is dipole-dipole while for the T-T dimer both dipole-quadrupole and quadrupole-quadrupole predominate (Figure 2.7). Since the twist of the two ACA aromatic planes is nearly the same for both dimer conformers, orientation of the basal planes does not provide insight of whether it is dipole-dipole or quadrupole-quadrupole interactions that dictate dimerization. However there is a direct correlation with the

leading moment orders of the dimer conformers. For the H-T dimer, leading order of non-zero moment is  $|Q_1| > 0$  while for the T-T dimer, leading non-zero moment is  $|Q_2| > 0$ . Perhaps more striking is that contrary to the H-T dimer whose multipolar electrostatic interactions are all attractive, only the T-T dimer has repulsive electrostatic interactions. This is because although the polar carboxylic acids are anti-parallel to each other, there is a residual repulsive dipolar interaction, i.e., two moments are parallel to each but displaced in the transverse direction in a new coordinate frame (Figure 2.8). As the intermolecular distance shortens, the displacement decreases and the repulsive interaction goes to zero (Figure 2.7). In the case of the H-T dimer, the dipolar interaction is always attractive and the carboxylic acids are never parallel nor anti-parallel to each other.

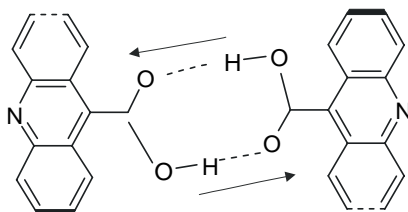


**Figure 2.8.** Displaced anti-parallel dipoles create a repulsive dipolar interaction.

For the H-T dimer, all pairwise multipole interactions *except* dipole-octopole each contribute just  $\approx .17$  of the total electrostatic energy at optimum distance. The dipole-octopole preference can be explained in terms of the probability density factors for p- and

f-electrons of a hydrogen-like atom[35] (Figure 2.9). For the  $\ell = 3, m_l = \pm 2$  modes, the lobes are tilted  $52^\circ$  while the  $\ell = 1, m_l = \pm 1, 0$  the lobes are tilted either  $90^\circ$  or  $0^\circ$ , respectively. Thus for maximum lobe-lobe alignment, the relative tilt between the two hydrogen-like atoms would be either  $52^\circ$  or  $38^\circ$ . Since the ACA monomer can be treated as a united atom with one-center multipole moments, the orientation of the united atoms in the ACA H-T configuration as well as the dominant magnitude of the multipoles supports the MMMA trend (Figure 2.7). From the *ab initio* calculations of the ACA H-T dihedral angle, the HF H-T dihedral angles are  $\approx 69^\circ$  and when looking at the planes edge-on are  $\approx 65^\circ$ . The DFT dihedral angles are  $\approx 59^\circ$ , producing an error of  $\sim 17\%$  that corresponds to a proportionate error in estimating the probability density factor (Table 2.1, Figure 2.4). Clearly,  $\ell = 3, m_l = \pm 3$  lobes tilted at  $90^\circ$  are far from the dihedral angle calculations and consistent with relatively low values for  $|Q_{3,3s}|$ . For the T-T conformer however, competition between pairwise multipole interactions is quite different.

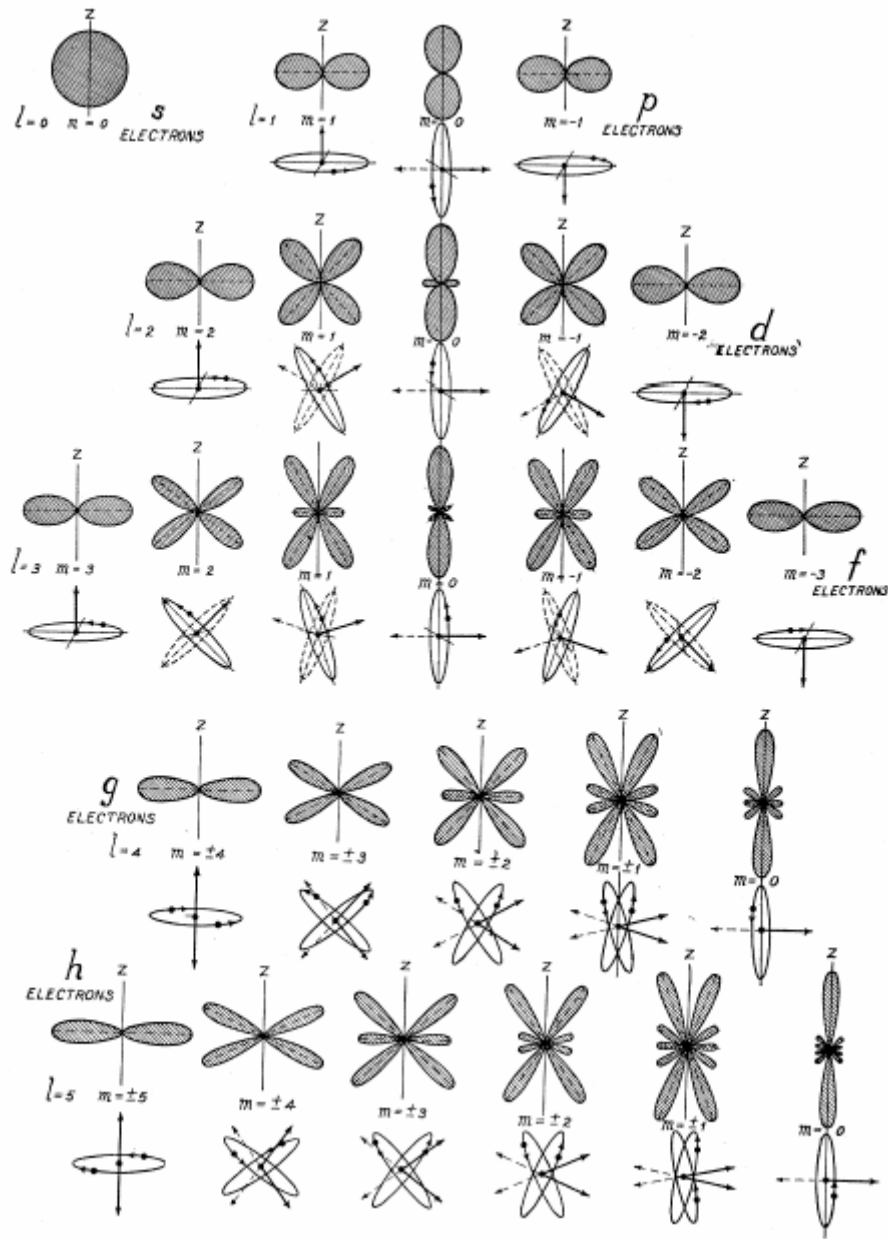


**Figure 2.9.** The probability density factor  $(\Theta_{m,l})^2$  plotted in angular coordinates for single electron hydrogen-like atoms. [From H. E. White, *Physical Review* **37**, 1416 (1931). Reproduced with permission.]

At optimum distance, only the dipole-quadrupole and quadrupole-quadrupole pairwise multipole interactions contribute to the total electrostatic energy for the ACA T-T

conformer, in which the latter accounts for  $\approx .70$  of the total electrostatic energy. In terms of the probability density factors for d-electrons of a hydrogen-like atom, the preferential direction of the two united atoms that comprise the ACA T-T conformer are derived in a similar fashion. For the  $\ell = 2, m_l = \pm 1$  modes, the lobes are tilted  $55^\circ$  while the  $\ell = 2, m_l = \pm 2, 0$  modes are tilted either  $0^\circ$  or  $90^\circ$ , respectively. Thus for maximum lobe-lobe alignment for a quadrupole-quadrupole multipole interaction, the relative tilt between the two hydrogen-like atoms would be either  $55^\circ, 35^\circ, 0^\circ$  or  $90^\circ$ . From the *ab initio* calculations of the ACA T-T dihedral angle (Table 2.1), the HF dihedral angles are  $\approx 69^\circ$  and when looking at the planes edge-on are  $\approx 66^\circ$  (Figure 2.4). The DFT dihedral angles are  $\approx 86^\circ$ , producing an error of  $\approx 20\%$  that corresponds to a proportionate error in estimating the probability density factor although in this case there can be other modes besides quadrupole-quadrupole that satisfy this criteria. It is perhaps likely that mixed components occur at  $\ell = 2$  since all  $|Q_{2,\kappa}|$  values are comparable.

When the point charge is replaced by another ACA monomer whose global axis system is rotated by a new set of Euler angles  $(\alpha, \beta, \gamma)$ , the orientational dependence ‘S’ appears to be more sensitive to orbital alignment as well as to distance separation between local molecular axes. This pronounced ‘S’ dependence of multipolar electrostatic energy contributions due to moment-moment interactions can be observed in a test case of the H-T dimer at the optimum distance of  $\approx 15$  Bohr ( $7.9 \text{ \AA}$ ). When one of the monomers undergoes a  $180^\circ \gamma$  rotation, the entire multipolar electrostatic energy switches from attractive to repulsive, retaining only  $\approx 40\%$  of its original strength. Empty/non-

uniform modes for a particular order may also enhance the discrepancy between MMMA and AAAIP.

Empty modes in the T-T dimer occur for the dipole interactions, i.e.,  $|Q_1| \approx 0$ , and for some quadrupole interactions since  $|Q_{2\kappa}| \approx 0$  except at  $\kappa = 1c$ . Non-uniform modes in the T-T dimer occur are pronounced at the third moment order since  $|Q_{3,2s}| \gg |Q_{3,\kappa}|$  for octopole interactions. For the H-T dimer, quadrupole moment modes are nearly uniform since all  $|Q_{2\kappa}|$  terms are nearly equal in order, and more importantly, have  $|Q_1| \neq 0$ .

An error analysis of MMMA shows excellent agreement with DMA for ACA monomers at a distances of 15 Å or higher. Errors arising between MMMA and DMA dimer energies of the HB motifs was fair. The discrepancies were due to: sensitivity of 'S', silent or asymmetry of the orbital modes, and distance separation between dimer partners (see APPENDIX C: MMMA Error Analysis). Nevertheless, percentage ratings of which modes dominated were well within the margin of error for a moderate range of distance separations (Figure 2.7).

### 2.3.2.2. Dimer Building Block Approach

Analogous to the monomer unit which freely associates through hydrogen bonding, the dimer unit associates with other dimer units. Since dimers are known to form naturally at

a lower temperature compared to monomers, particularly for gas phase hydrogen bonded molecules, a fraction of them associate to form larger clusters. In fact, molecular multipolar electrostatic interaction modes of dimer-dimer clusters compete differently. The total dimer electronic density from B3LYP/6-31G(d) calculations were used to compute the multipole moments of the system (Table 2.3b), in turn, to consider the electrostatic interaction energies of dimer units forming dimer-dimer short chain structures,  $n=4$ . The total dimer electronic density resulting from HF *ab initio* calculations were performed as well (Table 2.3d). Features of these short chains using dimer units are significantly different than those formed using monomer units as shown in Figure 2.10.



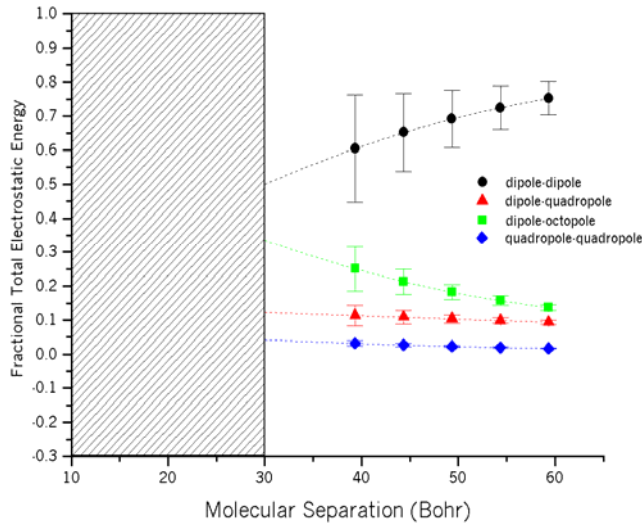


**Figure 2.10.** The molecular moment electrostatic energy distribution for the ACA dimer-dimer short chain is computed from the multipolar electrostatic energy  $\ell_{j\nu}^m S_{j\nu,k\nu}^m \ell_{k\nu}^m / R^{j+k+1}$  for pairwise molecular moments. The dimer building block is used and the fractional total electrostatic energy contribution for pairwise moments  $L_t^m=4$  is shown for the short H-T type chain. The cross-hatched area represents the dimer-dimer separation of increasing ‘molecular’ repulsion beyond optimized geometries.

The short chain analysis using dimer units is similar to the analysis using monomer units. MMMA prescribes which pairwise *dimer* moment interactions influence dimer-dimer formation and shown to be dimer-dimer distance dependent (Figure 2.10). In this context, the short type chain has fixed multipole moments since the dimer acts as a single molecule. Physically, this means that dimers do not dissociate relative to larger chain clusters and remain so in the case of isolated dimers. As the monomer unit analysis, the errors increase proportionally to the fractional amount which a particular moment-

moment interaction contributes to the total electrostatic energy and the assumption is made that the error per mode changes over distance only through propagation of error.

At dimer-dimer separations up to 60 Bohr ( $31.7 \text{ \AA}$ ), the dominant multipole-multipole interaction for short H-T type chains is dipole-dipole (Figure 2.10). Apparently, the short chain formation is influenced by dipole-octopole interactions, and to a greater extent by dipole-dipole interactions of which the latter is not predicted from the simpler H-T HB motif formed from monomer units. Although the shapes of the molecular moment electrostatic energy distribution are similar to the monomer unit for a single H-T dimer (Figure 2.7, 2.10), it is the crossover that occurs in the short separation region that does not have an opportunity to occur before reaching the optimum distance of  $15.8 \text{ \AA}$ . At the ‘molecular’ repulsion onset, the dipole-dipole mode remains dominant although the error is substantial, decreasing to  $\approx .13$  of the total electrostatic energy at 59 Bohr ( $31.2 \text{ \AA}$ ). Dipole-dipole dominance further suggests that there is a residual dipolar-dipolar interaction in which the ‘dimer dipoles’ of the short chain are never parallel nor anti-parallel to each other in their dimer coordinate frame.

In the case of short T-T type chains, the total multipole-multipole electrostatic interactions were repulsive for dimer-dimer separations up to 61 Bohr ( $32.3 \text{ \AA}$ ). For the case of the monomer unit for the T-T dimer, the leading non-zero moment of a single dimer is  $|Q_2| > 0$  and the residual repulsive dipolar interaction results due to the

displaced coordinate frames. This meant that the quadrupole-quadrupole interaction was the lowest order multipole-multipole interaction with 'dimer dipoles' parallel to each other, displaced in the transverse direction (Figure 2.8). Repulsive dipole-dipole interactions for the T-T type chain can plausibly be based on similar reasoning, although no quantitative multipole moment data was collected for short T-T chains of length  $n=4$ . Since the total electrostatic energy was of the wrong sign, this suggests that the dominant mode for the dimer-dimer was probably dipole-dipole despite the large errors due to missing modes and sensitivity to multiple Euler angle shifts.

During optimization, some of the ACA molecules regrouped as dimer pairs while others' did not, sometimes changing their partners or single status during the process. Regardless whether the short chains formed via two dimers (dimer unit) or four individual monomers (monomer unit), the angle between monomers stays relatively the same, i.e.,  $\approx 69^\circ$ . This is analogous to a helical coil in which new ACA monomers attach to the end chain at an angle of  $69^\circ$ . When the new monomer or dimer associates and forms a different rotation angle, the chain structure obtains a curvature point along the chain growth direction. Curvature points occur occasionally, notably at the chain edge and for higher monomer numbers,  $n$ .

The MMMA method using dimer units is fair at very large separations in the case of the H-T dimer. Nevertheless, qualitative percentage ratings of which modes dominated were well within the margin of error for some modes (see APPENDIX C: MMMA Error Analysis).

### 2.3.3. Chain Analysis

Configurations and energies of H-T and T-T type chains of n-monomers of ACA were obtained using the electrostatic and repulsive energy terms from the AAAP method for chain lengths n=2 through n=14. Both AAAP and MMMA methods using ORIENT4.5 program were chosen to evaluate distribution of intermolecular energies among the different moments and directly compare features but only in the short length chain regime. Through use of the atom-atom multipolar electrostatic interactions and repulsive interactions, chain length dependent features were observed for both H-T and T-T type chains.

AAAP provides intermolecular electrostatic energies by explicitly summing over  $(\ell_i, \ell_j)$  pairwise atomic multipole moments (Eq 2.2) over the operators. During the energy minimum search, often the chains would fragment and then re-associate. In the case of H-T chains, the chains retained the typical HB length as well as the twist. In the case of T-T chains, the chains did not always retain the HB interaction between paired monomers that initially formed T-T dimers, but often formed secondary HBs. Even so, it retained its helicity, i.e., dihedral angle, also known as dimer twist angle. Furthermore, the chains did not maintain a straight pattern as in the initial configuration, but instead developed a snake like pattern. Often the ends are turned inward, as expected because the free ends want to close on themselves (Figure 2.11).

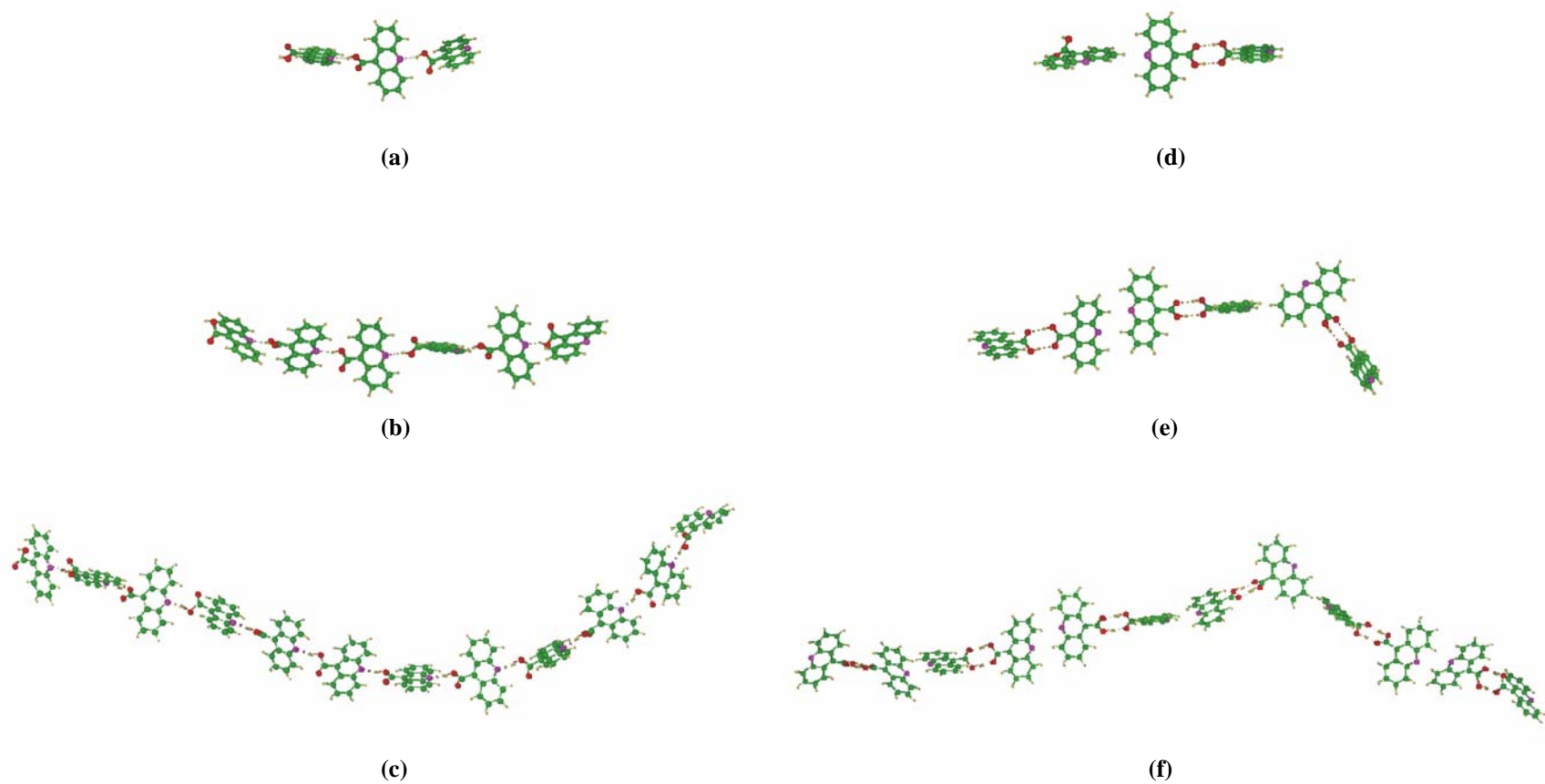


**Figure 2.11.** Optimized geometries of 3-, 6- and 12-monomer length ACA chains of (a)-(c) H-T type and (d)-(e) T-T type. Chains display helical twist about the ‘S’ shaped curve that connects their geometric centers.

Since the sites of the atomic multipole moments are the atom positions themselves in this study, the distance  $R$  between monomer centers for the optimized structure ranged from 6.8 to 9.4 Å. This variation signified that although ACA monomers deviated from their dimer conformation, they maintained a 1-D structure-like form. In the case of dimer-dimer conformers build from dimer units, the distance  $R$  between them extends further to 15.1 Å. The result was similar for consecutive molecular pairs throughout the short chain even in the case of the T-T type chain.

For the local analysis of chains, the dihedral angles can be easily understood if the direction for which the vector rotates to form a dihedral angle is considered to be in the direction of the chain growth. In the conventional sense, the dihedral angles are found for consecutive monomers and the sequence of dihedral angles moves along the ACA molecular chain. In the values reported, the dihedral angle is the absolute acute angle about the axis perpendicular to its basal plane center falling between 0 and 90° the angles found were not random but one of four distinct rotation angles (Table 2.4a, 2.5a), averaged to find a characteristic angle per chain length (Table 2.4b, 2.5b), showing periodicity of  $\approx 9$  monomers for both chain types (Figure 2.12).

**Table 2.4a.** Geometries for ACA H-T chains from n=2 to n=14 were computed, where n is the number of monomers.

n-Length Chain	E (kJ/mol)	Average HB Length r(N··H) (Å)	Average HB Angle a(N··HO) (deg.)	Dihedral Angles (deg.)
2	-40.59106071	2.00324	158.236	68.438
3	-81.29371963	2.00342	158.197	74.561
4	-122.02051518	2.00356	158.189	71.436
5	-162.89651223	2.00421	158.037	73.318
6	-203.74072680	2.00426	158.023	78.147
7	-244.42789029	2.00424	158.031	76.462
8	-285.27517748	2.00427	158.022	76.975
9	-325.90024204	2.00396	158.084	77.187
10	-366.74656743	2.00402	158.070	77.613
11	-407.43358534	2.00402	158.072	72.362
12	-448.28572163	2.00406	158.061	73.306
13	-488.97281938	2.00406	158.063	75.900
14	-529.82113723	2.00410	158.055	79.903

**Table 2.4b.** Dihedral angles for H-T chains in order of increasing rotational twist along the chain growth direction.

	<b>Rotational Twist Angle Order</b>			
	<b>1</b>	<b>2</b>	<b>3</b>	<b>4</b>
<b>Dihedral Angle (deg.)</b>	102.2	-81.6	99.1	-68.4

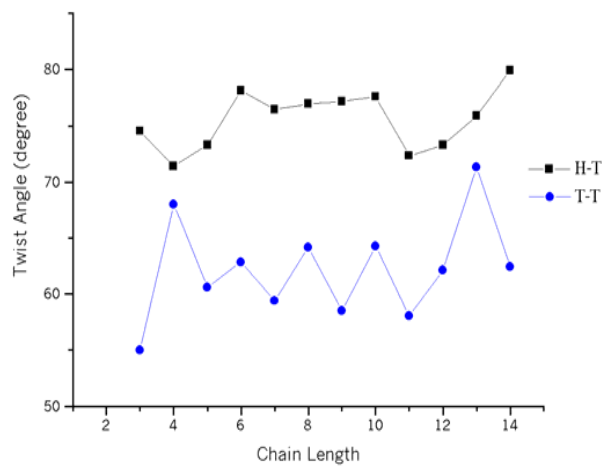


**Table 2.5a.** Geometries for ACA T-T chains from n=2 to n=14 were computed, where n is the number of monomers. Hydrogen bonding occurs along odd molecular pair indices of the dihedral angle plots.

n-Length Chain	E (kJ/mol)	Average HB Length r(O··HO) (Å)	Average HB Angle a(O··HO) (deg.)	Dihedral Angles (deg.)
2	-57.15941798	1.85854	177.277	82.689
3	-66.06799164	1.85855	177.282	54.982
4	-125.03936105	1.85853	177.270	68.039
5	-135.77315729	1.85852	177.267	60.589
6	-191.06220834	1.85853	177.275	62.844
7	-202.00883118	1.85853	177.273	59.379
8	-260.95782061	1.85852	177.268	64.157
9	-267.98460568	1.85854	177.272	58.468
10	-325.09545830	1.85854	177.273	64.246
11	-333.98975831	1.85854	177.279	58.033
12	-394.87224577	1.85853	177.270	62.109
13	-401.79747098	1.85854	177.278	71.349
14	-457.25066654	1.85854	177.274	62.405

**Table 2.5b.** Dihedral angles for T-T chains in order of increasing rotational twist along the chain growth direction.

	Rotational Twist Angle Order		
	1	2	3
<b>Dihedral Angle (deg.)</b>	82.7	-96.6	84.8



(a)

Chain Length Type	Average HB Length $r(\text{N}\cdots\text{H})$ or $r(\text{O}\cdots\text{HO})$ (Å)	Average HB Angle $\alpha(\text{N}\cdots\text{HO})$ or $\alpha(\text{O}\cdots\text{HO})$ (deg)
H-T	2.00	158
T-T	1.86	177

(b)

**Figure 2.12.** Average (a) twist angle and (b) HB geometries for pairwise ACA molecules along the chain growth direction. The twist angle is the averaged dihedral angle.

The ORIENT4.5 optimized n-monomer length geometries resulting from the stamp-like initialization produced structures that resemble 2-D ACA features[30], i.e., similar dihedral angles. The ACA chain ends turning inward would be expected to occur in the gas phase to reduce the amount of free energy of the system. The curling at the ends would not be expected to occur in 1-D adsorbed structures[31] because the chemisorbed ACA molecules will be confined to the Ag (111) support..

From the multipolar electrostatic and repulsive energy interactions calculated for a n-monomer length chains, dependent features for lengths ranging from n=2 through n=14 were obtained (Figure 2.13). In the case of  $E_n$ , the cross over between H-T and T-T chains occurs at n=3. Dynamically however, the energy features for n-monomer length chains are more complex and result in two different energy terms,  $\Delta E_r(n)$  and  $\Delta E_s(n)$ . Since  $\Delta E_r(n)$  is the energy due to the association of an additional dimer to an already existing chain, competition between chain types can occur just as well as with competition with  $\Delta E_s(n)$  formed chains, the latter due to insertion of a monomer anywhere within the existing chain. From the calculated values,  $\Delta E_s(n)$  has one critical chain length at n=4 at which crossover between the chain types occurs, while  $\Delta E_r(n)$  has energy splittings for an even and odd number of monomers in the T-T type chain.

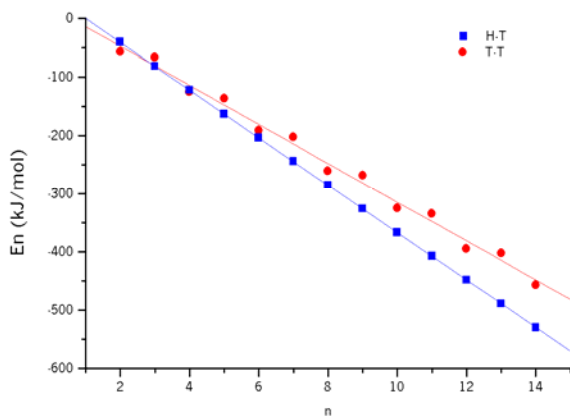
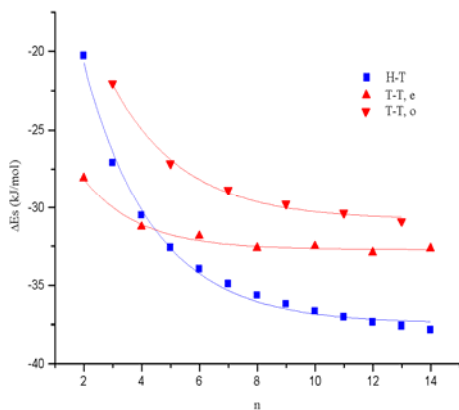
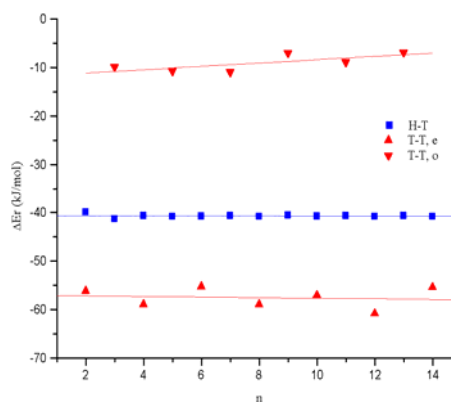


**Figure 2.13a.** Intermolecular energy  $E_n$  for ACA chain lengths of  $n$  monomers were calculated for  $n=2$  through  $n=14$ .



**(a)**



**(b)**

**Figure 2.13b.** Intermolecular energy for ACA chain lengths of  $n$  monomers were calculated for both **(a)**  $\Delta E_s$  and **(b)**  $\Delta E_r$ . For the T-T configuration,  $\Delta E_r$  splits into  $\Delta E_{r,e}$  and  $\Delta E_{r,o}$  where the former corresponds to an even number of monomers and for the latter to an odd number, shown as T-T,e and T-T,o respectively. The trends are for chain lengths  $n=2$  through  $n=14$ .

The two  $\Delta E_r(n)$  branches straddle the H-T type chain for all chain lengths. The striking dissimilarity found between the two energies was that  $\Delta E_r(n)$  prefers dimer-dimer pairs

in T-T type chains for all calculated even-numbered chain lengths and no preference for very long chains, while  $\Delta E_s(n)$  prefers T-T types but for only short chains. Hence, chains will grow more favorably in the T-T type so long as they can associate onto the end of an existing chain. However, when chains grow by associating and dissociating *anywhere* on the chain, then T-T type chains will be limited in size and will be accommodated by H-T type long chains. In the case of  $E_n$  depicting a thermodynamically, stable chain system, ACA H-T long chains are preferred.

From the direct-space measurements of ACA on low index surfaces via STM topography images, there are predominately long H-T type chains up to one monolayer coverage. This is consistent with  $E_n$ 's dominant chain mode prediction for a thermodynamically, stable ACA chain system. However, for the vicinal surfaces and slightly higher coverages, the observed topographies are more complex. The dynamical analysis of ACA H-T and T-T type chain preference depend upon the growth mode.

Molecules in the gas phase have less encounters approaching the chain ends than they do approaching the chain elsewhere, suggesting that the rate of association at the chains ends is less than rate of association via chain insertion. The rate is even less for adsorbed molecules since less encounters exist for approaching the chains ends in 2-D while overcoming energy barriers along the potential landscape.

Experimentally, there is a moderate distribution of long H-T (and less so of long T-T type chains), as well as short T-T type chains in a 2-D planar array. This suggests that the

chains are forming via insertion of monomers within the existing chain. In this study of ACA chain formation, cooperative hydrogen bonding occurs in the H-T type chain while conjugation of a HB with a  $\pi$ -electron system occurs predominately in the T-T type chain. This well-known phenomenological generality stated by Vinogradov, *et al.*[34] is correct for the ACA H-T type chain for lengths greater than four and for ACA T-T type chains of lengths two or four, consistent with both current direct-space measurements and MMMA analysis. Further details of the STM experimental results can be found in Chapter 5.

## 2.4. CONCLUSION

Choosing AAAIP for long chain studies and HF and DFT for monomer and dimer calculations was a cost effective way to study chain formation of moderate size N-heteroaromatics. HF and DFT with moderate basis sets was used to provide reasonable geometries, and electronic properties of ACA, as well as to furnish coefficients of the orbitals forming the wavefunction required by ORIENT4.5 as shown in Tables 2.1-2.3. With the aide of GDMA software used to abstract an atomic multipole moment database from the wavefunction, AAAIP can be implemented to test the stability of arrays and chain-like structures by optimizing the geometric parameters to find the minimum free

energy. Since multipolar electrostatics is the largest contributor to long-range energy, this energy calculation up to 4<sup>th</sup> order multipole moment along with hard-sphere repulsion can give reasonable n-monomer chain configuration geometries and energies.

By first investigating the two different ACA HB motifs in the gas phase by *ab initio* and AAAIP methods, the dimerization energies and geometries were determined. An upper limit of the short-range energy  $\Delta E_{SR}$  of these dimers was found to be  $\sim 25\%$  of the total supermolecule interaction energy. Then in a systematic patterning scheme, the intermolecular energy of H-T and T-T type chains were investigated and T-T chain types preferred. For these type chains at long length, there was no preference as to how long they would grow but only the necessity that they grow in *pairs*. To establish the driving force behind preferred chain structures, the strength of pairwise molecular multipole moments involved in the interactions were examined and an orbital mode picture emerged. For the H-T dimer, the dipole-octopole mode was preferred, while the quadrupole-quadrupole mode was preferred for T-T dimers both at optimum molecular separation. This impetus led to development of the MMMA methodology to partition energy among the different (non-local) modes using a molecule-molecule anisotropic potential. As a consistency check, AAAIP calculations were performed for both AC HB motifs.

From the MMMA methodology, two different molecular building blocks (units) were used. Implementing the ACA monomer unit provided partitioning of the H-T multipole-multipole interaction strengths at  $\sim 10\%$  error for molecular separation distances of

28 Å or higher. For the T-T dimer, the errors increased ~ 15 % for similar separations.

When applying the dimer unit in MMMA, the results were less satisfying. In the case of the ACA dimer-dimer, the errors were ~ 30 %. The values of the T-T dimer-dimer were not reported.

Despite the errors associated with the MMMA method, the identification of which *molecular* multipole-multipole modes dominate is not ambiguous but definitive. It also provides the flexibility to adjust the coarse-graining to a real, physical conditions such as the case of molecular interactions occurring between dimers, predominately. By allowing *dimer* electronic densities to be used as the multipole moment building blocks in MMMA, the geometries of a system of dimers can be obtained. MMMA in conjunction with AAAIP can account for both molecular and atomic details such as equilibrium structures, atom-atom interaction strengths and molecular multipole moment competition.

The AAAIP method provides a good estimate of the electrostatic energy of a system of molecules by considering pairwise atomic multipole moment interactions that take into account the anisotropic intermolecular potential. Even when not coupled with an atom-atom pseudo hard-sphere potential, the electrostatic interaction alone accounts for a majority of the intermolecular interaction energy providing adequate geometries of large molecular systems. By using AAAIP to investigate the length dependent chain type systems, the preference for one type chain over another, as well as the method of association involved in forming that particular chain type system, can be determined.



This is of particular importance for understanding the morphology of molecular chains in supramolecular structures.

## Chapter 3

### Chain Formation, Energy Distributions and Vibrational Frequencies of Isonicotinic Acid

#### ABSTRACT

Anisotropic atom-atom intermolecular potential (AAAIP) calculations were performed for the Head-to-Tail (H-T) and Tail-to-Tail (T-T) type chains of  $n$ -monomers of isonicotinic acid (INA) ranging from  $n=2$  to  $n=14$  using ORIENT, popularly known as Distributed Multipole Analysis (DMA). An alternative single dimer molecular multipole moment analysis (MMMA) dependent upon molecular electrostatic properties was performed as well for the short length chains and compared to AAAIP. Hartree-Fock (HF), Møller-Plesset (MP2) and Density Functional Theory (DFT) calculations performed for the INA H-T and T-T dimer conformer. These computations provided electronic density values for AAAIP and MMMA calculations, qualitatively described the long-range electrostatic effect and assigned the energy partitioning, as well as provided a benchmark for other N-heteroaromatic systems.

From AAAIP and MMMA multipolar electrostatic energy analysis, long and short chain length intermolecular features are obtained and demonstrate the cooperative features of

H-T type chains which crossover from T-T type chains at low monomer number,  $n$ . The correlation between electrostatic moments and electron orbitals suggests an explanation for these definitive features. Vibrational frequencies for the dimer conformers are calculated. Infrared (IR) active vibrational modes associated with inter- and intramolecular vibrations are presented.

### 3.1. INTRODUCTION: LEVEL OF THEORY STRATEGY

Highlights of many important contributions to the study of molecular chains, both experimentally and computationally, has been mentioned previously. The importance of developing computational methods to compliment experimental data however is not exhaustive. Spectroscopic measurements, in addition to real-space imaging of adsorbed molecular adlayers, call for improved levels of theory to characterize the molecular chain models. The *ab initio* computations of the energetics and geometries of hydrogen bonded systems alone have been determined to require, at a minimum, the Møller-Plesset (MP2) theory[88]. Nonetheless, many important global features of a hydrogen bonded system can be described by the AAAIP method.

The AAAIP method uses the electron density obtained from *ab initio* computations of single molecules to obtain the anisotropic electrostatic potential that predominately drives monolayer architecture. By using both *ab initio* chemistry computations and AAAIP, a consistent hybrid-scale method is able to determine intermolecular energies and geometries, hydrogen bonding energies and geometries, and optimized geometrical structures for large molecular assemblies. Based upon the successful treatment of ACA, we now apply this hybrid scale approach to INA. This smaller molecule is amenable to higher levels of *ab-initio* theory, providing more stringent tests of the AAAIP method. This higher level of theory also permits exploration of vibrational frequencies.

It is well known that to achieve a reasonable level of accuracy for hydrogen bonding (HB), the minimal level of theory required is the Moller-Plesset Perturbation to second order (MP2) with split-valence with polarization and diffuse functions on all atom types basis set[88]. This makes the basis set requirements the Dunning-Huzinaga type contracted basis set[89] to provide particularly good results for systems containing a small number of atoms.

In fact, for systems where London dispersion interactions dominate, coupled-cluster computations with perturbative triples [CCSD(T)] have been used to estimate complete basis binding energies within a few tenths of a kilocalorie per mole, although it is a much more expensive calculation than MP2, for dimers such as non-polar benzene[90]. From such calculations, the stable benzene dimer conformer geometries were found to be: edge-face, offset stacked and face-face stacked. The substituent effects of benzene,

particularly in the case of face-face stacked dimer conformers, have proved puzzling[91]. This may be attributed to the extent to which  $\pi$ - $\pi$  stacked interactions dominate over HB, electrostatic and dispersion forces. Even in the case where  $\pi$ - $\pi$  interactions are at a minimum, it is well known that vibrational frequencies of HB complexes require a model chemistry that have an electron correlation and a large basis set[92]. Because INA is of comparable size and aromaticity to benzene, caution must be exercised in interpreting computational results.

The INA *ab initio* calculations provide not only information on INA dimer geometries and energetics, hydrogen bonds and vibrational spectra, but serve as a benchmark for other N-heteroaromatic systems.

## 3.2. THEORY AND METHODOLOGY

### 3.2.1. *Ab Initio* and Intermolecular Theory

Quantum chemistry *ab initio* and AAAIP intermolecular energy models are both used to study INA clusters that form 1-D chains. Because of the many degrees of freedom of such systems, the *ab initio* approach is limited to small aggregates, while the AAAIP

approach is suited for larger assemblies. Both methods provide energetic, geometric and vibrational information, but are based on very different chemistry and physical models. Quantum chemistry models[86] themselves can range in accuracy, and choice is dependent upon both the desired calculation (excited states, ionization potentials, hyperfine spectra, etc.) and available resources[93, 94]. For INA monomer and dimer ground state systems, a moderate size N-heteroaromatic, Hartree-Fock theory with a moderate basis set is sufficient to obtain reliable geometries.

Hartree-Fock *ab initio* calculations are based on the Hartree-Fock model, also known as the "self-consistent field" model. It takes into account the anti-symmetric property of electron coordinates and represents the molecular wavefunction as a sum of Slater determinants, i.e., the N product of 1-particle eigenfunctions. The wavefunction is the solution of the expression,

$$\hat{H}_{\text{HF}} = -\frac{\hbar}{2} \sum_i \frac{1}{m_e} \nabla_i^2 - \frac{Ze^2}{4\pi\epsilon_0} \sum_i \frac{1}{r_i} + \sum_i \sum_j \frac{e^2}{r_{ij}} \quad (3.1)$$

more commonly seen as an the integro-differential expression in which the Hamiltonian commutes with the permutation operator,

$$E[\Phi] = \sum_{\lambda} I_{\lambda} + \frac{1}{2} \sum_{\lambda} \sum_{\mu} [J_{\lambda\mu} - K_{\lambda\mu}] \quad (3.2)$$

where  $I_{\lambda}$ ,  $J_{\lambda,\mu}$ , and  $K_{\lambda,\mu}$  are the average value, direct term and exchange term, respectively, and  $\lambda, \mu$  indices are the single-particle orbital states for which individual electrons belong. With a double zeta plus polarization type basis set (6-31G(d)), this level of theory scales as  $M^4$ , where the number of basis sets for INA is  $M=290$ . The Hartree-Fock method lacks electron correlation beyond the exchange term (built into the Slater determinant) and does not provide accurate values of the hydrogen bond energies. To include reasonable electron correlation, the next level of theory is the Møller-Plesset with second order correction (MP2) using an adequate basis set.

MP2 actually specifies a particular type of electron correlation method. In this electron correlation method, the energy corrections are a solution to a perturbed Hartree-Fock Hamiltonian rather than to a new wavefunction. In the MP2 method, the perturbation in the total Hamiltonian is called the fluctuation potential and is meant to derive local variations in the otherwise average energy for all the electrons of the Hartree-Fock term  $g_{ij}$ , where  $\langle g_{ij} \rangle = J_{ij} - K_{ij}$ . Thus the fluctuation potential is the variance of the Hartree-Fock term  $g_{ij}$ , i.e.,  $H = H_{HF} + H'$  where  $H_{HF}$  is the HF Hamiltonian and  $H' = \sum \sum g_{ij} - \langle g_{ij} \rangle$ . To perform a perturbation expansion with  $g_{ij}$  as the ordering parameter, the HF Hamiltonian is redefined to exclude  $g_{ij}$ . Then correction to second order would indeed include all  $g_{ij}^2$  terms. The second-order Møller-Plesset correction  $E_2$  can be written as,

$$E_2 = \sum_{i,j} \sum_{a,b} [ \langle \phi_i \phi_j | \phi_a \phi_b \rangle - \langle \phi_i \phi_j | \phi_{ba} \rangle ]^2 / [ \epsilon_i + \epsilon_j - \epsilon_a - \epsilon_b ] \quad (3.3)$$

where  $i,j$  corresponds to occupied molecular states and  $a,b$  correspond to unoccupied molecular states. For large basis sets, this computational method scales as  $M^5$  where  $M$  is the number of basis functions and can be quite large is using the Dunning-Huzinaga type correlation consistent contracted basis set.

Although MP2/aug'-cc-pVDZ (or better yet, MP2 with a Complete Basis Set) level of theory is the one of choice for obtaining hydrogen bonding energies and bonding lengths, density functional theory (DFT) calculations are routinely used to obtain these values. The accuracy very much depends upon the density functional chosen, and how well the functional is suited for the chemical system being studied. For moderate size N-heteroaromatics in the gas phase, a suitable and widely used DFT functional is B3LYP often with triple zeta plus polarization and diffusion type basis set (6-311+G(d,p)).

B3LYP is the Becke 3 parameter functional hybrid method used in the field of computational chemistry to specify a particular type of density functional method. The generic density functional method model is a modified Hartree-Fock (HF) energy equation written as a functional of the electron density,

$$E_{\text{total}}[\rho] = E_{\text{kinetic}}[\rho] + E_{\text{n-e}}[\rho] + E_{\text{direct (or coulomb)}}[\rho] + E_{\text{exchange}}[\rho] + E_{\text{correlation}}[\rho] \quad (3.4)$$

The modification of the HF equation occurs through the addition of a correlation term and a redefinition of the exchange term, the latter often done to make the exchange and correlation energy terms appear as similar functionals of  $\rho$ . The functional forms of



$E_{\text{exchange}}[\rho]$  and  $E_{\text{correlation}}[\rho]$  will vary, depending upon which density functional method is used. Some density functionals will replace the two energy terms with a single energy term  $E_{\text{exchange-correlation}}[\rho]$ , since the correlation and exchange terms are permutations of paired electron interactions.

In the B3LYP method,  $E_{\text{exchange-correlation}}[\rho]$  is the linear sum of four specific different density functional exchange and correlation energies: exchange and correlation energy from the local spin density approximation method (LSDA), correlation energy from the generalized gradient approximation (GGA) method, exchange energy from Becke's gradient corrected method and the HF exchange energy.

The LSDA method models the electron density as a slowly varying electron gas density. The GGA, on the other hand, models the electron density as a non-uniform electron gas and modifies the functional dependence of the exchange and correlation energy; the energies are functionals of the electron density and its gradient. Becke's gradient corrected method is a GGA type method that explicitly defines the exchange energy as a function of  $|\nabla \rho| / \rho^{4/3}$ .

B3LYP is often used with triple zeta plus polarization and diffusion type basis set (6-311+G(d,p)). Like the HF level of theory, this computational method scales as  $M^4$ . Even with a reduction of one order of magnitude from MP2 calculations, HF and DFT quantum chemistry computations can be quite expensive for assemblies of N-heteroaromatic molecules, in this case INA.

A common approach to solving the dynamics of large systems is to use force field methods. This method models the molecule and thus the ensemble, in the classical sense, specifically writing the total energy  $E$  of the molecule as a sum of energy terms corresponding to specific degrees of freedom. The energy terms themselves are functions of parameters assigned to particular classes of atoms or molecules and of the molecule's degrees of freedom. Although the method produces qualitatively correct geometries for the molecules of choice, it produces poor conformational energies for organic molecules and in general has difficulty producing accurate relative energies for most molecules. A hybrid-scale method thus offers an economic route for quantitative studies of ensembles of molecules.

To calculate the preferred geometries of large molecular systems, the AAAIP method can be used with far less resources than exclusively *ab initio* methods. The AAAIP method uses the electron density obtained from *ab initio* computations directly of only a single molecule to obtain the overall anisotropy electrostatic potential. By using *ab initio* computations not only to obtain the molecule's atomic multipole moments, but molecular energies, geometries and vibrational data for the monomer and dimer unit, a hybrid scale approach of studying self-driven systems can be realized.

The complexity of defining intermolecular motion and thermodynamically stable states of molecular chains can be reasonably approached by using the AAAIP intermolecular energy model. In this case, the INA chain study is analogous to the ACA chain study. Details of the AAAIP intermolecular energy model description is provided in Chapter 2.

Multipole moments provide information as to how the atom (or molecule's) electronic charge is distributed, providing insight as to the bonding nature of molecules. From the molecular charge distribution, in addition to calculating the electrostatic multipolar electrostatic energy, the optical constants, and subsequently, vibrational spectra can be found as well using AAAIP. Although this will not be investigated in this study, it is mentioned to indicate the potential ability of the AAAIP methodology in quantifying analogous spectroscopic information.

### 3.2.2. Chain Model Configurations and Computational Details

The motivation for quantifying molecular chain length structures for INA with the current strategy is similar to that of ACA. Sampling phase space when dimer configurations and long-range features are established may not be an efficient way to produce n-monomer length chains bound by electrostatic forces. By choosing local characteristics in dimer configurations such as monomer-monomer geometries, as well as long-range features, a specific initial pattern is obtained. Using the same approach to study INA n-monomer length conformer chains as ACA n-monomer length chains, the order of multipole moment terms that contribute strongly to the electrostatic energy as well as the preferred chain length types can be determined.

Initial configurations of the ORIENT4.5 optimization were 1-D arrays of in-plane dimers. Since optimized geometries are sensitive to initial conditions, particularly for the

formation of INA clusters, several initial configurations were sampled for INA dimers. For this trial, HF *ab initio* calculations were performed. From eight in-plane and three out-of-plane dimer geometries, none of the INA molecular pairs formed a more energetically favorable dimer than the H-T or T-T dimer configuration, nor formed a hydrogen bond. The energies were determined from the supermolecule energy, and their energies relative to the hydrogen bonded H-T dimer are shown in Figure 3.1. Thus a narrowly select region of phase space accessible for energetically favorable dimer formation supports a priori that the dimer configurations are the most probable *initial* chain configurations to form stable chains upon optimization. From the dimer configurations, the initial INA chain configurations were comprised of n-INA monomers arranged in a stamp-like fashion, making a linear chain with relative repetitive coordinates chosen to replicate the INA dimer. The geometries were intentionally offset from the corresponding dimer values to avoid being trapped in a local minimum during optimization.

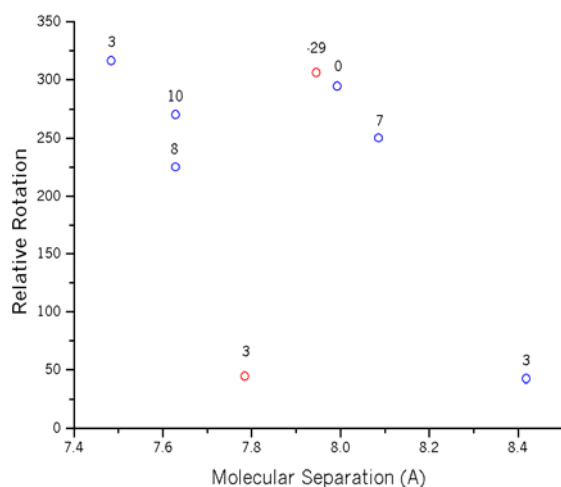


**Figure 3.1** The supermolecule interaction energy differences between random planar orientations about their average is shown. Of the 8 dimer configurations, 6 were above (blue) and 2 (red) were below, indicating that the directional dependence of intermolecular forces skews (uniformly distributed) random selection. All of the dimer configurations are in-plane. Units are kJ/mol above or below the configuration at 0.

For H-T type chains of  $n$ -monomers, there were  $n/2$  replicas of a H-T dimer with each monomer oriented to its nearest neighbor with similar HB features as two INA molecules have within the H-T dimer and lying flat within the plane. Corresponding dimer values are written in parenthesis. Each monomer was rotated in the plane at a  $(\text{N}\cdots\text{H}-\text{O}) \approx 179^\circ$  ( $179.9^\circ$ ) and approximately  $8 \text{ \AA}$  ( $7.6 \text{ \AA}$ ) from its neighbor with a HB length  $r(\text{N}\cdots\text{H}) \approx 2 \text{ \AA}$  ( $1.9 \text{ \AA}$ ). In the case of T-T type chains of  $n$ -monomers, there were  $n/2$  replicas of the T-T dimer each monomer also oriented to its nearest neighbor with similar HB features as two INA molecules have within the parent T-T dimer type, with every monomer lying flat within the plane with its dimer partner. Within the T-T type chain, each monomer was approximately  $9 \text{ \AA}$  ( $9.7 \text{ \AA}$ ) from its neighbor with HB length  $r(\text{O}\cdots\text{H}) \approx 2 \text{ \AA}$  ( $1.8 \text{ \AA}$ ) at the carboxylic acid dimer tails and carbon hydrogens within  $\approx 2 \text{ \AA}$  of

each other. These initial configurations for both H-T and T-T type chains were a repetitive, linear 1-D array, where each monomer was oriented to have slightly offset HB lengths and angles from each other with a similar strategy to the ACA initial configuration scheme.

To compute the electrostatic and repulsive energy terms of INA monomer-monomer interactions to a given order, the atomic pairwise electrostatic and repulsive energies are calculated. The analysis is similar to that performed for ACA intermolecular interactions. During optimization of an n-monomer chain, there were no fixed parameters while stepping-through variation of 6n redundant coordinates to find the lowest intermolecular energy. These 6 coordinates correspond to the center of mass and Euler angles for a rigid molecule.

The computations were produced using Orient4.5 in conjunction with GDMA and Gaussian03. The wavefunction and single point energy of a single INA monomer was obtained at the B3LYP/6-311G(d,p) level of theory using Gaussian03, as well as acquisition of the multipole moments using GDMA. Using the atomic multipole moments obtained from of a single monomer, Orient4.5 was used to optimize the molecular arrangement of the initial configuration, similar to the methodology used in the ACA chain study.

From *ab-initio* calculations however, the INA study was slightly different. Here, the wavefunctions, single point energies, geometries and frequencies of a single INA

monomer and both INA dimer conformers, i.e., Head-Tail (H-T) and Tail-Tail (T-T), were obtained at the HF/6-31G(d) and MP2/6-31+G(d,p) level of theory using Gaussian03 on a high performance processor at Pittsburgh Supercomputer Center. Preliminary H-T and T-T optimized computations and select dimer configuration runs were obtained at the HF/6-31G(d) level of theory using Gaussian98 on a single processor DEC Alpha machine. For these same dimer molecules, *ab-initio* calculations were also performed on a Tiger dual G5 MAX OS in our node cluster but at the B3LYP/6-311G(d,p) level of theory Gaussian03. For a single INA molecule, the same node cluster produced the wavefunction, single point energy and geometries at the B3LYP/6-311G(d,p) level of theory. AAAIP geometries and energies for INA chains using ORIENT4.5 were computed as well on the Tiger machine.

### 3.2.3. Molecular Multipole Moment Analysis Revisted

For quantifying molecular orbitals of INA structures in the mesoscopic regime, the approach is similar to the analysis performed for the ACA chains. The electrostatic energy distribution of pairwise *molecular* multipole moments for molecules and dimer conformers is analogous to the INA atomic moment analysis. Thus the MMMA method is employed.

#### 3.2.3.1. Initial HB Motifs: Initial Monomer

AAAIP software methods are adapted to MMMA for INA clusters in the same fashion as for ACA clusters. They are both comprised of rigid backplane monomers. The decrease in the number of  $\pi$ -electrons per monomer may provide insight into differences in chain formation.

In this study, only the INA H-T and T-T dimers are the clusters of interest in obtaining electrostatic properties. As before, the electrostatic moment ensembles form units (or blocks) from which to build these hydrogen bonding dimer and the monomer unit is the one of choice to build dimer motifs and long chain structures. For the monomer block, the electrostatic moments of a single frozen INA molecule is employed.

The distance 'R' between dimer partners was not arbitrarily selected but rather the measured distance, as in the ACA case, from the monomer molecular backbone center to its partner's monomer backbone center determined from *ab initio* dimer calculations. For the INA H-T HB motif  $R \approx 7.6 \text{ \AA}$ , and for the INA T-T HB motif  $R \approx 9.7 \text{ \AA}$ . From the optimum intermolecular distance 'R' and optimum global axis coordinate system of each molecule, paired order moments of the INA molecule and its dimer partner at the new axis configuration form the corresponding molecular moments. Thus the electrostatic interaction energy due to two (possibly different) static electron density distribution modes can be found and the pairwise summation of all molecular multipole electrostatic interactions is straightforward.



In addition to the wavefunction, geometries, single point energies and frequencies obtained from *ab initio* HF, MP2 and B3LYP model chemistries for the INA monomer and dimer units, the molecular electrostatic moments were computed as well. The electrostatic moments and wavefunction were used to determine the molecular multipole moment tensor for the MMMA analysis and provide wavefunction coefficients for the ORIENT4.5 program. This is analogous to the ACA chain study with the inclusion of MP2 calculations.

#### 3.2.4. Chain Length Dependency

From the AAAIP computation using ORIENT4.5, the chain length dependent energies were computed for H-T and T-T type chains, analogous to the ACA chain study.  $E_n$ ,  $\Delta E_r(n)$  and  $\Delta E_s(n)$  for INA chains of n-monomers was calculated. Details of the chain length dependency description is provided in Chapter 2.

#### 3.2.5. Intra- and Intermolecular Vibrational Modes

The vibrational motion is an important tool to identify the chemical environment and molecular interactions of a molecule or compound. Within a single molecule itself, nuclei undergo vibrational motion that can couple to other vibrational motions. For the case of nearby molecules, such as in the case of hydrogen bonded systems, inter- and new

intramolecular vibrational motion can occur as well. For molecular chains, the vibrational coupling is even more complicated.

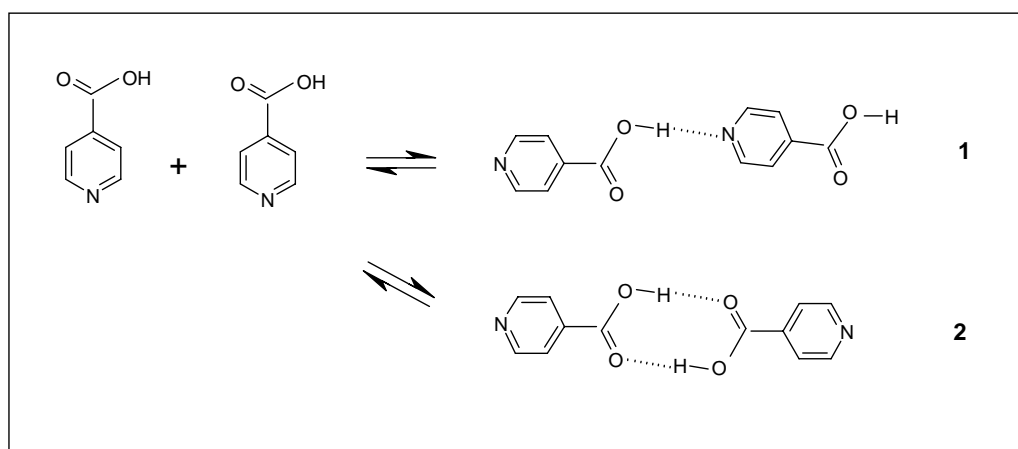
For weakly coupled molecules, observing the vibrational changes of the free molecule has been widely accepted as a method of identifying molecular interactions. In our study of hydrogen bonded INA dimers, we examine the vibrational modes from this perturbative approach, in particular searching for stretching modes that have red-shifted or deformation modes that have blue-shifted, for integrated intensity increases or new modes.

### 3.3. RESULTS

#### 3.3.1. AAAIP Atom-Atom Interactions and *ab initio* Dimer Calculations

From *ab initio* and AAAIP calculations, the INA H-T and INA T-T dimer conformers were confirmed to be stable clusters brought about by self-association confirming previous experimental models (Figure 3.2), consistent with optimum structures resulting from a sampling of phase space. The criteria and methodology for establishing AAAIP interactions and *ab initio* dimers are similar to those performed for ACA, with the

inclusion of MP2 calculations. Included as well are vibrational frequency analysis of the INA monomer at the HF and MP2, and of the dimer conformers at the HF level of theory. Used in conjunction with calibrated vibrational data of a similar N-heteroaromatic molecule, the HF computational scaled results are tailored for this INA study.

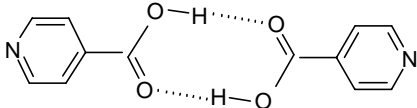
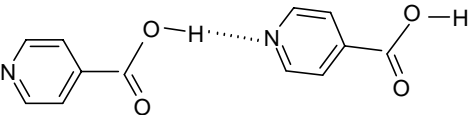


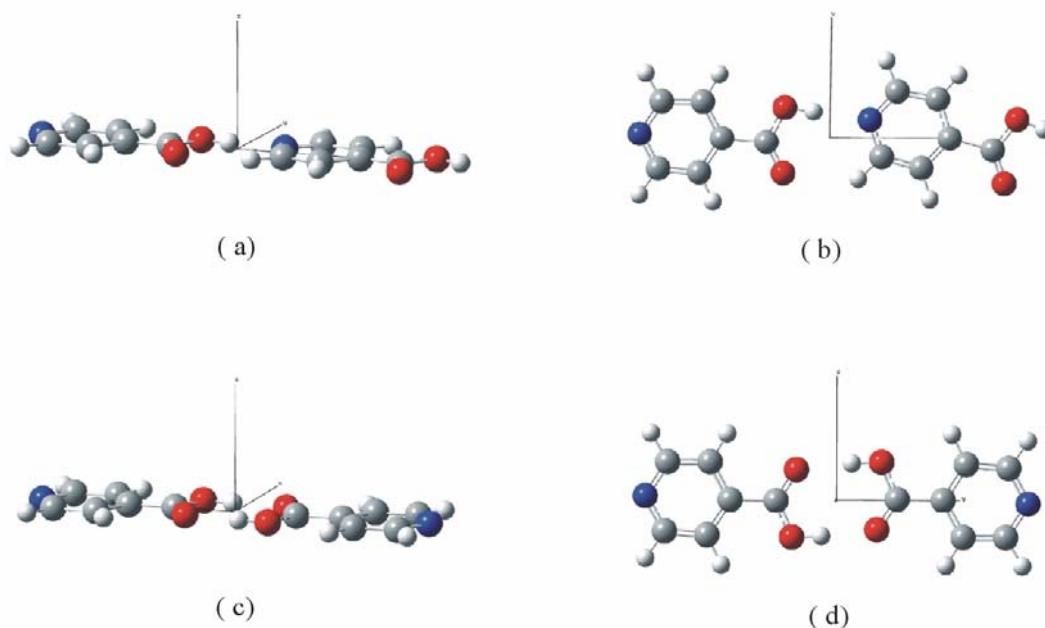
**Figure 3.2.** Formation of gas phase isonicotinic dimer conformer **1** (head-to-tail) and conformer **2** (tail-to-tail) through self-association.

### 3.3.1.1. Dimer Geometries

*Ab initio* calculations for both INA HB dimer motifs were performed, and at three different levels of theory and compared to the AAAIP generated dimers. Both HF, MP2 and DFT *ab initio*, and ORIENT computational methods produced similar INA dimer structures that showed strong HB features and little if no rotational out of the plane for the H-T and T-T conformers (Figure 3.3). The hydrogen bonding geometries for these HB motifs are similar for all four methods (Table 3.1).

**Table 3.1.** Dimer geometries are calculated from HF/6-31G(d), B3LYP/6-311G(d,p) and MP2/6-31+G(d,p) computations. There is no helicity at the HF and DFT level of theory. At the MP2 level of theory, there is a non-significant tilt between the two basal planes. For INA T-T dimers, the H-B length is defined as  $r(\text{O}\cdots\text{H})$ , the HB angle as  $a(\text{O}\cdots\text{HO})$  and dihedral angle both as  $d(\text{C}_3\text{C}_6^\circ\text{C}_3^\circ\text{C}_6)$ , where superscript '°' refers to the second INA molecule and are listed accordingly in absolute values. For INA H-T dimers, the H-B length is defined as  $r(\text{N}\cdots\text{H})$ , the HB angle as  $a(\text{N}\cdots\text{OH})$  and dihedral angle both as  $d(\text{C}_3\text{C}_6^\circ\text{C}_6^\circ\text{C}_3)$ . In the case of T-T dimer conformers, the two H-B lengths and two HB angles are shown. The carbon numbering scheme provided for the dihedral angle is according to NIST Special Publication 922, Polycyclic Aromatic Hydrocarbon Structure Index, L.C. Sander and S.A. Wise.

N-Heteroaromatic Dimer Species	H-B Length (Å)				H-B Angle (deg.)				Dihedral Angle (deg.)			
	HF	DFT	MP2	AAAIP	HF	DFT	MP2	AAAIP	HF	DFT	MP2	AAAIP
	1.82093	1.65965	1.67713	2.44228	175.726	179.056	179.789	174.425	0.005	0.037	14.76	0.013
	1.82093	1.65965	1.67700	2.44228	175.726	179.056	179.825	174.425				
	1.91760	1.74036	1.70641	2.53860	179.904	179.941	179.325	176.564	0.027	0.007	6.714	0.009

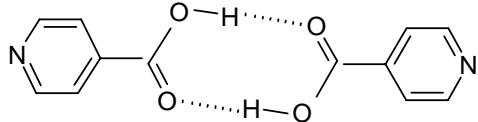
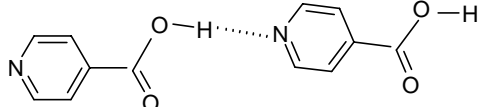


**Figure 3.3.** Optimized geometries of INA (a)-(b) H-T and (c)-(d) T-T dimers display no helical twist about the line that connects their geometric centers.

The HF and AAAIP HB lengths for H-T and T-T conformers are in poor agreement. Since HF bond lengths are characteristically underestimated by as much as a few tenths of an angstrom[86], this would suggest that the atomic charge distribution in the HF calculation is similar to that in the AAAIP multipole moment distribution. However, the HB lengths are grossly exaggerated in the AAAIP method, possibly due to an overestimated hard sphere potential. In the case of the H-T conformer, the HF and ORIENT4.5 dihedral angles differ by  $\approx 5^\circ$  while for T-T conformers they differ by  $\approx 13^\circ$  (Table 3.1).

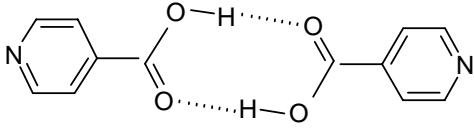
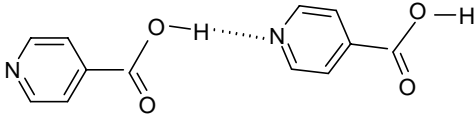
### 3.3.1.2. Short-Range Energy $\Delta E_{\text{SR}}$

The total intermolecular energy calculated from the DFT and AAAIP methods show that the values differ significantly enough to capture the short-range energy between the two INA monomers (Table 3.2a). Although an APT analysis was not performed for the INA dimer conformers, it is expected that there is *less* electron charge at the hydroxyl hydrogens and is redistributed elsewhere within the dimer because like the ACA monomer, there exist a strong dipole moment from the carboxylic acids and subsequent hydrogen donors. Therefore, the total energy  $E_{\text{T}}$  difference between the DFT and the AAAIP calculation is an upper limit on the amount of energy due to short-range effects, attributed predominately to electron correlation and charge density redistribution, the latter brought about by local shifting of charge to other nearby atoms.

N-Heteroaromatic Dimer Species	Intermolecular Energy (kJ/mol)	
	DFT	AAAIP
	-77.5227	-27.4455
	-54.3596	-20.6099

**Table 3.2a.** Total intermolecular energies are calculated from B3LYP/6-31(d) and AAAIP computations. From DFT calculations,  $\Delta E^{AB}$  is the supermolecule interaction energy, i.e.,  $\Delta E^{AB} = E^{AB} - (E^A + E^B)$  based on the total electronic energies of the dimer conformer and monomer with ZPE corrections. From the AAAIP calculations,  $E_T$  is the total intermolecular interaction energy (electrostatic and repulsive energies) of the dimer conformer, i.e.,  $E_T = E_{\text{electrostatic}} + E_{\text{repulsive}}$  up to 4<sup>th</sup> multipole moment. Since  $E_{\text{repulsive}}$  is only a few percent,  $\Delta E_{LR} \cong E_T$ .

By definition of short-range energy  $\Delta E_{SR}$  and calculation of the interaction energies (Table 3.2a), the short range energy values are easily tabulated[95]:  $\Delta E_{SR}|^{T-T} \approx 65\%$ ,  $\Delta E_{SR}|^{H-T} \approx 62\%$  of the total supermolecule interaction energy.  $\Delta E_{SR}$  is grossly overestimated due to a much larger HB length. Although DMA computation of  $E_T$  includes a hard sphere repulsion term, the contribution is negligible and  $E_T \sim E_{LR}$  characterizes the intermolecular Coulomb interactions. For completeness, the total intermolecular energy calculated from the HF, MP2 and AAAIP methods are shown in Table 3.2b.

N-Heteroaromatic Dimer Species	Intermolecular Energy (kJ/mol)		
	HF	MP2	AAAIP
	-59.8220	-72.5006	-27.4455
	-37.4764	-58.2501	-20.6099

**Table 3.2b.** Total intermolecular energies are calculated from HF/6-31(d), MP2/6-31G(d,p) and AAAIP computations. From *ab initio* calculations,  $\Delta E^{AB}$  is the supermolecule interaction energy, i.e.,  $\Delta E^{AB} = E^{AB} - (E^A + E^B)$  based on the total electronic energies of the dimer conformer and monomer with ZPE corrections. From the AAAIP calculations,  $E_T$  is the total intermolecular interaction energy (electrostatic and repulsive energies) of the dimer conformer, i.e.,  $E_T = E_{\text{electrostatic}} + E_{\text{repulsive}}$  up to 4<sup>th</sup> multipole moment. Since  $E_{\text{repulsive}}$  is only a few percent,  $\Delta E_{LR} \cong E_T$ .

### 3.3.2. MMA Molecule-Molecule Interactions and Mesoscopic Features

For INA dimers, atomic pairwise electrostatic interactions and their orbital distribution have been considered using AAAIP. The atomic moments correlate directly with the charge of the atomic orbitals, and the intermolecular energies up to the fourth order of multipole moments, similar to the ACA study.

MMA depends upon the electrostatic properties resulting from *ab initio* computations, found to be sensitive to the level of theory used. Multipolar moments for both HF, MP2 and DFT were computed and are in relatively fair agreement with one another. MP2 and



DFT monomer and all dimer multipolar moments are in good agreement, while the HF moments are overall in fair agreement with either MP2 or DFT.

Comparing HF to DFT multipolar moments, INA H-T dimers are in fair agreement and relatively good agreement for INA monomer multipole moments, the latter up to third order. For INA T-T dimer multipole moments, the agreement is poor. At each level of theory, the monomer (and dimer) was optimized, suggesting that the differences in the multipole moments are due to differences in the calculated electronic density of non-identical geometries. Only the DFT electrostatic moments were used in the MMA analysis.

The total molecular electronic density resulting from B3LYP/6-311G(d,p) calculations were used to compute the monomer multipole moments (Table 3.3a), and the total dimer electronic density from B3LYP/6-31G(d) calculations used to compute the dimer multipole moments (Table 3.3b). Both HF/6-31G(d) and MP2/6-31+G(d,p) level of theory calculations were also used to produce monomer (Table 3.3c, Table 3.3e) and dimer multipole moments (Table 3.3d, Table 3.3f).

**Table 3.3a.** The monomer molecular multipole moments  $\ell_{j,k}^m$  of order  $j$ , component  $k$  were computed at the B3LYP/6-311G(d,p) level of theory. They are the spherical tensor form multipole moments in atomic units (a.u.) listed  $\ell_{1,0}^m$   $\ell_{1,1c}^m$   $\ell_{1,1s}^m$ , etc.

$j$	B3LYP/6-311G(d,p) $\ell_{j,k}^m$ (a.u.)				
1	-0.00003931	-.48169138	-.52049875		
2	-1.2767922	-.000772161	.000386080	-3.5011096	7.1682318
3	-.006950247	17.682243	17.576999	.0067975240	.011963642
	-111.49651	-56.307764			
4	243.32974	.10530227	.0012585934	-530.02999	-187.07900
	-.078808188	-.045508958	-50.981017	500.35657	

**Table 3.3b.** Molecular multipole moments for N-heteroaromatic INA H-T and T-T dimer conformers are computed. The dimer molecular multipole moments  $\ell_{j,k}^m$  of order  $j$ , component  $k$  were computed at the B3LYP/6-311G(d,p) level of theory. They are the spherical tensor form multipole moments in atomic units (a.u.) of order  $j = 1, 2, 3, 4$  and are listed  $\ell_{1,0}^m$   $\ell_{1,1c}^m$   $\ell_{1,1s}^m$ , etc.

$j$	H-T $\ell_{j,k}^m$ (a.u.)					T-T $\ell_{j,k}^m$ (a.u.)				
1	.000078637	-2.0186529	.97132512			-0.000511140	.00000000	.00000000		
2	-2.9867638	-.00154432	.000386080	-3.1518347	-13.146048	3.0686062	.00000000	.00000000	14.803432	-11.478951
3	-.01495356	207.62916	-65.907668	.013866949	.001087603	.064096733	.00000000	.00000000	.16395628	-.011963642
	-461.55891	165.70510				.00000000	.00000000			
4	800.40587	.55063438	-.04258239	-1396.6091	1243.0898	-432.59222	.00000000	.00000000	-14889.833	-11319.395
	-.54333254	.012764709	-416.73865	-2862.1238		.00000000	.00000000	-2830.7868	7812.5922	

**Table 3.3c.** The monomer molecular multipole moments  $\ell_{j,k}^m$  of order  $j$ , component  $k$  were computed at the HF/6-31G(d) level of theory. They are the spherical tensor form multipole moments in atomic units (a.u.) listed  $\ell_{1,0}^m$   $\ell_{1,1c}^m$   $\ell_{1,1s}^m$ , etc.

$j$	HF/6-31G(d,p) $\ell_{j,k}^m$ (a.u.)				
1	-0.00511140	.46509893	-.57637038		
2	-1.3227118	.000128693	-.001286935	-3.8577190	-7.7721904
3	-0.014321723	-16.113836	18.574742	.012507445	-.056555401
	117.94302	-60.097411			
4	248.44167	-.30646736	.10068743	-517.05639	194.30842
	.23253966	-.26417395	-41.103727	-528.64326	

**Table 3.3d.** Molecular multipole moments for N-heteroaromatic INA H-T and T-T dimer conformers are computed. The dimer molecular multipole moments  $\ell_{j,k}^m$  of order  $j$ , component  $k$  were computed at the HF/6-31G(d) level of theory. They are the spherical tensor form multipole moments in atomic units (a.u.) of order  $j = 1, 2, 3, 4$  and are listed  $\ell_{1,0}^m$   $\ell_{1,1c}^m$   $\ell_{1,1s}^m$ , etc.

$j$	H-T $\ell_{j,k}^m$ (a.u.)					T-T $\ell_{j,k}^m$ (a.u.)				
1	.000275229	1.6584951	1.0444183			.00000000	.00000000	.00000000		
2	-3.2420979	.005533823	-.00115824	-3.4772359	14.435686	2.6681950	.00000000	.00000000	19.504215	2.3393917
3	-.03994637	-189.95474	-72.409676	.053564492	.10549758	.003650635	.00000000	.00000000	.008157029	-.072869456
	467.46271	189.34521				.00000000	.00000000			
4	826.81557	-2.1400273	.073627684	-1362.4845	-1418.0690	-399.80009	.00000000	.00000000	-16853.099	634.34001
	2.7227675	-.13708186	-521.62167	3337.5216		.00000000	.00000000	-8877.4868	-1006.0737	

**Table 3.3e.** The monomer molecular multipole moments  $\ell_{j,k}^m$  of order  $j$ , component  $k$  were computed at the MP2/6-31+G(d,p) level of theory. They are the spherical tensor form multipole moments in atomic units (a.u.) listed  $\ell_{1,0}^m$   $\ell_{1,1c}^m$   $\ell_{1,1s}^m$ , etc.

$j$	MP2/6-31+G(d,p) $\ell_{j,k}^m$ (a.u.)				
1	.000235911	-.39169125	-.59996152		
2	-1.4442311	-.002831258	.006305984	-4.8184803	8.2029279
3	-.01586622	13.880868	19.829316	.017401662	-.036978532
	-125.45460	-64.203308			
4	644.76828	.16802215	-.22298071	-29.955453	-204.13893
	-.10378262	.21700003	609.45568	569.01077	

**Table 3.3f.** Molecular multipole moments for N-heteroaromatic INA H-T and T-T dimer conformers are computed. The dimer molecular multipole moments  $\ell_{j,k}^m$  of order  $j$ , component  $k$  were computed at the MP2/6-31+G(d,p) level of theory. They are the spherical tensor form multipole moments in atomic units (a.u.) of order  $j = 1, 2, 3, 4$  and are listed  $\ell_{1,0}^m$   $\ell_{1,1c}^m$   $\ell_{1,1s}^m$ , etc.

$j$	H-T $\ell_{j,k}^m$ (a.u.)					T-T $\ell_{j,k}^m$ (a.u.)				
1	-0.01879426	1.7480233	1.1254538			.018047207	-0.000117955	-0.000078637		
2	-3.0209406	.57989320	1.1761305	-5.7509298	15.934323	2.0800636	.0029599520	-0.005019048	-19.463743	1.7827920
3	-2.4497170	-179.06493	-76.527297	8.6208923	-86.213269	5.1496425	.020893780	.0045570798	-10.213144	-168.55467
	465.49538	197.66945				.0054391518	-0.036298016			
4	824.86309	-251.94365	-142.73449	-1240.1158	-1595.5077	-294.16895	-0.87325371	.68803077	1640.2022	-201.09170
	315.51192	314.02066	-1012.8779	3860.2792		1.3880232	-1.4252073	-9435.6941	561.29704	

### 3.3.2.1. Monomer Building Block Approach

The monomer multipole moments were used to compute the electrostatic energies of monomer units and of thus larger ensembles. From the moment terms listed (Table 3.3a), the quadrupole moment magnitude  $|Q_2|$  is only a factor of 12 larger than the dipole moment magnitude  $|Q_1|$ . The importance of the 'S' factor, the multipolar moments and the order of the multipolar moments itself, cannot be overemphasized in determining the intermolecular geometries and interaction energy of packed structures. From AAAIP optimized geometries, the INA motifs are consistent with DFT, MP2 and HF dimer structures.



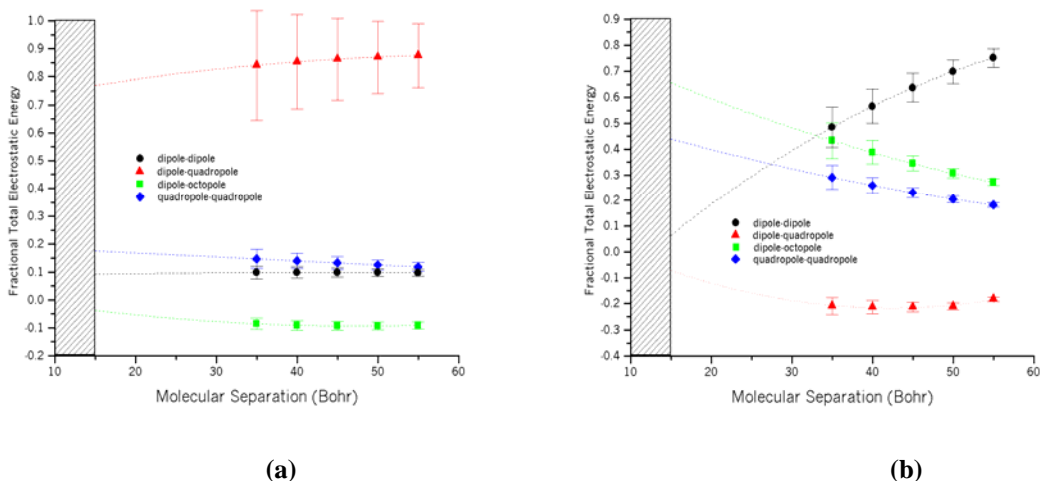


**Figure 3.4.** The INA dimer multipolar electrostatic energy  $\ell_{jv}^m S_{jv,kw}^m \ell_{kw}^m / R^{j+k+1}$  for pairwise molecular moments is computed. The fractional total electrostatic energy contribution for pairwise moments  $L^m=4$  is shown for the (a) T-T dimer conformer and (b) H-T dimer conformer. A negative fractional total electrostatic energy signifies a repulsive electrostatic energy contribution. The cross-hatched area represents the molecular separation of increasing molecular orbital repulsion beyond optimized geometries. Because the flat parallel geometries required more accurate multipole moment values, the MP2 calculations were used in the T-T case.

MMMA prescribes qualitatively which pairwise molecular moment interactions influence dimer formation and is shown to be intermolecular distance dependent. Like the H-T ACA case, the H-T INA paired moments that dominant at long range crossover within the 15-60 Bohr separation range. Consequently, the dipole-dipole interaction no longer dominants at short separation distance. However, unlike the T-T ACA case, the T-T INA paired moments that dominant at long range continue to dominant at short range. These INA pairwise moments do not crossover at some separation distance, and the same modes remain dominant throughout. Figure 3.4 summarizes the MMMA calculation for the monomer unit in a (a) T-T (a) and (b) H-T arrangement. For the H-T dimer, the

dominant multipole-multipole interaction is both dipole-octopole and quadrupole-quadrupole at short range, while for the T-T dimer it is dipole-quadrupole through the 15-60 Bohr separation range (Figure 3.4).

The twist of the two INA aromatic planes is nearly zero, the same for both dimer conformers, and offers no insight as to whether it is dipole or quadrupole interactions that dictate dimerization. However there is a direct correlation with the leading moment orders of the dimer conformers. For the H-T dimer, leading order of non-zero moment was  $|Q_1| > 0$  while for the T-T dimer, leading non-zero moment was  $|Q_2| > 0$ . This, in addition to a repulsive electrostatic interaction mode for the T-T conformer, were the same trends found for ACA dimers. However, unlike ACA, INA has a repulsive electrostatic interaction mode throughout the entire molecular separation for the H-T dimer. This dipole-quadrupole repulsion mode comprises about  $\approx -.05$  of the total electrostatic energy (where repulsive to attractive energy is about a 1: 6 ratio).

Of the remaining H-T dimer modes, the pairwise multipole interactions modes are attractive and each contributes  $\approx .60$  of the total electrostatic energy. These are the highest mode indexes, i.e., dipole-octopole and quadrupole-quadrupole. The dipole-dipole interaction is the lowest mode index, and contributes about 10 % to the H-T molecular electrostatic interaction at optimum molecular separation.

The dipole-octopole preference can be explained in terms of the probability density factors for p- and f-electrons of a hydrogen-like atom[35] (Figure 2.9, Chapter 2),

identical to the dipole-octopole mode analysis found for the ACA H-T dimer. For the  $\ell = 3, m_l = \pm 2$  modes, the lobes are tilted  $52^\circ$  while the  $\ell = 1, m_l = \pm 1, 0$  the lobes are tiled either  $90^\circ$  or  $0^\circ$ , respectively. Thus for maximum lobe-lobe alignment, the relative tilt between the two hydrogen-like atoms would be either  $52^\circ$  or  $38^\circ$ . Clearly,  $\ell = 3, m_l = \pm 3$  lobes tilted at  $90^\circ$  are far from the dihedral angle calculations and consistent with relatively low values for  $|Q_{3,3s}|$ . For the H-T quadrupole-quadrupole mode, the probability density factors are between strictly d-electrons, and the analysis is similar. For the  $\ell = 2, m_l = \pm 1$  modes, the lobes are tilted  $55^\circ$  while the  $\ell = 2, m_l = \pm 2, 0$  modes are tiled either  $0^\circ$  or  $90^\circ$ , respectively. Thus for maximum lobe-lobe alignment for a quadrupole-quadrupole multipole interaction, the relative tilt between the two hydrogen-like atoms would be either  $55^\circ, 35^\circ, 0^\circ$  or  $90^\circ$ . From the *ab initio* calculations of the INA T-T dihedral angle (Table 3.1), the HF dihedral angles are  $\approx 0^\circ$ . For the INA T-T conformer however, there is only one dominant mode, i.e., dipole-quadrupole.

At optimum distance, the dipole-quadrupole multipole interactions contributes  $\approx .75$  of the total electrostatic energy to the total electrostatic energy for the INA T-T conformer. In terms of the probability density factors for d-electrons of a hydrogen-like atom, the preferential direction of the two united atoms that comprise the INA T-T conformer are derived in a similar fashion. For the  $\ell = 2, m_l = \pm 1$  modes, the lobes are tilted  $55^\circ$  while the  $\ell = 1, m_l = \pm 1, 0$  modes are tiled either  $0^\circ$  or  $90^\circ$ , respectively. Thus for maximum lobe-lobe alignment for a dipole-quadrupole multipole interaction, the relative tilt between the two hydrogen-like atoms would be either  $55^\circ, 0^\circ$  or  $90^\circ$ . From the *ab initio*

calculations of the INA T-T dihedral angle (Table 3.1), the HF dihedral angles are  $\approx 0^\circ$ . The flat dimer geometry suggests a relative tilt of zero and that little mixing between modes occur.

When the point charge is replaced by another INA monomer whose global axis system is rotated by a new set of Euler angles  $(\alpha, \beta, \gamma)$ , the orientational dependence ‘S’ appears to be more sensitive to orbital alignment as well as to distance separation between local molecular axes, as was pointed out earlier. The appearance of empty/non-uniform modes of particular orders occur as well for the INA case, enhancing the discrepancy between MMMA and AAAIP.

Empty modes in the T-T dimer occur for the dipole interactions, i.e.,  $|Q_1| \approx 0$ , and for some quadrupole interactions since  $|Q_{2\kappa}| \approx 0$  except at  $\kappa = 1c$ . Non-uniform modes in the T-T dimer occur are pronounced at the third moment order since  $|Q_{3,2s}| \gg |Q_{3,\kappa}|$  for octopole interactions. For the H-T dimer, quadrupole moment modes are nearly uniform since all  $|Q_{2\kappa}|$  terms are nearly equal in order, and more importantly, have  $|Q_1| \neq 0$ .

### 3.3.3. Chain Analysis

Configurations and energies of H-T and T-T type chains of n-monomers of INA were obtained using the electrostatic and repulsive energy terms from the AAAIP method for

chain lengths  $n=2$  through  $n=14$ . Through use of the atom-atom multipolar electrostatic interactions and repulsive interactions, chain length dependent features were observed for both H-T and T-T type chains, similar to the ACA case.

AAIP provides intermolecular electrostatic energies by explicitly summing over  $(\ell_i, \ell_j)$  pairwise atomic multipole moments over the operators. During the energy minimum search, often the chains would fragment little and then re-associate. In the case of H-T chains, the chains retained the typical HB length while keeping their uniformly bent fragment during the optimization, eventually fluctuating about its center of mass, much like a flipped coin on a table top. In the final configuration of each H-T  $n$ -monomer chain, the chain resembled a horseshoe maintaining a constant angle of  $\approx 28^\circ$  between consecutive INA molecules. As the chain lengthened, the gap was reduced until a chain length of 13-monomers fully closed the gap. For chain lengths greater than 13-monomers, as in the 14-monomer chain length, the bent fragments did not continue closing the open horseshoe but instead rotated in the opposite direction at the midway point, forming an 'S' shaped chain as shown in Figure 3.5.

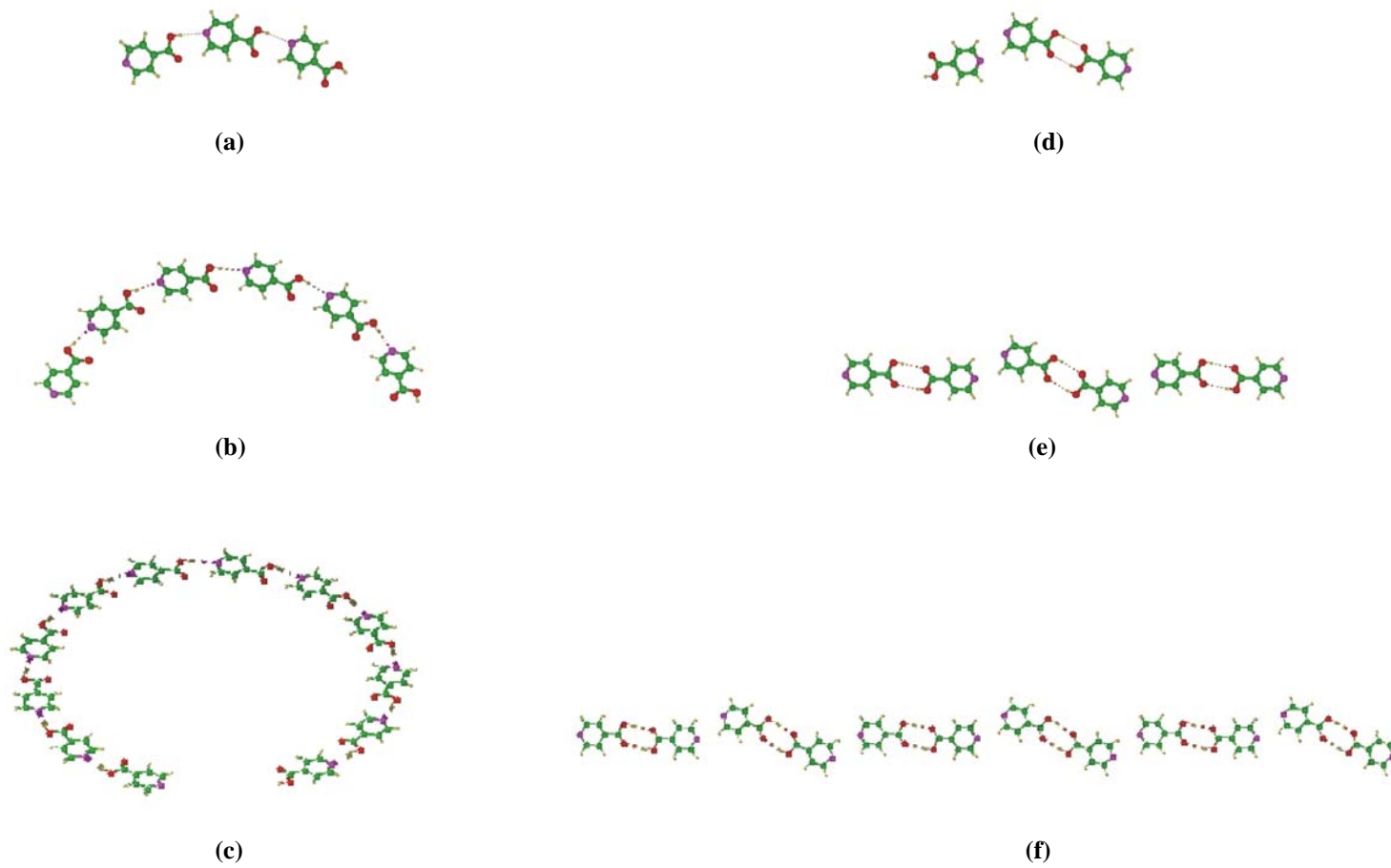


**Figure 3.5.** Optimized geometries of 3-, 6- and 12-monomer length INA chains of (a)-(c) H-T type and (d)-(e) T-T type. Chains display linearity for the H-T chain type and high curvature for the T-T chain types.

In, the case of T-T chains, the chains did not always retain the HB interaction between paired monomers that initially formed T-T dimers, but often formed secondary HBs. Even so, the T-T chains retained its helicity of zero forming near linear molecular chains (Figure 3.5).

The ORIENT4.5 optimized n-monomer length geometries resulting from the stamp-like initialization produced structures that resemble 2-D INA chains[96]. Although the INA H-T type chains described were not observed experimentally, chain ends turning onto themselves would be expected to occur in the gas phase to reduce the amount of free energy of the system. However, since observed INA molecular structures undergo weak adsorption onto a 2-D crystalline support, the anchoring of electron rich atoms of the cluster onto certain substrate sites is expected. Thus curling at the ends would not be expected to occur in 1-D adsorbed structures[31], even for the H-T type chains.

From the multipolar electrostatic and repulsive energy interactions calculated for a n-monomer length chains, dependent features for lengths ranging from n=2 through n=14 were obtained (Figure 3.6). In the case of  $E_n$ , the crossover between H-T and T-T chains occurs at n=3. In the dynamical case, the calculated values shows that  $\Delta E_s(n)$  has one critical chain length at n=4 at which crossover between the chain types occurs, while  $\Delta E_r(n)$  has energy splittings for an even and odd number of monomers in the T-T type chain, very similar to the results of the ACA chain types but with baseline energy shifts of  $\sim +20$  kJ/mol.

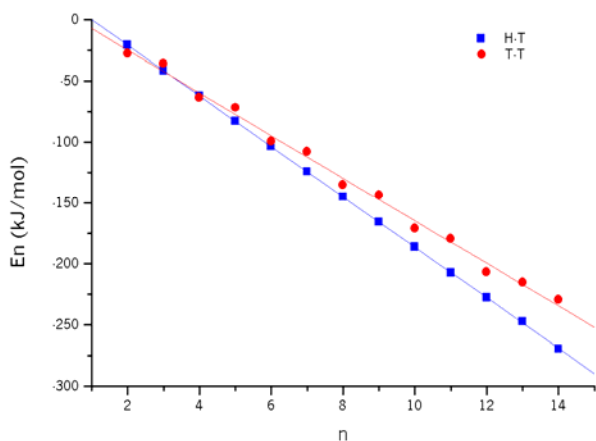
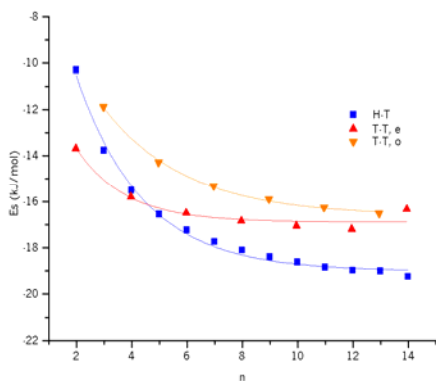
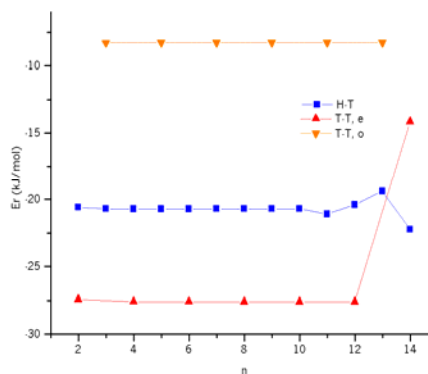


**Figure 3.6a.** Intermolecular energy  $E_n$  for INA chain lengths of  $n$  monomers were calculated for  $n=2$  through  $n=14$ .



(a)



(b)

**Figure 3.6b.** Intermolecular energy for INA chain lengths of  $n$  monomers were calculated for both (a)  $\Delta E_s$  and (b)  $\Delta E_r$ . For the T-T configuration,  $\Delta E_r$  splits into  $\Delta E_{r,e}$  and  $\Delta E_{r,o}$  where the former corresponds to an even number of monomers and for the latter to an odd number, shown as T-T,e and T-T,o respectively. The trends are for chain lengths  $n=2$  through  $n=14$ .

The two  $\Delta E_r(n)$  branches straddle the H-T type chain for all chain lengths. The striking dissimilarity found between the two energies was that  $\Delta E_r(n)$  prefers dimer-dimer pairs



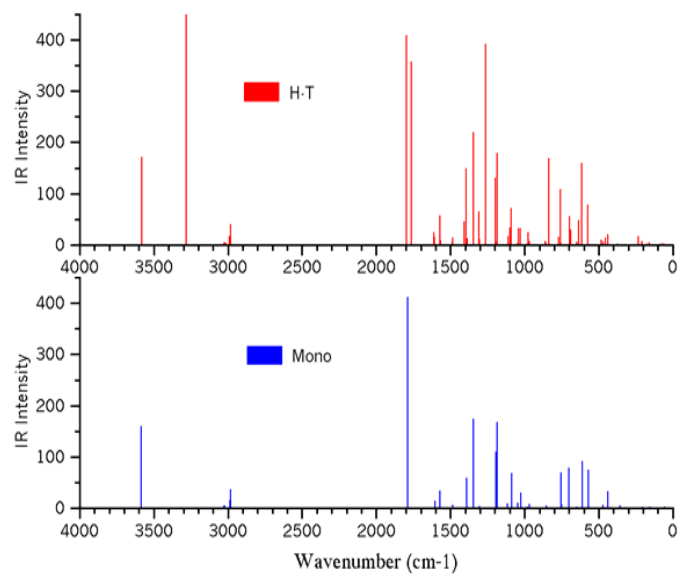
in T-T type chains for all calculated even-numbered chain lengths up to  $n=14$ , then switches to H-T preference, while  $\Delta E_s(n)$  prefers T-T types but for only short chains. For the T-T type chains, the anomaly at  $n=14$  indicates that long chains would no longer continue growing in pairs through attachment, and that any long chain grown is a H-T type chain. However, if chains grow only by associating and dissociating *anywhere* on the chain, then T-T type chains will be limited in size and will be accommodated by H-T type long chains. In the case of  $E_n$ , INA H-T long chains are preferred.

Molecules in the gas phase have less encounters approaching the chain ends than they do approaching the chain elsewhere, suggesting that the rate of association at the chains ends is less than rate of association via chain insertion. The rate is even less for adsorbed molecules since less encounters exist for approaching the chains ends in 2-D while overcoming energy barriers along the potential landscape.

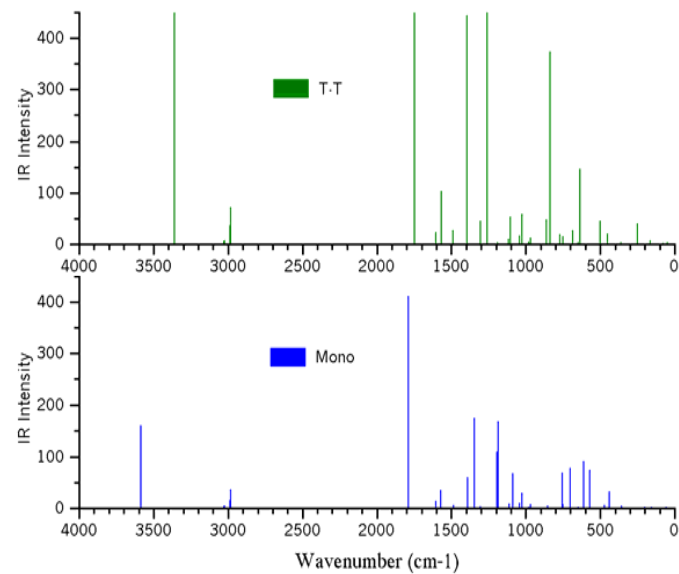
From direct-space measurements of INA monolayers via STM topography images, there is a large distribution of only one type chain in a 2-D planar array since no distinction is made between packed chains; the packed chains appear the same throughout the topographic images. The exception to this is at the rotational domain boundaries where the dimer chain type switches. This is consistent with  $E_n$ 's dominant chain mode prediction for a thermodynamically, stable INA chain system, and with the dynamic chain growth modes. Since the preferred chain type is H-T via either growth method, the chain type at the rotational domain boundary is T-T where only short chains can exist. Further details of the STM experimental results can be found in Chapter 5.

#### 3.3.4. Vibrational Spectra of INA Monomer and Dimers

From *ab initio* calculated at the HF and MP2 level of theory, and the use of calibrated vibrational data of nicotinic acid, a similar N-heteroaromatic molecule, accurate vibrational data was obtained for the INA monomer and dimer conformers. From HF/6-31G(d) optimized nicotinic acid, frequency computations at the same level of theory were obtained and compared to experimental vibrational data of gas phase nicotinic acid available from the NIST database to obtain a best-fit-line and subsequent scaling factor (see APPENDIX D: Calibration of INA Vibrational Spectra). The scaling factor of 0.88 (0.8836) was used for all HF monomer and dimer conformer vibrational data. For vibrational analysis, only the monomer modes were obtained at the MP2 level of theory using a prescribed scaling value of 0.995. The vibrational INA monomer data agrees relatively well (Figure 3.7, Table 3.4).



(a)



(b)

**Figure 3.7.** IR frequencies for INA monomer and dimer conformers computed from HF *ab initio* calculations. The (a) H-T dimer compared to the monomer shows a new mode at  $3266\text{ cm}^{-1}$ , while the (b) T-T dimer compared to the monomer shows a new mode at  $3337\text{ cm}^{-1}$ . The frequencies correspond to the acceptor-donor HB. The spectra was scaled specific for this system.

**Table 3.4.** IR active modes of INA monomers and dimers are listed. From quantum chemistry methods, two different fields of theory are used for gas phase INA: HF/6-31G(d), denoted HF, and MP2/6-31+G(d,p), denoted MP2. Frequencies from specific monomer and dimer conformer HF calculations are indicated, i.e., monomer (M), head-to-tail INA dimer (H) and tail-to-tail INA dimer (T). Frequency  $\nu_0$  is the mid-range value of the HF values for that mode, and only MP2 INA monomer frequencies are calculated. Ref<sup>a</sup> is Li, H. PhD thesis (2006) of adsorbed INA on Ag(111) in vacuum, and Ref<sup>b</sup> is P. Koczoń, *et al.* J of Molecular Structure **655** (2003), 89 of INA pellets in air. Scaling factors were used for the calculations, i.e., 0.88 (HF), 0.995 (MP2).

mode	frequency $\nu_0$	calculated		observed	
		HF	MP2	Ref <sup>a</sup>	Ref <sup>b</sup>
1	49	49 (vw) T			
2	58	57 (vw) M 59 (vw) H			
3	80	79 (vw) T 82 (vw) H	87 (vw)		
4	159	155 (vw) M 160 (vw) H 163 (vw) T	156 (vw)		
5	175	175 (vw) H			
6	202	202 (vw) M	208 (vw)		
7	230	230 (w) H			
8	250	250 (m) T			

9	357	356 (vw) M 359 (vw) T	355 (vw)
10	436	435 (m) M 437 (w) H	426 (w)
11	449	448 (w) T 451 (w) H	
12	470	470 (vw) M 471 (vw) H	469 (vw)
13	481	481 (vw) H	
14	499	499 (m) T	
15	569	568 (m) M 570 (m) H	577 (m)
16	611	609 (m) M 613 (s) H	593 (m)
17	631	631 (m, s) H, T	638 (vw)
18	645	644 (vw) H 645 (vw) T 646 (vw) M, H	
19	683	683 (w) T 685 (w) H	686 (m)
20	695	695 (m) H 697 (m) M	

21	722		722 (m)
22	746	746 (vw) M 748 (w) T	
23	753	751 (vw) H 753 (m) M 756 (s) H	
24	768	766 (w) H 770 (w) T	
25	809		809 (vw)
26	834	834 (s, vs) H, T	
27	854	849 (vw) M 853 (vw) H 856 (m) T 859 (vw) H	861
28	884		884
29	944		944 (vw)
30	964	964 (vw, vw, w) M, H, T	
31	975	973 (w) H 976 (vw) M, H 977 (vw) T	
32	981	981 (vw) H	

33	1023	1021 (m) T 1022 (w) M 1023 (w) H 1025 (m) H	1017 (w)	1024
34	1038	1038 (m) H 1039 (vw, vw, w) M, H, T	1032 (w)	
35	1083	1083 (m) M 1085 (m) H	1051 (m)	
36	1095	1093 (m) H 1098 (m) T		
37	1109	1107 (w) H 1109 (vw) M 1111 (vw) T		
38	1120			1120
39	1131		1131 (s)	
40	1144			1144
41	1163		1163 (w)	
42	1185	1180 (s) M 1182 (s) H 1185 (vw) H 1186 (vw) T 1190 (s) M 1191 (s) H		

43	1199		1199 (vw)		
44	1231			1231	
45	1255	1255 (vs) T 1258 (vs) H			
46	1268		1268 (vw)		
47	1299	1299 (vw) M 1300 (w) H 1301 (m) T 1302 (m) H	1291 (s)		
48	1329			1329	
49	1340	1340 (s) M 1340 (s) H			
50	1351		1351 (m)		
51	1370				1370
52	1383	1377 (s) T 1380 (w) H 1383 (m) M 1386 (s) H 1390 (vs) T			
53	1399	1399 (m) H			
54	1412			1412	1412
55	1426		1426 (vw)		



56	1482	1480 (vw, w) M, H 1481 (w) T 1483 (vw) H		1478
57	1504		1504 (w)	
58	1540		1540 (vw)	
59	1562	1561 (w) H 1562 (s) T 1563 (m) H 1564 (m) M		
60	1572			
61	1602	1598 (w) M, T 1599 (w) H 1606 (w) H		1597
62	1615		1615	1616
63	1651		1651 (vs)	
64		1740 (vs) T		
65	1710		1710	1712
66	1757	1757 (vs) H		
67	1785	1783 (vs) M 1788 (vs) H		

68	2350		2350	
69	2973	2968 (m) H 2971 (w) H 2972 (m) M, T 2975 (w) M, T 2978 (w) H		
70	3003	3003 (vw) H		
71	3013	3011 (vw) M 3012 (vw) H 3013 (vw) M, T 3014 (vw) H 3015 (vw) T 3016 (vw) H		
72	3023		3022 (w) 3024 (vw)	
73	3058		3055 (vw) 3061 (vw)	3054
74	3072			3072
75	3084			3084
76	3102			3104
77	3266	3266 (vs) H		
78	3347	3347 (vs) T		

79	3436			3436
80	3526		3526 (m)	
81	3568	3568 (s) H 3570 (s) M		
82	3633			

Comparing the computational IR active vibrational data of the INA monomer to the INA dimer, several distinct IR modes/features unique to the hydrogen bonding H-T INA and T-T INA are identified. For the H-T dimer, at least four new normal modes appear (3266, 1757, 1258 and 834  $\text{cm}^{-1}$ ) and are all in-plane except for the last mode. The 3266  $\text{cm}^{-1}$  mode is primarily the O-H stretch along the  $\text{N}\cdots\text{H}-\text{O}$  direction  $\nu(\text{N}\cdots\text{H})$  with some rocking of the carbonyl carbon  $\delta(\text{C}=\text{O})$ , and having a dipole moment gradient  $\approx 30^\circ$  to the HB direction. The 1757  $\text{cm}^{-1}$  mode is predominately the carbonyl stretch  $\nu(\text{C}=\text{O})$  in conjunction with the hydroxyl rocking  $\delta(\text{O}-\text{H})$  about the dipole moment gradient perpendicular to the HB direction. Like the 1757  $\text{cm}^{-1}$  mode, the 1258  $\text{cm}^{-1}$  also features the dipole moment gradient perpendicular to the HB direction and carbonyl stretching  $\nu(\text{C}=\text{O})$  but includes  $\alpha$ -carbon stretches  $\nu(\text{C}_{\text{C}=\text{O}}-\text{C}_\alpha)$  and significant wagging of both carbonyl  $\delta(\text{C}=\text{O})$  and hydroxyl  $\delta(\text{O}-\text{H})$ , and less so of  $\beta$ -carbon hydrogens  $\delta(\text{C}_\beta-\text{H})$  and non-bonded hydroxyl as well. The 834  $\text{cm}^{-1}$  mode is the out-of-plane O-H wagging  $\gamma(\text{N}\cdots\text{H})$  perpendicular to the  $\text{N}\cdots\text{H}-\text{O}$  direction, with a dipole moment gradient perpendicular to the HB direction in the direction of the wagging motion.

There is also broadening of some of the H-T IR active modes, in particular in-plane stretching of the C-C bonds of the ring atoms  $\nu(\text{C}-\text{C})$  and rocking of carbon hydrogens  $\delta(\text{C}-\text{H})$  and of all carboxylic acid atoms  $\delta(\text{C}=\text{O})$ ,  $\delta(\text{C}-\text{O})$ ,  $\delta(\text{O}-\text{H})$  at 1386  $\text{cm}^{-1}$  where the dipole moment gradient is  $\approx 45^\circ$  to the HB direction. Broadening also occurs at 1093  $\text{cm}^{-1}$  where the dipole moment gradient is also  $\approx 45^\circ$  to the HB direction. There a breathing mode of one of the INA molecules occurs while its partner undergoes

stretching  $\nu(\text{C}-\text{C})$ ,  $\nu(\text{C}-\text{H})$ ,  $\nu(\text{C}-\text{N})$  and rocking of the ring atoms  $\delta(\text{C}-\text{C})$ ,  $\delta(\text{C}-\text{N})$  including the hydrogens  $\nu(\text{C}-\text{H})$ , in conjunction with carbonyl carbon and hydroxyl oxygen stretching  $\nu(\text{C}_{\text{C=O}}-\text{O}_{\text{O-H}})$ . In the far IR at  $437\text{ cm}^{-1}$ , both molecules of the dimer undergo out-of-plane wagging  $\gamma$  of all the atoms as if there is flexing of the molecules across their molecular axis. As expected, the dipole moment gradient is perpendicular to the HB direction. For the T-T IR normal modes, the signature of the dimer motifs is different.

For the T-T dimers, there appears more dramatic frequency shifting and reverse-broadening in addition to new normal modes in which three appear ( $3347$ ,  $834$  and  $250\text{ cm}^{-1}$ ). The  $3347\text{ cm}^{-1}$  mode is primarily the in-plane asymmetric stretch of the two hydroxyls  $\nu(\text{O}\cdots\text{H})$  with minimal hydroxyl oxygen rocking about the carbonyl carbon  $\delta(\text{C}_{\text{C=O}}-\text{O}_{\text{O-H}})$ . It has a dipole moment gradient along the HB direction. The  $834\text{ cm}^{-1}$  mode is out-of-plane wagging of the hydroxyl pairs  $\gamma(\text{O}-\text{H})$  and ring hydrogens  $\gamma(\text{C}-\text{H})$  with a dipole moment gradient perpendicular to the HB direction. The far IR  $250\text{ cm}^{-1}$  mode is the in-plane rocking of the carboxylic acid pair  $\delta(\text{C}=\text{O})$ ,  $\delta(\text{O}-\text{H})$  as single units about their basal plane, having a dipole moment gradient nearly perpendicular to the HB direction.

The apparent frequency shift accompanied by over 100 % increase in intensity are the pair of  $1390$  and  $1255\text{ cm}^{-1}$  lines, blue-shifted by ca.  $62\text{ cm}^{-1}$ . At  $1390\text{ cm}^{-1}$ , the in-plane rocking of the hydroxyl hydrogens  $\delta(\text{O}-\text{H})$  along with carbon  $\nu(\text{C}-\text{C})$  and hydrogen

$\nu(\text{H}-\text{C})$  stretches of ring atoms, rocking of ring hydrogens  $\delta(\text{C}-\text{H})$  and stretches of hydroxyl oxygen  $\nu(\text{O}-\text{H})$  and carbonyl carbon  $\nu(\text{C}=\text{O})$  occur with a dipole moment gradient approximately along the HB direction. At  $1255\text{ cm}^{-1}$ , in-plane rocking of the hydroxyl pair  $\delta(\text{O}-\text{H})$ , C-C bonds  $\delta(\text{C}-\text{C})$  and ring hydrogens  $\delta(\text{C}-\text{H})$  accompanied by stretching between carbonyl carbon and  $\alpha$ -carbon  $\nu(\text{C}_{\text{C=O}}-\text{C}_{\alpha})$ , between hydroxyl oxygen and carbonyl carbon  $\nu(\text{C}_{\text{C=O}}-\text{O}_{\text{O-H}})$ , and minimally along carbon  $\nu(\text{C}-\text{C})$  and nitrogen  $\nu(\text{N}-\text{C})$  bonds occur. Not surprising, the dipole moment gradient is  $\approx 45^\circ$  from the HB direction.

Another noticeable frequency shift for the INA T-T dimer occurs at  $1740\text{ cm}^{-1}$  where the line is red-shifted and the dipole moment gradient  $\approx 45^\circ$  from the HB direction. At that frequency, there occurs carbonyl stretching  $\nu(\text{C}=\text{O})$  as well as in-plane rocking of the hydroxyls  $\delta(\text{O}-\text{H})$ , of carbonyl carbon about the  $\alpha$ -carbon  $\delta(\text{C}_{\text{C=O}}-\text{C}_{\alpha})$  and minimally, of the hydrogens  $\delta(\text{C}-\text{H})$  and ring atoms  $\delta(\text{C}-\text{C})$ ,  $\delta(\text{N}-\text{C})$ . At  $1562\text{ cm}^{-1}$ , the frequency shift is minimal in comparison but the intensity increases over 100 % and the in-plane asymmetric stretches of the carbonyls  $\nu(\text{C}=\text{O})$  and rocking of the hydrogens  $\delta(\text{C}-\text{H})$  and ring atoms  $\delta(\text{C}-\text{C})$ ,  $\delta(\text{N}-\text{C})$  occur. The two molecules vibrate in-phase and increase the vibrational intensity of a single monomer due to a dipole moment gradient  $\approx 45^\circ$  from the HB direction. At  $631\text{ cm}^{-1}$ , something different happens. At  $631\text{ cm}^{-1}$ , there appears reverse-broadening in which the band about the central frequency is sharper due to a dipole moment gradient  $\approx 45^\circ$  from the HB direction. Here, the in-plane motion resembles line tension applied along the molecular

axis in which the atoms of one molecule vibrates symmetrically from corresponding atoms in its dimer partner  $\nu, \delta$ .

Frequency modes computed for the INA monomer and dimer conformers allow identification of those frequencies unique for the INA cluster type, as well as intensity, broadening and shifts in frequency of free INA. 3266  $\text{cm}^{-1}$  (H-T dimer) and 3347  $\text{cm}^{-1}$  (T-T dimer) IR active modes do not appear in the free INA spectra, and make it possible to identify the dimer type. However adsorption of INA onto a flat Ag substrate lies parallel to the surface, thus rendering the change in the transition dipole moments  $\Delta\vec{\mu}$  (nearly if not exactly) parallel to the surface as well, making the vibrational signal IR inactive. For these strong near IR region modes, they are not observable and so modes with a  $\Delta\vec{\mu}$  having a component perpendicular to the surface are needed. These modes are not unique to INA dimers, so less redeeming features such as broadening, intensity or shifts from the free INA are sought instead to identify these perturbed frequencies.

IR spectroscopic measurements of INA within the wavelength region of interest are limited to  $\sim 800\text{-}3450 \text{ cm}^{-1}$  range. Certain bands obtained from the computations of the gas phase INA monomers and dimers are within  $\pm 5 \text{ cm}^{-1}$  with experimentally obtained IR of INA in the solid state phase[29, 97]. The mid-range  $\nu_0$  values are 1023, 1482, 1602 and 3058  $\text{cm}^{-1}$ , and they all characterize monomer as well as the dimer motifs, with a possible exception of the near-IR 3058  $\text{cm}^{-1}$  frequency (Table 3.4). Based on these experimental results, small dimer chains *may* occur, since the adsorption of only INA monomers cannot be ruled out. Considering the fact that the electron density of INA

chain structures adsorbed on Ag (111) have been imaged, the IR experimental data is consistent with INA chain formation. Unfortunately, the distinguishing fingerprint unique to INA H-T/T-T dimers have not been observed. This is due to the selection rules and how the molecule orients itself to be IR measurable rather than the occurrence of chain formation.

### 3.4. CONCLUSION

HF and DFT with moderate basis sets were the levels of theory used to provide reasonable geometries, and electronic properties of INA, as well as to furnish coefficients of the orbitals forming the wavefunction required by ORIENT4.5 as shown in Tables 3.1-3.3. INA computations at the HF level of theory provide geometries and supermolecule interaction energies of this and similar dimerized molecules at a low cost. The approximate geometries of INA are sufficient to estimate similar N-heteroaromatics and their dimers, such as ACA, and can serve as reasonable starting configurations for more complex molecular structures that dimerize. MP2 with a larger basis set is the minimum level of theory needed to compute vibrational frequencies of hydrogen bonded dimers and serve as a benchmark for the HF calculations. The AAAIP methods provide efficient ways to compute crystal packing structures of molecular systems, in this case INA,



requiring the *ab initio* or DFT computation of only a single molecule. All of these computational methods were used to predict the geometry, energy and electrostatic moments of the monomer and dimer conformer structure of INA. To predict the stability of chain structures of INA, AAAIP and MMA was implemented to find the minimum free energy of these molecular systems held together by predominately electrostatic forces, and as a final check, the vibrational (IR active) spectra of INA monomers and dimers were calculated.

By first investigating the two different INA HB motifs in the gas phase by *ab initio* and AAAIP methods, the dimerization energies and geometries were determined. An upper limit of the short-range energy  $\Delta E_{\text{SR}}$  of these dimers was found to be  $\sim 65\%$  of the total supermolecule interaction energy. This overestimates the short-range energy because the HB length in the AAAIP calculation is too long. Then in a systematic patterning scheme, the intermolecular energy of H-T and T-T type chains were investigated and H-T chain types preferred for long chains. For T-T type chains at shorter lengths, there was no preference as to how they grew but only the necessity that they grow in *pairs*. To establish the driving force behind preferred chain structures, the strength of pairwise molecular multipole moments involved in the interactions were examined and an orbital mode picture emerged.

For the H-T dimer, the dipole-octopole and quadrupole-quadrupole interaction were predominate, while the dipole-quadrupole interaction was predominate for T-T dimers both at optimum molecular separation. The dominant modes for the T-T dimer remained

the same throughout the entire molecular separation range of  $\approx 15 - 55$  Bohr, while the dominant modes for the H-T case crossover at  $\approx 35$  Bohr. Despite the errors associated with the MMMA method, the identification of which *molecular* multipole-multipole modes dominate is not ambiguous but definitive.

Though the MP2 provided more better molecular orbitals and consequently, improved HB lengths, energies and vibrational frequencies, an accurate scaling factor for INA HF vibrational computations INA was necessary for the more demanding dimer conformer calculations. Tested against MP2 monomer vibrational values, the calibrated HF values were in very good agreement.

IR spectroscopic measurements of INA within the wavelength region of interest however is limited, making it difficult to compare the IR vibrational data. Certain bands obtained from the computations of the gas phase INA monomers and dimers are within  $\pm 5 \text{ cm}^{-1}$  with experimentally obtained IR of INA in the solid state phase[29, 97]. The mid-range  $\nu_0$  values are 1023, 1482, 1602 and  $3058 \text{ cm}^{-1}$ , and they all characterize monomer as well as the dimer motifs, with a possible exception of the near-IR frequency  $3058 \text{ cm}^{-1}$ . Based on these experimental results, small dimer chains *may* occur, since the adsorption of only INA monomers cannot be ruled out. This is supported by experimental STM topography imaging of INA chain structures adsorbed on Ag(111)[96].

MMMA in conjunction with AAAIP can account for both molecular and atomic details such as equilibrium structures, atom-atom interaction strengths and molecular multipole

moment competition. The methods provide reasonable estimates of the electrostatic energy of a system of molecules by considering pairwise atomic multipole moment interactions that take into account the anisotropic intermolecular potential, particularly for 2-D crystal packing structures. By using AAAIP to investigate the length dependent chain type systems, the preference for one type chain over another, as well as the method of association involved in forming that particular chain type system, can be determined. This is of particular importance for understanding the morphology of molecular chains in supramolecular structures.

## Chapter 4

### **Molecular and Crystal Structure of Supramolecular 9-Acridinecarboxylic Acid Dihydrate: Whole-Molecule Disorder**

#### ABSTRACT

Crystals of the title compound,  $C_{13}H_9NO_2 \cdot 2H_2O$ , are built up of 9-acridinecarboxylic acid and water molecules. The acridine derivatives form linear chains of head-to-tail hydrogen bonding networks along the *a*-axis and  $\pi$ - $\pi$  intermolecular bonding in the transverse directions. The water molecules form a two-dimensional hydrogen bonding network in the traverse direction, bridging carboxyl groups of the acridine derivative. Two units related by glide plane symmetry interact through a pair of  $\pi$ - $\pi$  electrostatic interactions of the acridine basal planes, forming edge-face and offset stacked geometries. Diffraction data shows that the direction of the head-to-tail chains flipped randomly to form two different packings in about a 3:2 ratio, manifesting whole-molecule disorder.

#### 4.1. INTRODUCTION: SOLID STATE 9-ACRIDINECARBOXYLIC ACID

This present work is an extension of our surface science investigation on the characterization of the 2-dimensional adlayer phase of N-heteroaromatic 9-acridinecarboxylic acid. These molecules form dimer motifs and noncovalent supramolecular architectures via multiple hydrogen bonds and  $\pi$ -bonding networks since they contain arrays of hydrogen bonding, as well as edge-face and offset stacked  $\pi$ - $\pi$  interactions in 3-dimensional crystals. Our interest in these types of compounds arises from their multifunctional application such as their use as dopants in C<sub>60</sub> fullerene films[20, 21], fluorescence probes[18, 19], and photosensitive binding agents to DNA[22].

In order to expand the understanding of the condensed stated physical-organic chemistry of these rigid backbone compounds that form N $\cdots$ H-O and O $\cdots$ H-O H-bonded networks involving  $\pi$ - $\pi$  intermolecular bonding, we present here the structure of 9-acridinecarboxylic acid dihydrate obtained from diffraction data, and compare it to the structure predicted for isolated 9-acridinecarboxylic acid molecule and its head-to-tail (H-T) dimer via DFT fully optimized geometry calculations. The results are interpreted in terms of the intermolecular interaction forces responsible for many highly ordered hydrogen bonded systems.

## 4.2. EXPERIMENTAL

### 4.2.1. Synthesis

9-acridinecarboxylic acid hydrate (99%) was dissolved in neat ethanol at room temperature. After 72 hours, yellow crystals formed through slow evaporation and were suitable for single-crystal X-ray diffraction analysis.

### 4.2.2. X-ray Diffraction and Crystal Structure Determination Description

X-ray diffraction data was collected and the crystal structure determined by Dr. Peter Zavalij using a SMART 1000 three-circle diffractometer at the Chemistry & Biochemistry Department X-Ray Crystallographic Center facility at University of Maryland. The crystal structure was solved in the non-centrosymmetric Pc space group, and a model of two superimposed 9-acridinecarboxylic molecules provided an R factor less than 4.0 % to explain the presence of a shadow molecule. In that case, the ratio of occupation factors for both molecules was 0.593(5) : 0.407(5). A second model of two superimposed 9-acridinecarboxylic acid molecules, where one is flipped relative to the other, was also tested. In that case, the crystal was solved in the centrosymmetric P2<sub>1</sub>

space group with an R factor of 4.2 %, and a ratio of occupation factors of 1: 1. Displacement ellipsoids of the main molecule are shown in Figure 4.1a, while superimposed molecules are depicted in Figure 4.1b. Thus the title structure presents the case of whole-molecule disorder, which is discussed below. Details of the x-ray diffraction procedure and crystal structure determination can be found in APPENDIX E: X-ray Diffraction Details. The diffraction data is presented in APPENDIX F: Table F.1. X-ray Diffraction Data.

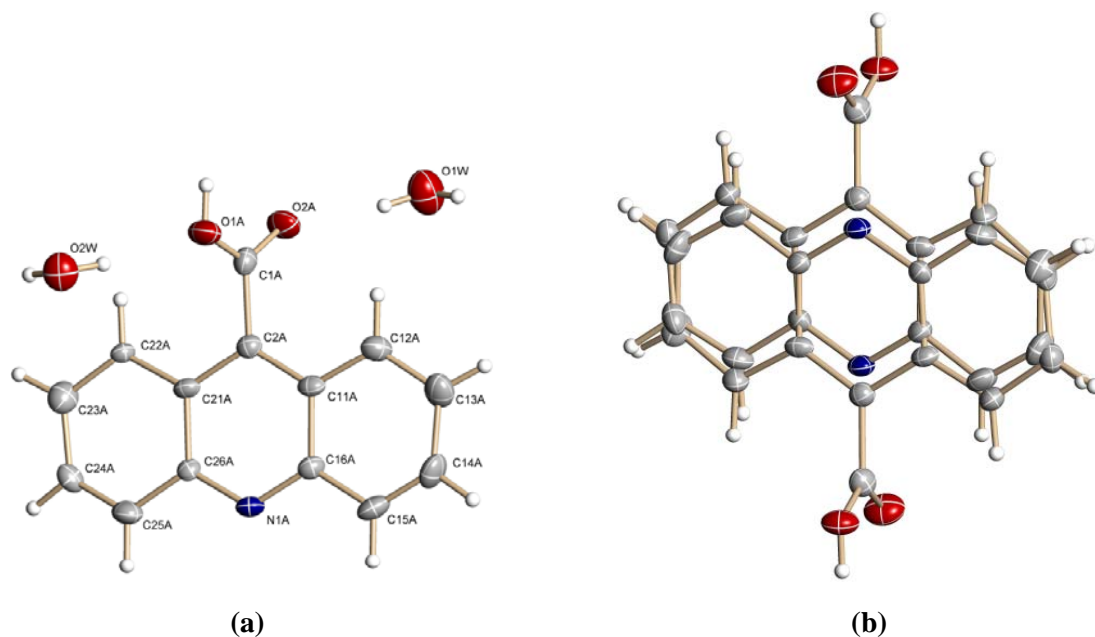


**Figure 4.1.** (a) Molecule 9-acridinecarboxylic acid with two water molecules labeling scheme and (b) superimposed molecules 9-acridinecarboxylic from the whole molecule disorder are shown. Atomic displacement ellipsoids of both (a) and (b) are shown at the 30 % probability level.

### 4.3. DFT COMPUTATIONS

Using quantum chemistry density functional theory (DFT) methods, the molecular orbitals (MOs) of neat (with no water molecules present) 9-acridinecarboxylic acid monomer and its H-T dimer were calculated and geometries optimized at the B3LYP/6-311G(d,p) and B3LYP/6-31(d) level of theory, respectively[94]. Due to the sensitivity which optimized structures often have on their initial configurations, initial atomic displacements resembling similar structures or their composites obtained from diffraction data libraries[98] or computational results[99] were used. From the stable molecular structures found, the bonding lengths and angles are given in Figure 4.2a and the dipole moments are described below.



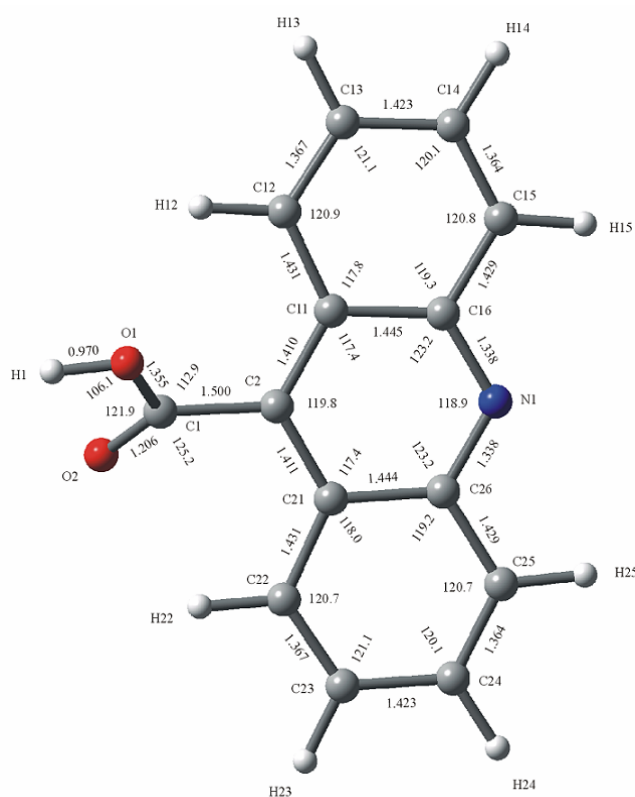


**Figure 4.2a.** Results of the optimized molecular orbital calculation ( $\text{\AA}$ ) for 9-acridinecarboxylic acid.

#### 4.3.1. DFT Geometries

The DFT gas phase geometries calculated for the isolated 9-acridinecarboxylic acid show a fused ring system with a smaller internal C-N-C angle of  $118.9^\circ$  compared to that of benzene, and the  $\alpha$ -carbon of the carboxyl group is lifted out of the basal plane by  $0.67(32)^\circ$  [ $\text{C26-C21-C2-C1} = -179.55^\circ$  and  $\text{C16-C11-C2-C1} = -179.10^\circ$ ] and rotated about the C-C bond by  $48.8(10)^\circ$  [ $\text{C21-C2-C1-O1} = 49.577^\circ$  and  $\text{C11-C2-C1-O1} = 48.088^\circ$ ].

The nitrogen lone-pair electrons are predicted by the valence-shell electron-pair repulsion (VSEPR) theory to occupy more space and therefore exert a larger repulsion than do its

bonding electron pairs. The alternating C-C bond lengths around the three rings of 9-acridinecarboxylic acid is a feature of heteroaromatic conjugated systems[100], i.e., [C12-C13=1.367 Å, C13-C14=1.423 Å, C14-C15=1.364 Å], due to the charge density change which a heteroatom has on its neighbors charges[101].

In the MO calculation, molecules in the H-T dimer have a relative twist of  $59.095^\circ$  [C2-C6-C7-C3=65.508 and C7-C3-C2-C6=52.682°] and tilt in toward each other. The hydrogen bonding length N...H is 1.81445 Å with a hydrogen bonding angle N...H-O of  $164.053^\circ$ . This is shown in Figure 4.2b where one molecule is labeled 1-26 and its dimer partner is labeled 27-52. Computed angles for the monomer and H-T dimer are within 1% of each other.

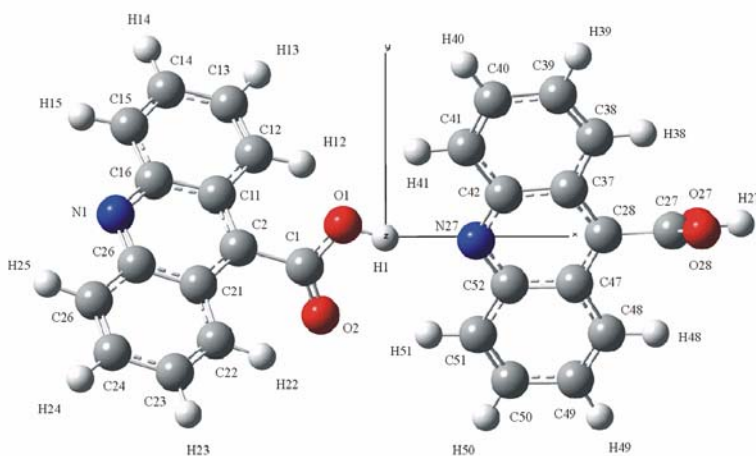


**Figure 4.2b.** Results of the optimized molecular orbital calculation (Å) for the 9-acridinecarboxylic acid H-T dimer.

#### 4.3.2. DFT Dipole Moments

Both the 9-acridinecarboxylic acid monomer and H-T dimer have non-trivial dipole moments. For the monomer, the dipole moment is 1.555 D that lies near equally along all 3 axes, while for the H-T dimer is 5.0173 D that lies 90 % along the acceptor-donor hydrogen bond direction.

#### 4.4. DISCUSSION

Here the crystallographic data and quantum chemistry computations are compared and the hydrogen bonding network is discussed.

##### 4.4.1. Crystal Structure

The asymmetric unit consists of a 9-acridinecarboxylic acid molecule and two water molecules. The  $\alpha$ -carbon of the carboxyl group is lifted out of the basal plane by  $0.10(2)^\circ$  and rotated about the C-C bond by  $77.6(6)^\circ$ . The two rigid acridine backplanes in the cell are in an edge-face geometry in the b-c plane and together with the four water molecules form a two-dimensional hydrogen bonding network between each other and the acridine derivatives.

Molecules of acridinecarboxylic acid are connected by intermolecular COOH...N H-bonds to form infinite chains along the a-axis (Figure 4.3). Two water molecules present in the structure alternate along the c-axis to form H-bonded zigzag chains. In addition, the water molecules form H-bonds with the carboxylic groups yielding a 3-dimensional network of H-bonds.

It is highly unlikely that the disorder occurs within the chain, otherwise T-T configurations would occur as well. Instead, a model of random H-T orientations of the chains describes the diffraction data more accurately.

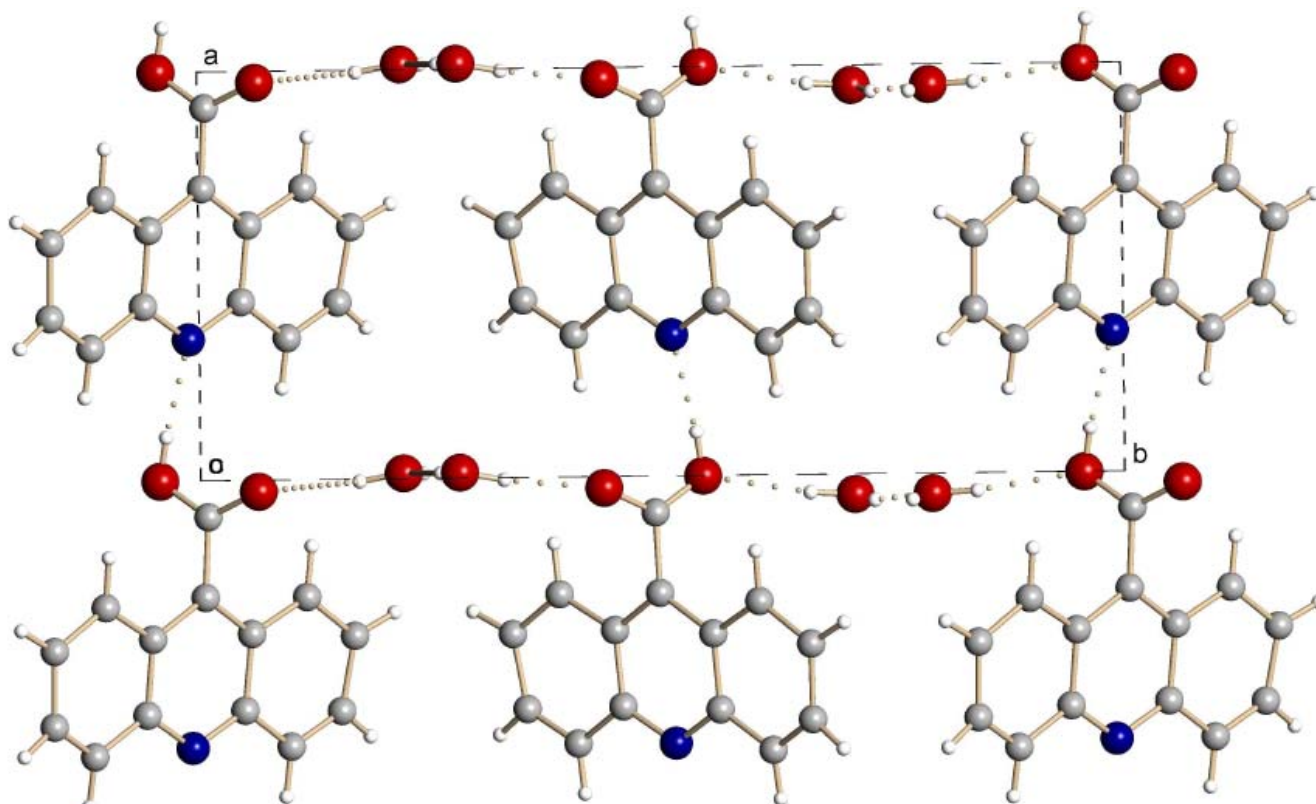


**Figure 4.3a.** Packing diagram shown looking down the c-axis is shown. Chains of H-bonded molecules are equally directed.

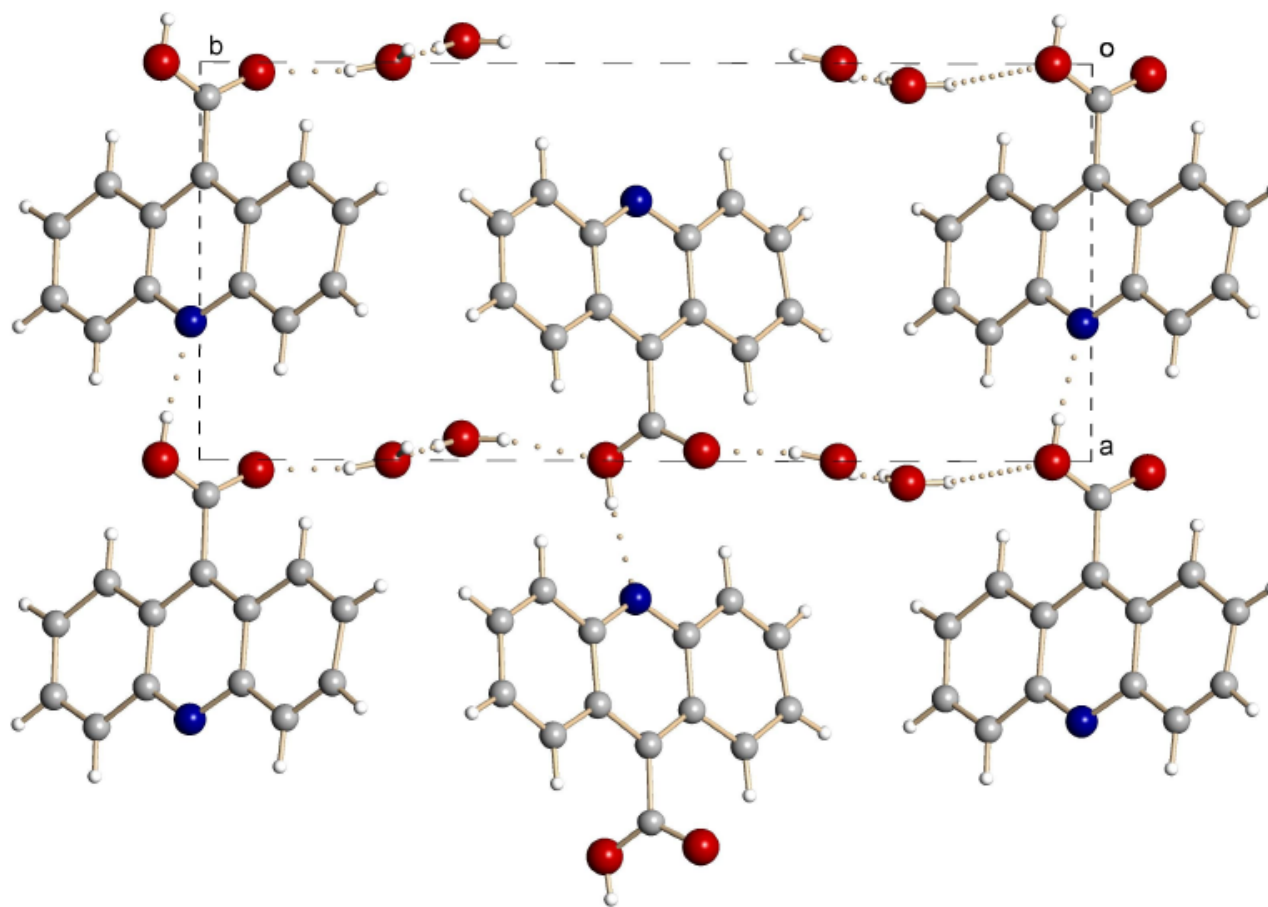


**Figure 4.3b.** Packing diagram shown looking down the c-axis with alternating chains of H-bonded molecules is shown. This is a plausible arrangement of consecutive chains in the 3:2 ratio of alternating chains.

Models of equally oriented and alternating chains are shown in Figure 4.3a and 4.3b, respectively. Interestingly, equally oriented chains are described by the  $Pc$  space group, while alternating chains are described by the  $P2_1$  group. It is worth noting that in both models the position of water molecules and H-bonds are practically identical, and the shape of the COOH...N H-bonded chains are very similar. The main difference between the two models is the orientation of COOH...N H-bonds. But because they are hidden in the middle of the chains and have a minimal effect on the crystal packing, whole-molecule disorder[102] of the structure occurs.

#### 4.4.2. Comparison: Crystallographic and Computational Molecular Geometries

The B3LYP/6-311G(d,p) level of theory computation predictions of individual 9-acridinecarboxylic acid molecules are within 3 % of the crystal structure geometries, i.e., [C2-C11=1.407(11) Å, C11-C16=1.425(5) Å, C16-N1=1.356(13) Å; C12-C13=1.405(15) Å, C13-C14=1.415(7) Å, C14-C15=1.315(17) Å]. The ring is less distorted with the alternating bond lengths and more mild than the calculation values. C2 and C11 are nestled between the rings with the carboxylic group extending in front. The C2-C11 bond length differs from the calculated value by only 0.003 Å, suggestive that the remaining bond length deviations are due to the effect which the water molecules have overall on the electron density of the aromatic ring.

The alternating bond lengths and distortion of the nitrogenous base (with an acidic substituent) of neat 9-acridinecarboxylic acid is due primarily from the delocalized  $\pi$ -electron density of the ring affected by heteroatom, N, and less so, to carbonyl's  $\beta$ -carbon, in which case the charge density is no longer unity on each atom. The alternating C-C bond lengths from the crystallographic data are less exaggerated than neat 9-acridinecarboxylic acid, consistent with charge density change that is stabilized by presence of the water molecules[103], and is important because it affects the electrostatic intermolecular interactions which in turn is responsible for hydrogen bonding networks[104].

The  $\alpha$ -carbon of the carboxyl group is virtually in the basal plane, the same as for the computation, however its rotation about the C-C bond differs significantly from the calculation by  $27.3^\circ$ . This suggests that the rotational potential cost is compensated by the free energy decrease upon formation of the 2-dimensional hydrogen bonding network introduced by the hydrating water[105].

The measured internal C-N-C angle of  $121.2(7)^\circ$  is reminiscent of additional in-plane  $\pi'$  conjugation with two new "d-atom" orbitals  $d_{xy}$  and  $d_{x^2-y^2}$  occurring as the angle opens up, and roughly one of the two  $\sigma$  lone-pair electrons is transferred from the nitrogen into the conjugated system[100], extending the charge distribution further into the ring and promoting  $\pi$ - $\pi$  interaction between the two acridine derivative backplanes. This in turn is important because the charge density distribution changes affect the electrostatic interactions that help govern long-range order.



For two adjoining cells, the two acridine backplanes have both an edge-face and offset stacked geometry in the b-c plane and a nearly coplanar geometry in the a-b plane. The edge-face stacked acridine backplanes repeat every 7.7 Å, forming two sets of offset stacked acridine backplanes at  $\pm 42^\circ$  to the c-axis. The nearly coplanar acridine backplanes are rotated slightly out of the a-b plane, forming rows of H-T molecular chains along the a-axis (Figure 4.4a). In the b-c crystal plane, the edge-face and offset stacked acridine backplanes form a herringbone structure with intercalated water molecules forming a 2-dimensional hydrogen bonding network that straddles the acridine backplane (Figure 4.4b). This hydrogen bonding network always involves a water molecule and is distinct from the linear hydrogen bonding network formed between donor and acceptor sites of 9-acridinecarboxylic acid molecules. H-T hydrogen bonding between the acceptor and donor sites of the acridine derivative occur along the a-axis with a *ca.*  $11^\circ$  tilt, forming a N...H-O bond of length 1.88 Å, significantly longer than the MO dimer calculation of 1.814 Å. Bonding lengths between carboxyl carbon and hydroxyl oxygen, and between hydrogen and oxygen of the hydroxyl group are also significantly less than from the isolated gas phase calculation [C1-O1 = 1.255(7) Å and O1-H1 = 0.830 Å]. The bond length differences suggest that charge has been redistributed to the aromatic ring, leading in part to a stronger acceptor-donor hydrogen bond.

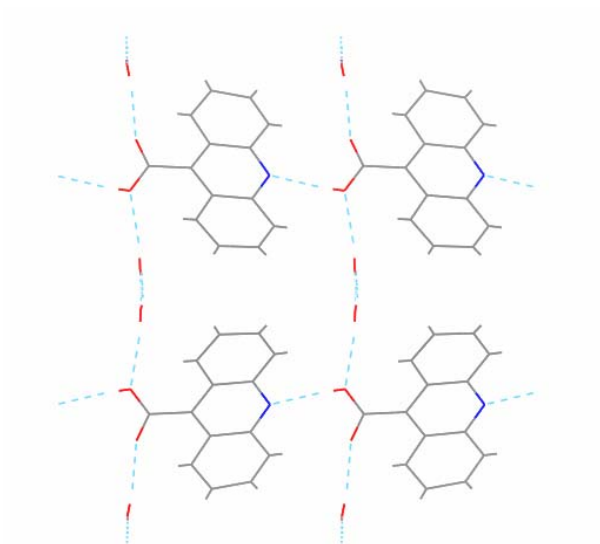


**Figure 4.4a.** H-T molecular chains along the a-axis direction.

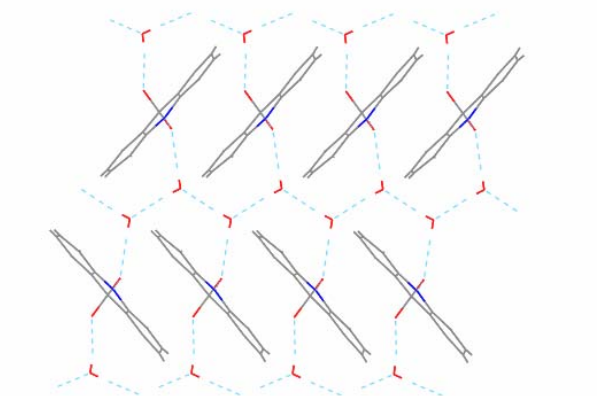


**Figure 4.4b.** In the b-c plane, herringbone structure of ACA and water molecules form a 2-dimensional hydrogen bonding network.

The 3-dimensional crystal of 9-acridinecarboxylic acid dihydrate is composed of 9-acridinecarboxylic acids directly coupled pair-wise to each other (predominately by quadrupole-quadrupole interactions) and by acceptor-donor hydrogen bonding, and through water molecules directly coupled to each other and to the acridine derivative

through both the carbonyl and hydroxyl oxygen groups. The hydrogen bonds between 9-acridinecarboxylic acids form linearly networks along the N...H-O chain direction, with acridine derivative backplanes offset displaced. Water molecules form a 2-dimensional network nearly perpendicular to the acridine acceptor-donor hydrogen bonding network, forming two 2-dimensional nets each partially shrouding the acridine backplane to form a larger 'S' shaped net about the entire acridine backplane. The well ordered structure of close-packed N-heteroaromatic 9-acridinecarboxylic acid dihydrate is influenced by electrostatic intermolecular interactions[104, 106] and the effect on its hydrogen bonding networks.

In both Pc and P2<sub>1</sub> crystal packings, the acceptor-donor hydrogen bond network is a linear chain of 9-acridinecarboxylic acid prochiral molecules. In the Pc case, neighboring H-T chains ( equally directed) are enantiomers (Figure 4.3a), while in the P2<sub>1</sub> case, neighboring H-T chains (alternating direction) are diastereomers (Figure 4.3b). In either case, each molecule within its chain is edge-face to another molecule in the neighboring chain as well as offset stacked to yet a third molecule in its neighboring chain (Figure 4.4b). This permits multiple quadrupole-quadrupole intermolecular interactions. Since Pc crystal packing is favorable by 3:2, the diastereomer chains are preferred in the H-T chain arrangement.

The preference for alternating rather than same chain direction can be understood by comparing the crystallographic results to 9-acridinecarboxylic acid monolayer films on Ag (111)[30]. In that case, ordered H-T chains formed in the same direction, not affected

by polarity of the adlayer because of metal surface screening. In the crystal however, whole-molecule disorder reduces the polarization by flipping the molecular chain direction.

## Chapter 5

### STM and XPS Data of Adlayer Structures of N-Heteroaromatics on Ag (111) Perspectives

The experimental results of this Chapter have been published in the following journal articles: Bo Xu, Bindhu Varughese, Diane Evans, and Janice Reutt-Robey, "*Morphology Selected Molecular Architecture: Acridine Carboxylic Acid Monolayers on Ag (111)*" J. Phys. Chem. B 110, 1271-1276 (2006); Li, H., Xu, B., Evans, D., Reutt-Robey, J. E., "*Isonicotinic Acid Molecular Films on Ag (111): I. XPS and STM Studies of Orientational Domains*" J. Phys. Chem. C 111, 2102-2106 (2007); Xu, B., Tao, C., Williams, E. D., Reutt-Robey, J. E., "*Coverage Dependent Supramolecular Structures: C<sub>60</sub>: ACA Monolayers on Ag (111)*" J. Am. Chem. Soc. 128, 8493-8499 (2006).

#### ABSTRACT

Adlayer structures of N-heteroaromatics isonicotinic acid (INA) and 9-acridinecarboxylic acid (ACA) formed on Ag (111) at room temperature through self-assembly are

investigated using scanning tunneling microscopy (STM) and x-ray photoelectron spectroscopy (XPS). Observed phases for both ACA and INA are consistent with chain type computational results, and their dimer geometries strikingly similar. The multipole moments that drive ACA and INA to form ordered structures electrostatically provide insight to the dynamics of these self-organized organic monolayers.

## 5.1. INTRODUCTION: SUPRAMOLECULAR SURFACE CHEMISTRY

The emergence of nanotechnology has ignited a “bottom-up” approach to nanofabrication for device miniaturization and molecular electronics[107-111]. One particularly important “bottom-up” strategy utilizes molecular self-assembly to create surface nanostructures[111-113]. Surface nanostructures are particularly suitable for applications involving catalysis, sensing, and optoelectronic signaling due to their accessibility to ambient chemical species and to electric and optical contacts.

Research on self-assembled monolayers has particularly proliferated since alkanethiol monolayers were first characterized on Au surfaces[114]. Redox properties (e.g., porphyrin and their derivatives[115, 116]), electronic properties (e.g., pentacene and polyacenes[117-119]) and optical properties (e.g., porphyrin[120]) of chemically distinct

monolayer films have been explored. While reported research has emphasized the study of functional monolayers, supramolecular surface chemistry remains to be fully exploited to fabricate nanostructures with prescribed lateral dimension and molecular architectures.

Three kinds of non-covalent interactions are most important in supramolecular organization: hydrogen bonding[31, 121, 122], metal-ligand interaction[123], and dipole-dipole interaction[33]. The high selectivity and directionality of hydrogen bonding, key factors in biological assemblies, can also be utilized to form surface nanostructures through self-assembly process. When supramolecular organization occurs at surfaces, self-assembled structures will be stabilized by both intermolecular and molecular-substrate interactions. Understanding the hierarchy of these interactions is essential for developing nanostructures with tailored properties. For example, chromophores with anisotropic interactions offer the possibility to form oriented molecular films with enhanced optoelectronic properties. While such anisotropic molecules have often lead to the production of disordered films, organization on the nano-meso scale has been readily observed[31, 33, 111-113, 121-123].

In this Chapter, we explore how anisotropic molecular interactions, in combination with substrate morphology, yield distinctive molecular film architectures and interpret them in terms of the H-T and T-T type chain analysis based upon gas-phase calculations.

Although ACA-ACA and INA-INA intermolecular interactions are somewhat weaker (<30%) than the chemisorption energy, they should contribute significantly to the adlayer structure because of their strong orientational dependence. The chain type

analysis should provide a figure of merit for interpreting the experimental results of adlayer architecture.

## 5.2. EXPERIMENTAL MATERIALS AND METHODS

### 5.2.1. Materials

The Ag (111) substrates were first prepared by vapor deposition on mica substrates[124]. The initially prepared Ag substrates (300 nm thick) were transferred in air to the two separate UHV systems for STM and XPS measurements. All subsequent sample preparations were conducted under vacuum. The Ag/mica samples were cleaned by several cycles of argon ion sputtering (1000 V, 0.5  $\mu$ A) and subsequent annealing to 500°C, resulting in large defect free Ag (111) terraces with typical terrace widths over 100 nm (Figure 5.1). ACA molecules were deposited by organic molecular beam epitaxy in the preparation chambers contiguous to the measurement chambers (base pressure  $5 \times 10^{-9}$  torr). ACA in powder form (Aldrich) was placed in a quartz Knudsen cell, and degassed for at least 4 hours at 80°C to remove the water of hydration. The cell temperature was then raised to 120°C for deposition onto the room temperature Ag (111) substrates (8cm cell-substrate distance). The deposition rate was 0.3 monolayer per



minute, as calibrated from subsequent STM measurements. Here we define one monolayer (ML) of ACA coverage as one ACA molecule per 8 substrate atoms.

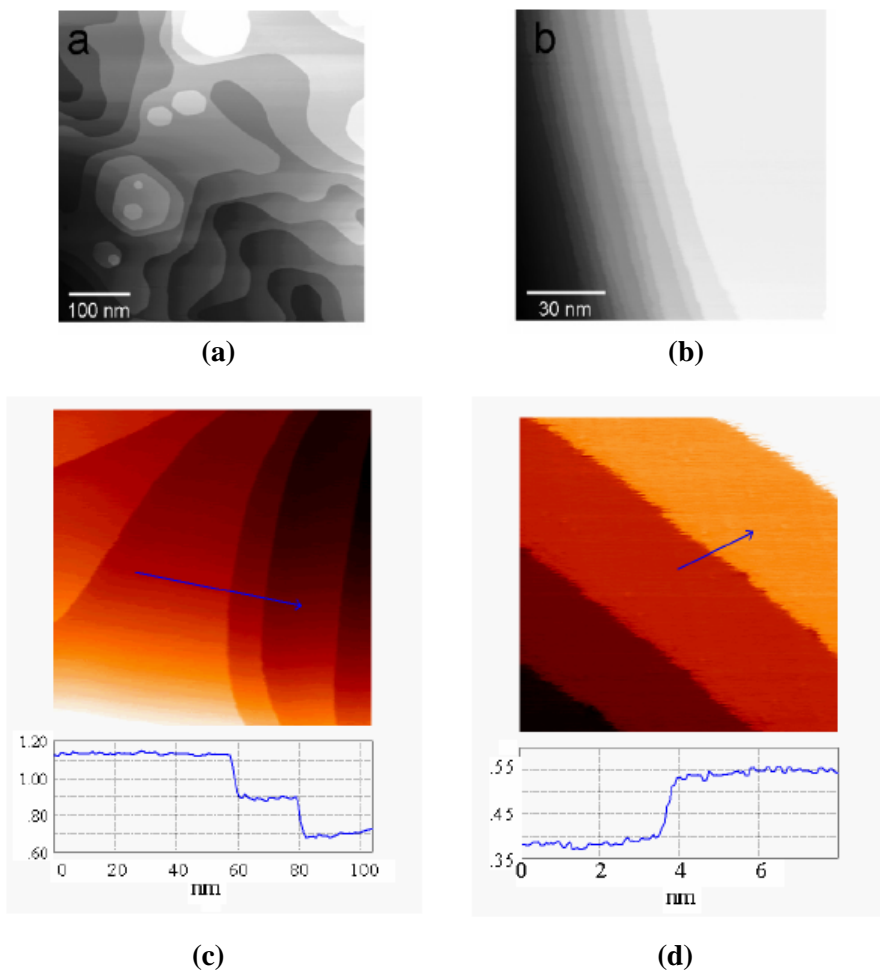


**Figure 5.1.** STM topography scans of different areas of Ag (111) after sputtering and annealing. **(a)** Relatively "smooth" surface characterized by irregular steps and silver islands are shown, whereas **(b)** "rough" surface characterized by step bunches and a wide terrace. Image **(c)** shows a magnified image of **(b)**, and **(d)** a further magnification revealing the "frizzled" crystallographic step indicative of thermal edge motion. The corresponding line profiles indicate monatomic free steps.

## 5.2.2. Scanning Tunneling Microscopy (STM)

STM experiments were performed with an Omicron UHV VT-STM system operated at room temperature with pressures typically  $5 \times 10^{-11} \text{ torr}$ . The reported images were collected in a constant current mode with a typical sample bias of +0.8 V and a typical tunneling current of 50 pA. These relatively mild tunneling conditions were chosen to minimize the tip-sample interaction. The electrochemically etched tungsten tips were cleaned under UHV by electron bombardment (200 V, 10  $\mu\text{A}$ ) immediately prior to data acquisition.

### 5.2.3. X-ray Photoelectron Spectroscopy (XPS)

XPS experiments were performed with a Kratos AXIS 165 spectrometer with a base pressure of  $3 \times 10^{-10} \text{ torr}$  using the Mg  $K_{\alpha}$  excitation line (1253.6 eV) at room temperature.

## 5.3. EXPERIMENTAL RESULTS

### 5.3.1. STM Topographies of N-Heteroaromatics

The STM images were collected with both the RT-STM and VT-STM Omnicron instruments. The deposition times were not necessarily consecutive; after scanning a sample with ACA deposition time  $t_1$ , the sample were sometimes sputtered and annealed before ACA was re-deposited with deposition time  $t_2$ . Many images were collected on both instruments, however only the VT-STM images are shown below. Shown images were collected by Dr. Bo Xu and Mr. Chengang Tao at MRSEC at University of Maryland, and they provided the ACA phase diagram as well.

#### 5.3.1.1. STM images of ACA/Ag (111)

Adlayer structures of ACA/Ag (111) were investigated as a function of coverage,  $\theta$  with room temperature STM. Kinetic effects were not measured, but rather the adlayer structures in thermal equilibrium on both low-index and vicinal surfaces. From the hundreds of STM scans collected, four phases consistently appeared: 2-D gas,  $\alpha$ -,  $\beta$ - and vicinal  $\beta$ -phase. The three phases of 2-D gas,  $\alpha$ -,  $\beta$ -phase only appeared on low-index surfaces, while the gas phase and the remaining vicinal  $\beta$ -phase only appeared on narrow step regions of vicinal surfaces.

The 2-D gas phase consist of mobile ACA. The  $\alpha$ -phase consist of head-to-tail (H-T) dimer chains, while the  $\beta$ -phase were of tail-to-tail (T-T) ordered structures densely packed. The vicinal  $\beta$ -phase, on the other hand, were of T-T dimers with dilute packing density formed in a region of high crystallographic step density. The close-packed

direction is defined along the crystallographic step direction of  $\langle 1 -1 0 \rangle$  and is one of the primitive unit cell directions used in the indexing matrix notation to describe these phases.

STM images of bare Ag (111) surface taken to survey the overall silver surface morphology, step density and possible defects. Surfaces selected for subsequent ACA deposition were atomically smooth regions, punctuated by the presence of monatomic crystallographic steps. The distribution of these crystallographic steps and islands reflect variations in the initial Ag film structure and its response to the sputter-annealing treatments. Silver film morphologies vary from surfaces with terrace widths exceeding 100 nm in combination with meandering steps and large silver islands (Figure 5.1a) to surfaces with extended (111) terraces that are bordered by large step bunches (Figure 5.1b, 5.1c). In all films of bare Ag (111), the step edges appear "frizzled" under magnification at room temperature as shown in Figure 5.1d. The room temperature motion of the Ag (111) step edge is due to the thermal exchange of silver adatoms along the step edge with kink sites.

After 2 seconds of ACA deposition, some ACA adsorb onto the step edge while others remain in the 2-D gas about the step edge (Figure 5.2a). For the isolated step edge, the ACA is seen to decorate both the upper and lower step edges indicated by the evanescent ripple and protrusions (Figure 5.2b, 5.2c).

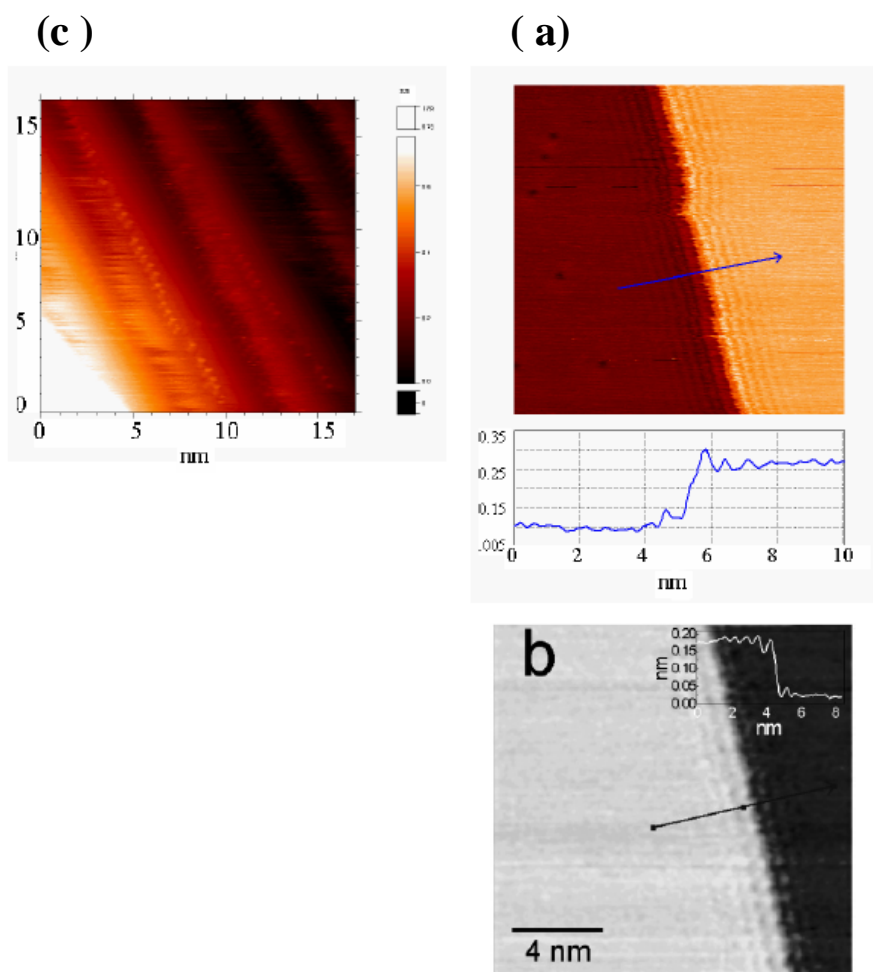


**Figure 5.2.** Early ACA chain formation along the Ag (111) step edge. (a)-(b) ACA is seen to decorate both the upper and lower step edge indicated by the evanescent ripple and protrusions. (c) Some ACA molecule adsorb onto the step edge while others remain in the 2-D gas. Line profile shows damping of the ripples.

After 30 seconds of ACA deposition, in regions of high step density, ACA form loosely packed dimer arrangements, as clearly demonstrated by the line profile (Figure 5.3), consistently showing two protrusions. These dimers further arrange in rows parallel to the step edges. In adjacent rows, dimer orientations in the surface plane alternate by  $\sim 30^\circ$  and form a zig-zag pattern. We reasonably presume these dimers to be tail-to-tail coupled

ACA dimers, generally observed in surface regions with terrace widths  $\leq 6\text{nm}$ , with appropriate coverage  $\theta$  (0.4 – 0.8 ML). The unit cell for this overlayer structure can be indexed in matrix notation as  $\begin{pmatrix} 1 & 2 \\ 2 & 6 \end{pmatrix}$ . This is the vicinal  $\beta$ -phase, also known as the 'vicinal dimer phase' (Figure 5.3).

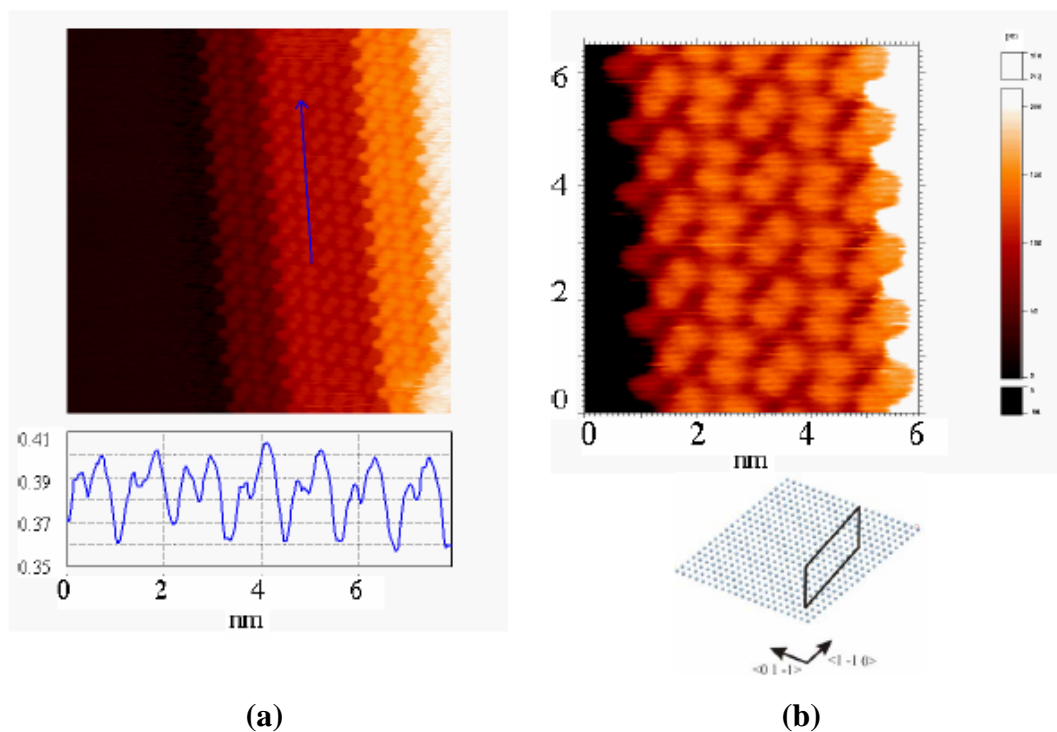


**Figure 5.3.** Vicinal  $\beta$ -phase of ACA is shown on regions with narrow Ag (111) terraces. The (a) line profile emphasizes the a dimer arrangement arranged in a zig-zag pattern, shown (b) magnified.

After 100 seconds of ACA deposition and waiting  $\sim 24$  hours before imaging, 2-dimensional arrays of ACA linear chains appear. Within each chain are individually resolved ACA that have a relative tilt with its neighbor. The unit cell for this overlayer structure are two nonequivalent ACA molecules, imaged as protrusions with different

sizes and indexed in matrix notation as  $\begin{pmatrix} 4 & 0 \\ 2 & 4 \end{pmatrix}$ . These paired nonequivalent ACA form a single dimer, modeled as two ACA with a relative tilt of  $45^\circ$  to form a head-to-tail (H-T) hydrogen bond (HB) with one another. To do so however, the two ACA cannot lie parallel to the silver surface but must rotate out-of plane. The chain comprised of these H-T dimers is a linear array of double hydrogen bonded molecules because each ACA has both an acceptor and donor at opposite ends. This is the  $\alpha$ -phase, also known as the 'chain phase' (Figure 5.4a).

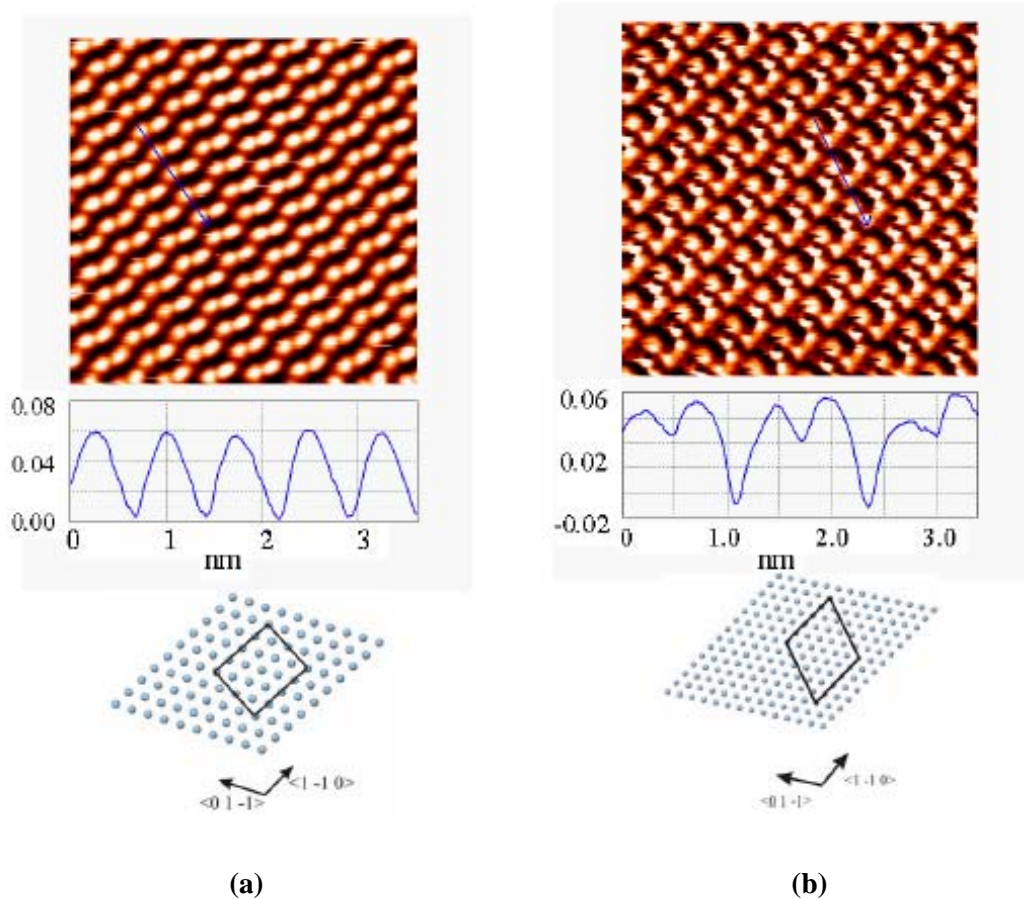


**Figure 5.4.** Large terrace areas are occupied by ordered ACA adlayers forming (a) long H-T chains in the  $\alpha$ -phase, and (b) ordered arrays of T-T dimers in the  $\beta$ -phase. The line profiles show the molecular periodicity and minimum number of protrusions per unit cell.

After 150 seconds of ACA deposition, ACA coverage ( $\theta > 0.4$  ML) is increased and large ACA islands are observed, amenable to room temperature STM imaging. In fact, STM surveys of different surface regions reveal that ACA islands generally span the large Ag (111) terraces and that the islands appear to be nucleated from the Ag step edge. The  $\sim 170$  nm x 170 nm STM image (Figure 5.5a) shows large 2-D ACA islands with diameters greater than 100 nm formed on the silver terraces at  $\theta = 0.7$  ML. A molecularly resolved STM image of this 2-D island is provided in Figure 5.5b. Such images reveal ACA molecules possess just one orientation in the 2-D island, already identified as the  $\alpha$ -phase, and arrange in rows that parallel the close-packed Ag step edge.

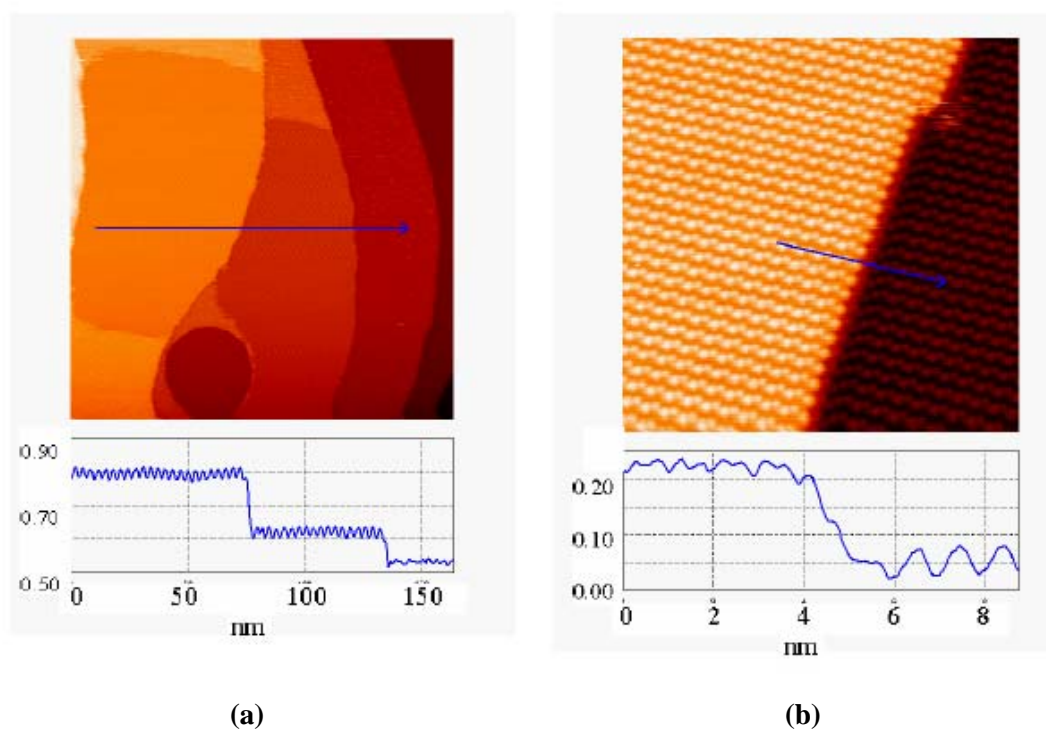


**Figure 5.5.** (a) ACA islands are formed over large terraces at coverage  $\theta = 0.7$  ML. The (b) step edge region is magnified, showing ACA molecules forming at both the upper and lower step.



After 210 seconds of ACA deposition, the procedure was slightly different. After ~ 24 hours, the surface was annealed at 0.15 Amps for 10 minutes before imaging. The unit cell consisting of two ACA dimers (or four ACA molecules) is indicated by four bright protrusions and indexed as  $(5 \ 0, 5 \ 6)$ . These four ACA molecules are modeled as a pair of dimers held together by intermolecular interactions, each dimer consists of two ACA with a relative tilt to form a tail-to-tail (T-T) hydrogen bond (HB). To accommodate the available space within the unit cell, the four ACA cannot lie parallel to the silver surface but must rotate out-of plane. This is the  $\beta$ -phase, also known as the 'ordered dimer phase' (Figure 5.4b).

The molecular orientation of ACA within the unit cell of each structural phase (except 2-D gas) is shown in Figure 5.6. The euler angles and geometrical center of the dimer pair was selected to resemble the STM image. The size of the ACA molecules are drawn to scale with the Ag (111) atom spacing.

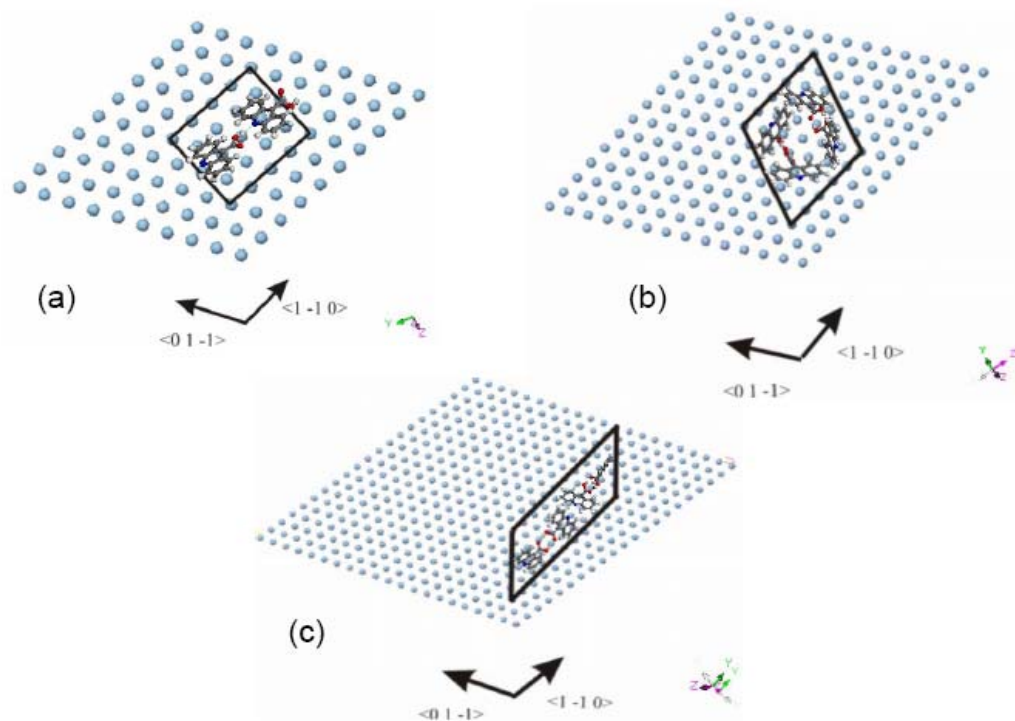


**Figure 5.6.** The unit cells of the ordered structural phases of ACA are shown. For the (a)  $\alpha$ -phase, the H-T dimer forms the unit cell, while for the (b)  $\beta$ -phase, two T-T dimers ( 4 molecules) form the unit cell. For the (c) the vicinal  $\beta$ -phase, two T-T dimers (4 molecules) form the unit cell but are less densely packed.

### 5.3.1.2. Phase Diagram of ACA/Ag (111)

The phase diagram of self-assembled ACA adlayer structure type as a function of coverage  $\theta$  was sampled for only low-index surfaces (Figure 5.7). By defining full  $\alpha$ -phase occupation as  $\theta = 1$  ML for the phase diagram, then at  $\theta < 1$  ML relative dosage times are used to estimate  $\theta$ . At  $\theta > 1$  ML, coverage  $\theta$  is determined from the projected "area" that the molecules occupied for each phase of the topographic image(s). Multiple

images were used in the statistical treatment. As noted, only two phases co-existed in the scans, i.e., 2-D gas and  $\alpha$ -phase, or  $\alpha$ - and  $\beta$ -phase.

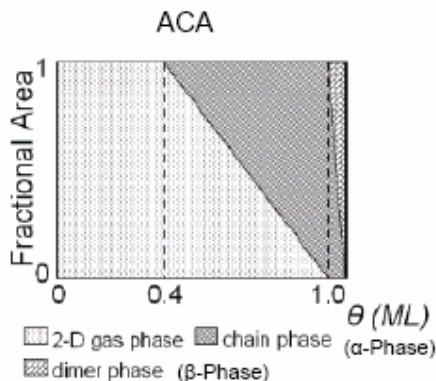


**Figure 5.7.**  
ACA phase diagram for low-index surfaces.

### 5.3.1.3. STM images of INA/Ag (111) Summary

From the numerous STM scans collected for deposited INA, only one ordered (structural) phase appeared: head-to-tail (H-T) phase. The INA formed 12 orientational domains, i.e., 6-fold rotational domains and two reflectional domains for every rotational domain. The reflection domains are prochiral enantiomers of each other. The rotational domains form a hexagonal superstructure commensurate with the Ag (111) substrate. The results are presented below (Figure 5.8) and the details can be found elsewhere[29].

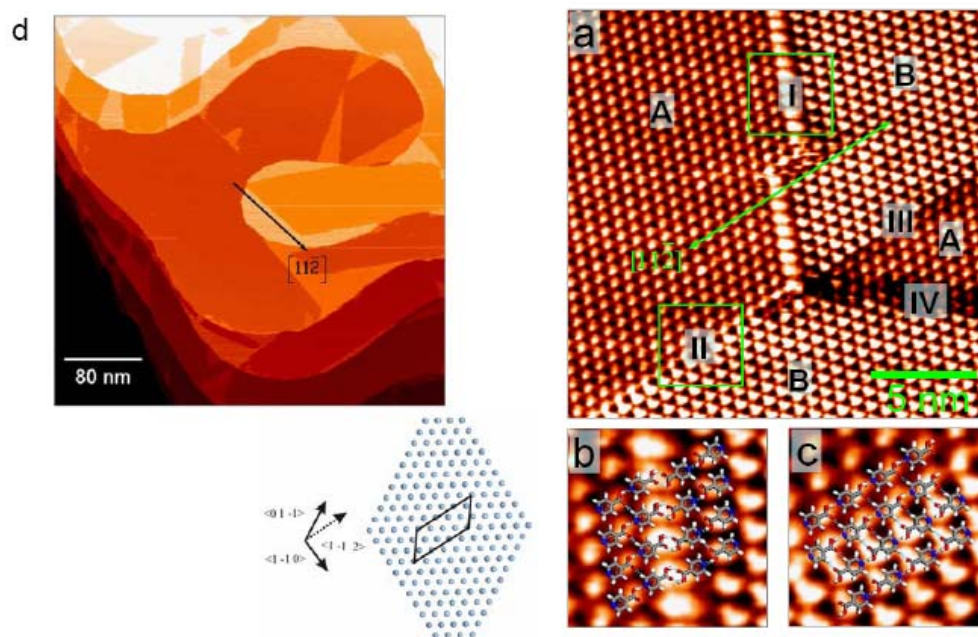


**Figure 5.8.** Ordered phase structures of INA showing that (a) 12 orientational domains form (6-fold rotational domains and two reflection domains). Magnification of (b) boxed area I, and of (c) boxed area II are shown. Over a large terrace area, the (d) rhombic shapes of INA islands form where the H-B direction is indicated by the sharp boundaries.

### 5.3.2. XPS Spectra of N-Heteroaromatics

Sample preparation for the XPS measurements was done directly in the XPS load-lock by Dr. Bo Xu for ACA and by Ms. Hui Li for INA. The XPS data was collected by Dr. Bindhu Varughese at the Chemistry & Biochemistry Department XPS facility at University of Maryland.

#### 5.3.2.1. XPS Spectra of ACA/Ag (111)

XPS measurements provide spatially averaged information on the chemical binding states of the films and serve as a further test of the proposed adlayer models. The Ag  $3d_{5/2}$  core level (not presented here) is located at 368.4 eV, before and after ACA deposition. This close agreement with the reported value for clean Ag excludes the possibility of metal-ligand formation[125]. The C 1s, O 1s and N 1s core levels spectra of the ACA film are presented in Figure 5.9.

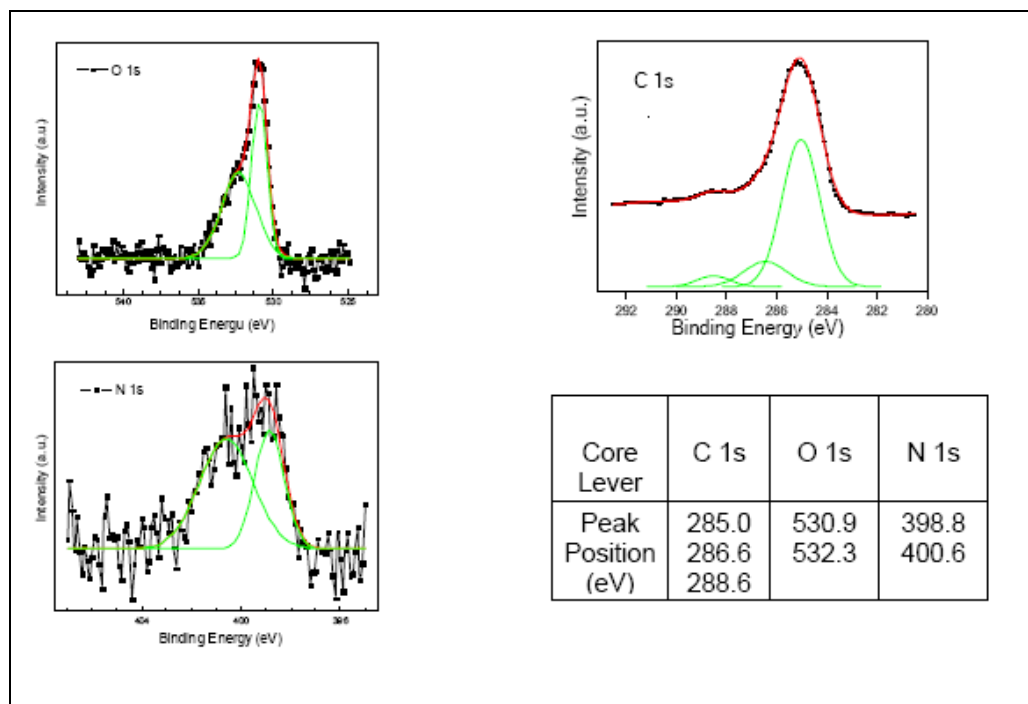


**Figure 5.9.** XPS core level shifts of ACA of atoms involved in acceptor-donor hydrogen bonding.

The C 1s core level spectrum displays one main peak centered at 285.0 eV with an asymmetric tail and shoulder towards higher binding energy. A least square fitting of the

C 1s spectrum with Gaussian functions locates three components at 285.0 eV, 286.6 eV and 288.6 eV. These components can be associated to  $C_{C=C}$ ,  $C_{C=N}$ , and  $C_{COOH}$ , respectively[126-128]. The ratios of the integrated areas of these three carbon peaks,  $C_{C=C}:C_{C=N}:C_{COOH}$ , are 5.1:1:0.42, in reasonable agreement to the expected ratios of 5.5:1:0.5 for molecular ACA.

Applying a similar fitting procedure to the O 1s spectrum reveals two features. Peaks at 530.9 eV and 532.3 eV are assigned to  $O_{C=O}$  (FWHM=1.0 eV) and  $O_{C-OH}$  (FWHM=2.1 eV), respectively. The binding energies of O 1s core level features and the difference (~1.4 eV) are in agreement with analogous aromatic molecules[129, 130]. The narrow width of the carbonyl oxygen peak suggests a uniform chemical environment. In contrast, the width of the hydroxyl oxygen peak is very wide, indicating a mixed chemical environment, and consistent with participation in H-bond formation.

The N 1s core level spectra reveals more information about H-bond formation. The N 1s spectrum reveals two peaks at 398.8 eV (FWHM = 1.2 eV) and 400.6 eV (FWHM = 2.2 eV). These two components are assigned to non-hydrogen bonding nitrogen and hydrogen bonding nitrogen, respectively[129]. From the relative areas of these features, ~70 % of the ACA molecules use N as a H-bond acceptor. The remaining 30% of adsorbed ACA molecules must form either T-T hydrogen bonds or not participate in hydrogen bond formation ( e.g., 2-D ACA gas).

### 5.3.2.2. XPS Spectra of INA/Ag (111) Summary

From the XPS data of the adlayer structures of INA/Ag (111), the results are similar to those of ACA/Ag (111). There is no core level shift of the Ag 3d<sub>5/2</sub> peak (no metal-ligand formation) and nearly same binding energies and ratio of integrated areas of N 1s as that of ACA. Thus ~ 70 % of the INA molecules use nitrogen as a hydrogen bonding acceptor. The difference is oxygen, in which case about 15 % of the oxygens are free hydroxyls at the higher binding energy (O<sub>O-H</sub> = 533.6 eV). The results are presented below (Figure 5.10) and the details can be found elsewhere[29].

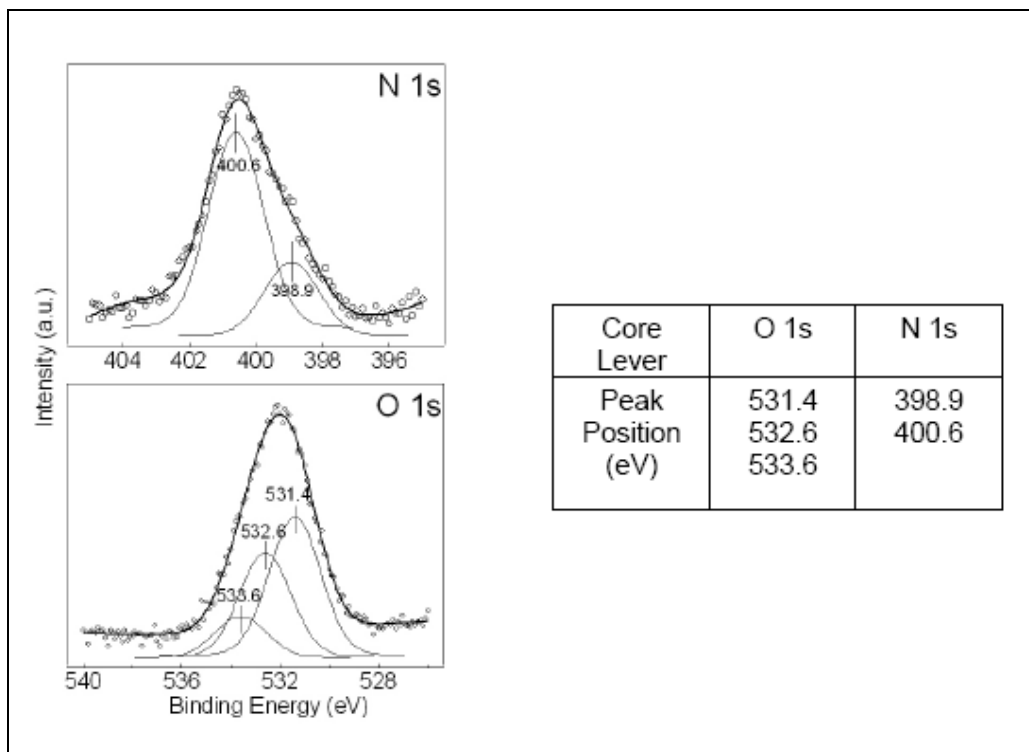


**Figure 5.10.** XPS core level shifts of INA of atoms involved in acceptor-donor hydrogen bonding.

## 5.4. COMPARISON: EXPERIMENTS VS. COMPUTATIONS

The experimental results are summarized and then compared to  $E_n$ , dimer calculations and the multipole moments analysis at large intermolecular separation.  $E_n$  represents the free energy (lowest energy where entropy is ignored) of a linear array of n-monomers governed only by intermolecular forces in a thermodynamically stable system. Another approach to understanding the dynamics of N-heteroaromatic film growth is presented. Since the kinetics of the adlayer structures have not been explored experimentally, the arguments are academic. The simplicity of its approach using distance dependent MMMA and  $\Delta E_r(n)$  and  $\Delta E_s(n)$  offers an appealing alternative to the growth mode scenario in light of the experimental results. The surface density of each ordered phase is tabulated in Table 5.1.

<b>Ordered Structural Phases</b>	<b>Molecules/unit cell</b>	<b>Ag atoms/Molecule</b>
<i>ACA <math>\alpha</math> - phase</i>	2	8
<i>ACA <math>\beta</math> - phase</i>	4	7.5
<i>ACA vicinal <math>\beta</math> - phase</i>	4	12
<i>INA <math>\alpha</math> - phase</i>	2	6

**Table 5.1.** Crystal packing arrangement of the ordered structural phases of ACA and INA determined from STM measurements are shown. The unit cell was determined from molecularly resolved STM topography images of ordered structures. For instance, for the ACA  $\alpha$  - phase, there are 2 ACA molecules per unit cell and 8 Ag atoms per ACA molecule. The later is determined from the atomic spacing of Ag (111) and the lateral dimensions of ACA.



#### 5.4.1. Experimental ACA Results Compared to its Thermodynamically Equivalent Computational Model

STM and XPS experimental results show that ACA can self-organize at thermodynamic equilibrium into possible three distinct structural phases dependent upon both its coverage and local morphology ((111) terrace width). ACA that adsorb on narrow steps can only form loosely packed T-T dimers (vicinal  $\beta$ -phase). ACA that adsorb on large terraces form large 2-dimensional islands of H-T chains ( $\alpha$ -phase). At very high coverage, ACA adsorbed on large terraces start to form large 2-dimensional islands of ordered T-T dimers ( $\beta$ -phase). From the  $E_n$  values, there is a direct correlation when it is more favorable to form H-T arrangements than it is to form T-T arrangements, namely at the crossover threshold of 3 monomers. For 'chains' formed from 3 or more monomers, the free energy  $E_n$  lowers and the cooperative effect makes it advantageous to grow long H-T type chains (Chapter 2). Only for very short chains, or dimers, are T-T type chains favorable. Thus on vicinal surfaces with low-moderate ACA coverage, only short chains can occupy or 'fit' the narrow step region, leaving dilute T-T dimer arrangements to form (vicinal  $\beta$ -phase). On large terraces at moderate-high coverage however, the H-T type chains can grow in length until they can no longer adjust their relative twist and hydrogen bond length to accommodate more ACA molecules ( $\alpha$ -phase). At even higher coverage, the H-T chain cannot survive and instead, linear rows of ordered T-T dimers form ( $\beta$ -phase). The interpretation is that it is not T-T type long chains that have formed, but rather T-T dimers that are densely packed. In that case, they form not because T-T dimers are mutually attracted to each other but because they are attracted to the substrate.

To understand the dynamics of these self-organized organic monolayers of ACA into ordered phases, the forces responsible for crystal packing are examined. Electrostatic intermolecular interactions are the major contributor to the total intermolecular energy, and thus the dominant pairwise multipole moments are the charge distributions that characterize the interactions. Thus, MMMA analysis can provide insight to the effect that separation, and consequently, coverage can have on the dynamics of these systems.

At large separation, the H-T dimer is driven by dipole-dipole interactions while the T-T dimer is driven by dipole-quadrupole and quadrupole-quadrupole interactions. This implies that for long range order, dipole-dipole interactions are responsible for the cooperative effect. On the other hand, a T-T dimer although more strongly hydrogen bonded together than a H-T dimer, are driven by quadrupole interactions and their effect are short-range.

The fact that intermolecular interactions governed by electrostatic forces predict nearly the same geometries (twist angle and hydrogen bond lengths) as shown in the dimer calculations, further supports the argument that the ACA adsorbates only weakly interact with the substrate. Furthermore, since the intermolecular energy of a single dimer is much larger than  $K_b T$ , entropy effects can be ignored and the adlayer structures are indeed stable.

#### 5.4.2. Alternative to the Growth Mode Scenario for ACA Adlayers

The energies and multipole moments of both H-T and T-T type chains of n-monomer length have been treated on equal footing. The T-T type chains have been shown to form chains held together by secondary hydrogen bonding between consecutive dimers and their interaction is governed by distinct pairwise multipole moments (Chapter 2).

Computationally, the T-T type at short chain length was the most favorable through either association or attachment. As the chains grew in length, the preference for H-T or T-T type chain depended upon the growth mode. If the chain grew through association anywhere in the chain, then the H-T type chain prevailed. On the other hand, if the chain grew via attachment, then the preferable type chain was T-T but only if it grew in pairs. The experimental results show a similar pattern.

At low coverage, individual T-T dimers were observed and occupied only the narrow step region. At moderate coverage and on large terraces, the H-T type chains grew to form compact parallel chains forming sharp edged ACA islands. At high coverage, the dominant chain type mode was T-T type chains in which the chain growth occurred through dimer-dimer interactions. This pairwise interaction parallels the requirement in the computational T-T type chain, i.e., long T-T type chain can only occur in pairs, or multiple of pairs.

When the coverage is moderate, both H-T type chains and the 2-D gas phase co-exist. In the gas phase, ACA molecules are more accessible to chain sites to associate and adsorb.

At higher coverage, there are fewer gas phase molecules available, so gas phase monomers will have less chance to approach the chain randomly. Instead, free chain ends are the most readily available for diffusing monomers. This is consistent with the phase diagram, showing the correlation of ACA type chain growth and occupation of gas phase molecules. ACA gas phase monomers can associate more readily anywhere on the chain early-on, than when the supply is less, a monomer on the silver surface can find its way to a more favorable location, with little energy cost.

Since the electrostatic intermolecular interactions are the major contributor to the total intermolecular energy, the dominant pairwise multipole moments are the charge distributions that characterize the interactions and are distance dependent. In fact, the pairwise multipole moments that dominate as a function of molecular separation can change, as in the case of ACA dimers.

At low coverage, ACA in gas phase is seen to be in equilibrium with the adsorbates that form T-T dimers. At far enough separation, these monomer partners are quadrupole (both dipole-quadrupole and quadrupole-quadrupole) driven. At moderate coverage where H-T type chains occur, the driving mechanism is dipole (dipole-dipole and dipole-octopole). Then at high coverage, where T-T dimer type chains are dominant, monomer partners are strictly quadrupole-quadrupole driven. Interestingly, the dominant driving forces can be different when the repeating units are not single molecules but dimers, as was the case for the H-T type chain. In fact, the driving forces can be very different even for very similar molecules such as INA.

### 5.4.3. Experimental INA Results and Comparison

From the STM topography images of INA, only the H-T type chains were observed. They self-assembled into rotational domain commensurate with the Ag (111) substrate. Each H-T dimer chain had a prochiral enantiomer, producing 12 possible INA chain orientational phases. Computationally, the T-T type at short chain length was the most favorable through either association or attachment but as the chains grew in length, the preference chain type was H-T. This is completely analogous to the computational results.

From the MMMA analysis, the H-T type were a mixture of dipole and quadrupole driven (dipole-octopole and quadrupole-quadrupole) electrostatic forces at small to moderate separation of its dimer partner, and dipole-dipole driven at large separation. Dipole-quadrupole interactions were strongest only at the rotational boundaries where T-T type short chains formed.

## 5.5. CONCLUSION

The distinct adlayers structures of ACA and INA molecules and their monolayer coverage are in good agreement with computational results. From MMMA arguments, the dominant multipole modes are assigned to describe the intermolecular interaction at different intermolecular separations, analogous to different surface densities (coverage). From this, it is observed that dipole and quadrupole modes drive the ACA H-T type chains which are prevalent at moderate coverages, while the quadrupole modes only drive the ACA T-T type chains prolific at even higher coverages. For the INA type chains, the results are also consistent with computational calculations. Only the H-T type chain grows throughout the terraces, driven by apparently a mixture of dipole and quadrupole modes.

## Chapter 6

### Conclusion

Anisotropic electrostatic potentials govern the crystal packing of SAMs. Computational methods that can replicate these intermolecular forces of large molecular systems are of importance in the design of SAMs and interpretation of the results of such systems. The AAAIP and MMMA methods were used to predict the hydrogen bonded arrangement of two rigid N-heteroaromatic molecules observed experimentally: 9-acridinecarboxylic acid and isonicotinic acid.

STM adlayer topographies, crystallographic diffraction data and XPS showed that both ACA and INA formed crystal packed chain structures. AAAIP and MMMA computational methods predicted chain structures that formed via physical vapor deposition on a weakly interacting surface, Ag (111). H-T and T-T type chains for ACA, and H-T type chains for INA were predicted and their interaction energy as a functional of chain length provided. Preference of one chain type over another was dependent not only upon chain length, but upon the growth mode.

By comparing *ab initio* dimer geometries to AAAIP calculation, a gauge to the AAAIP method was made. It was shown for the ACA dimer, the hydrogen bonded lengths were in

good agreement. However, for the INA case, the hydrogen bonding lengths were less satisfying. By including dispersion forces in the AAAIP and MMMA methods, the hydrogen bond lengths should improve. Nonetheless, the results were in agreement with the observed chain type.



## Appendices

## **A: Historical Efforts toward Modeling of Chains**

Computational approaches of studying chain length dependent features and formation of rigid aromatic molecules involving hydrogen bonding (HB) have a wealth of experimental data[20, 21, 30-33] to confirm and an ever-growing need for cost effective computations. In fact, the computational study of molecular chain formation and development of molecular models has flourished since inception of the statistical mechanical treatment of gases and liquids [131] motivated in part for the advancement of synthetic materials such as biomaterials, ceramics and polymer nanocomposites[132]. One of the early two-body intra-and intermolecular interaction description used for fluid systems and for soft condensed materials as well[133] was the site-site molecular fluid model. Used in conjunction with liquid state theory, thermodynamic state functions of fluids of electrolyte molecular chains[134, 135]and of flexible polymer fluids[136, 137], as well as mean molecular potentials and order parameters of lipid bilayers[138] and of polymer chains[137]were developed. Molecular fluid systems which have relied on gradients of the electrostatic potential, including as well an atomic point charge description, has been the polarizable-continuum model (PCM) used primarily to model solvent effects on solute molecules and even in gas phase[139, 140]. An anisotropic site-site model where sites are restricted to atomic nuclei positions (anisotropic atom-atom) and higher order moments of the atomic charge distribution have been have been investigated by S. L. Price, *et al.*[36, 37, 141] for fluid systems and crystal structures. A difficulty encountered has been the fact that multipole expansion of a charge distribution

extending to infinity is formally divergent at any distance from the origin of the expansion center, avoided by implementing a radius of convergence in some program applications[38].

A more rigorous treatment of the assignment of atomic charges has been Bader's atoms-in-molecules (AIM) theory designed to assign atomic charges determined from the molecular electrostatic potential (MEP)[57]. MEP is computed from the electron probability distribution determined explicitly from the appropriate electronic wavefunction and has found wide application, particularly for computing the classical Coulomb effects known to be the most influential on chemical reactivity (as opposed to quantum effects) of intra- and intermolecular interactions for numerous systems[58, 59]. Although it does rely upon an *ab initio* computation of the wavefunction, MEP is found to be not strongly affected by choice of basis set nor by inclusion of electron correlation[57].

AIM together with MEP has been used to prescribe a multipole moment description of the field due to individual atoms while maintaining the overall potential. The atomic electrostatic potential (AEP) and AIM moments have been investigated by Kosov *et al.*[38], providing a multipole moment description that lends readily to an anisotropic site-site model. This partitioning method of AEP has been successful for small size systems, in part due to the assignment of multipoles as integrations over finite volumes in the context of AIM, formally avoiding convergence problems. However, similar to the AEP approach is the anisotropic atom-atom intermolecular potential (AAAIP) computed

using A. J. Stone's ORIENT program. Widely known as distributed multipole analysis (DMA), it requires less computational effort and is probably better suited for more larger, rigid systems such as large, conjugated molecular architectures inherent in photovoltaic, LED, transistor and chemical sensors application systems.

## B: Atomic and Molecular Multipole Integers $L_t^a$ and $L_t^m$

Although  $L^a$  helps determine the local (atomic) orbit mode competition among sets of pairwise orbitals, a more definitive orbital set can be established and the energy contribution of a specific  $L^a$  can be obtained. To obtain the atomic multipole moment distribution of electrostatic and repulsive energies for a given  $L^{\text{th}}$  order integer, a new parameter  $L_t^a$  is defined whose sum, in this case, equals  $n$  and represents the summation over all atomic pairwise multiple moment integers  $(\ell_j^a, \ell_k^a)$  whose sum *only* equals 'n'. Thus,

$$L_t^a = L_{\text{max}}^a - L_{\text{max}-1}^a \quad (\text{B.1})$$

and the total atomic multipole moment integer,  $L_t^a$  shows which combination of atomic moments form the molecular cluster through electrostatic pair interactions. So for the case of  $L_t^a = 2$ , only pairs of  $\ell^{\text{th}}$  order atomic multipole moment that sum to two are included, i.e.,  $(l^1 = 1, l^2 = 1)$ ,  $(l^1 = 0, l^2 = 2)$  or  $(l^1 = 2, l^2 = 0)$ . Thus lower order modes are eliminated and are useful when considering distributions of  $L_t^a$ .

Although the total energy  $E(L^a)$  only changes  $\approx 5\%$  as  $L^a$  goes from  $3 \rightarrow 4$ , the convergence of  $E(L^a)$  does not necessarily lead to increasing attraction but oscillates near

the cut-off  $L^a$  value. More importantly,  $E(L^a)$  did not scale the same way for the different ACA conformers (Figure B.1).

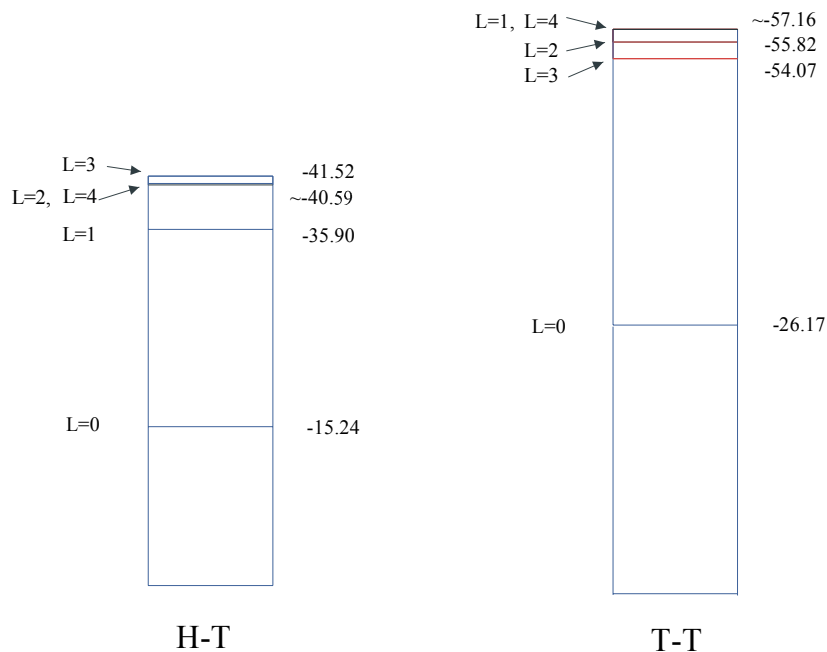


**Figure B.1.** The cumulative atomic multipole moment  $L^a$  distribution for ACA H-T and T-T conformers is displayed. The total electrostatic and repulsive energy  $E$  per cumulative multipole moment  $L^a$  (labeled  $L$ ) is the numerical value shown for both the H-T and T-T ACA dimer. For the H-T conformer,  $E(L^a = 2) \approx E(L^a = 4)$  while for the T-T conformer,  $E(L^a = 1) \approx E(L^a = 4)$ . The bar graph height grows with increasing attractive energy, showing which specific  $L^a$  values contribute to, or detract from, the change. Energies are in kJ/mol.

When considering a large number of molecules (or large molecules themselves), and thus a large number of pairwise atomic interactions, it is instructive to consider  $L_t^a$  to remove

the lower order modes . Since  $L_t^a$  is effectively the 'last' multipole moment integer of pairwise atomic multipole moments used to compute the electrostatic and repulsive energies (Eq B.1), determination of  $E(L_t^a)$  ratios provides insight to the relative importance of these higher order orbitals and which  $L_t^a$  values effect a decrease in  $E(L_t^a)$  (Table B.1).

		$E(L_t^a)$	
		H-T	T-T
$L_t^a$	0	-15.2384	-26.1735
	1	-20.6655	-30.9604
	2	-4.8521	1.3146
	3	-0.7648	1.7531
	4	0.9298	-3.0932

**Table B.1.** Electrostatic energies  $E(L_t^a)$  are tabulated for atomic multipole moment integer  $L_t^a$ . Energies in kJ/mol.

Since  $L^a$  and  $L_t^a$  always reflect the pairwise sum of the atomic moment integers, we can refer to the ‘first added-in’ contribution to a given  $L_t^a$  as the atomic monopole- $n^{\text{th}}$  multipole atomic moment interaction. For example, in the case of  $L_t^a = 2$ , the first

added-in terms are  $(l^1 = 0, l^2 = 2)$  and  $(l^1 = 2, l^2 = 0)$ . Then when considering  $L_t^a = 3$ , the first added-in terms are different but all other terms involve quadrupoles and are  $(l^1 = 1, l^2 = 2)$  and  $(l^1 = 2, l^2 = 1)$ . Thus the ratio  $E(L_t^a = 3)/E(L_t^a = 2)$  is the ratio of dipole-quadrupole interactions to dipole-dipole interactions when not considering the first added-in of  $L_t^a = 3$ . Care is taken however when ignoring the monopole interactions.

For the ACA H-T dimer, monopole-quadrupole and dipole-dipole interactions contribute only 25 % of what the monopole-dipole moment interactions alone contribute to the intermolecular dimer energy, i.e.,  $E(L_t^a = 1) \approx 4 \times E(L_t^a = 2)$ . Stated equivalently, dipole-dipole interactions are nearly four times larger than quadrupole interactions when the latter is first added-in. When quantifying the positive value of  $E(L_t^a = 4)$ , there are 3 modes that describe the interactions, i.e., hexadecapole interactions when first added-in, and quadrupole-quadrupole and dipole-octopole interactions. The sum of the 3 modes are repulsive and nearly equal in *magnitude* to the sum of octopole interactions when first added-in and to dipole-quadrupole interactions, i.e.,  $E(L_t^a = 3) \approx -E(L_t^a = 4)$  (Table B.1). Then if the repulsion is due to the quadrupole orbitals, then the octopole orbitals are relatively attractive for the H-T dimer.

When considering the cumulative pairwise addition of atomic multipole moments  $L^a$  for the H-T dimer, it's not surprising that  $E(L_t^a)$  is nearly equal for dipole-dipole type atomic interactions as for quadrupole-quadrupole type atomic interactions, i.e.,  $E(L^a = 2) \approx E(L^a = 4)$  (Figure B.1). In fact, if moment terms stopped after octopole



moments were first added-in, the attractive intermolecular energy would be even stronger, i.e.,  $L^a = 3$  and the final intermolecular energy would be  $-41.52$  kJ/mol.

Although  $\delta E(L_t^a)$  decreases as  $L^a$  increases, convergence does not establish a criteria to ignore the differences in  $E(L_t^a)$  for different  $L_t^a$  values.  $L_t^a$  represents a combination of atomic orbitals that either add to or decrease from the binding energy of the cluster.

For the ACA T-T dimer,  $L^a$  and  $L_t^a$  analysis shows a multipole distribution that leads, at least qualitatively, to some different atomic orbital competition compared to the ACA H-T dimer conformer. Like the ACA H-T dimer, monopole-dipole type atomic interactions dominate all leading multipole interactions, however much more so for these than for the H-T case, i.e.,  $E(L^a = 1)|_{T-T} > E(L^a = 1)|_{H-T}$ , by  $-21.24$  kJ/mol (Figure B.1). However, unlike the ACA H-T dimer, the quadrupole interactions when first added-in are repulsive, and only about 30 % in magnitude (Table B.1). The octopole interactions when first added-in are as well repulsive, enough to bring the T-T dimer intermolecular energy for octopole-monopole interactions up by  $\sim +3$  kJ/mol. The quadrupole-quadrupole type interactions recover the energy to what it had for monomer-monomer type interactions, i.e.,  $E(L^a = 4) \approx 4 \times E(L^a = 1)$  (Figure B.1).

Since the strength of local multipole moments generally extend over a few atoms, at most, the charge distribution of the moments are relatively small compared to charge distribution of the molecular moments, which for the case of the latter for a single monomer extends over  $\sim 10$  Angstrom region, minimally. The dominant total atomic

multipole moments are point charge-quadrupole and dipole-dipole terms, thus  $L_t^a = 2 (\ell_j^a = 0 \text{ and } \ell_k^a = 2, \text{ or } \ell_j^a = 1 \text{ and } \ell_k^a = 1)$ . Quadrupole-quadrupole terms are not the most dominant, and in fact, are least attractive for T-T dimers and repulsive for H-T dimers. The latter means that the electrostatic contribution is negligible compared to the repulsive energy term and orbital overlap between  $j, k$  atoms in the  $L^{\text{th}}$  mode is out of phase. This suggests that for short range interactions an anomaly occurs; conjugated rings often characterized by  $\pi$ - $\pi$  interaction need not be predominately quadrupole-quadrupole orbitals and can in fact be repulsive. AAAIP geometries and energies predicted are relatively correct since they correlate well to ACA dimer *ab initio* calculations, suggesting that local moments can predict the mesoscopic chain structure.

In the MMMA analogue, for all  $\ell^{\text{th}}$  order molecular multiple moment integers of the  $j^{\text{th}}$  and  $k^{\text{th}}$  molecule without regard to the  $\ell^{\text{th}}$  component  $\kappa$ , denoted  $\ell_j^m$  and  $\ell_k^m$ , the energies are computed according to their cumulative molecular multipole moment integer,  $L^m$  (Eq 2.10) and  $L_{\text{max}}^m$  (Eq 2.13).

Then for a given  $L^{\text{th}}$  order integer, parameter  $L_t^m$  is defined whose sum represents the summation over  $(\ell_j^m, \ell_k^m)$  molecular pairwise multipole moment integers. Thus,

$$L_t^m = L_{\text{max}}^m - L_{\text{max}-1}^m \quad (\text{B.2})$$

The total molecular multipole moment integer,  $L_t^m$  shows which combination of molecular moments form the monomer pair interaction.

## C: MMMA Error Analysis

Errors of the MMMA method using monomer and dimer units did not scale in similar fashion to AAAIP computations using ORIENT4.5. Although this would not be surprising given the large difference in size between monomer units consisting of chain lengths  $n=2$  and dimer units consisting of chain lengths of  $n=4$  when compared to atomic units, the results can nonetheless give insight to the larger dimerized systems. Both unit arrangements of ACA molecular chains were chosen to evaluate distribution of intermolecular energies among the different moments and to directly compare features in the short length chain regime.

The electrostatic potential of a single ACA monomer was calculated at several close and intermediate points using DFT, AAAIP and MMMA methods. To determine the accuracy of AAAIP and MMMA, relative percentage errors of AAAIP against DFT and of MMMA against AAAIP were calculated (Figure C.1). AAAIP potential errors were on the order of 1.5 % for distances  $\geq 5 \text{ \AA}$ , in excellent agreement with DFT results and continued to decrease exponentially. MMMA potential errors for a single ACA monomer, on the other hand, were on the order of 5% for distances  $\geq 20 \text{ \AA}$ , in good agreement with AAAIP results.

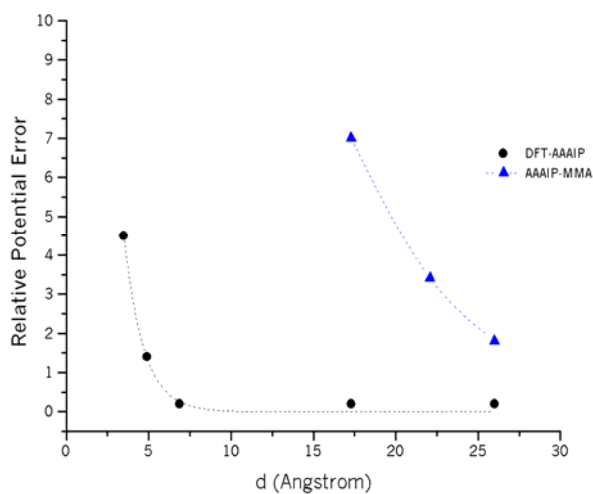


**Figure C.1.** Relative potential error of ACA monomer between DFT and AAAIP, and between AAAIP and MMMA methods.

In addition to the electrostatic potential error analysis performed, error analysis of the dimer conformers using monomer building blocks was performed as well (Figure C.2). Here, the MMMA and AAAIP electrostatic energies were computed using the dimer coordinates, Euler angles and monomer molecular moments (Table 2.3a). At 25 Å, the ACA monomer electrostatic potential is approximately 2% (Figure C.1). At roughly the same distance, the electrostatic energy error for the H-T dimer increases to 12%, while for the T-T dimer it increases to 30%. As the intermolecular separation increases, the electrostatic energy errors decrease as expected (Figure C.2). When the point charge is replaced by another ACA monomer whose global axis system is rotated by a new set of Euler angles ( $\alpha, \beta, \gamma$ ), the orientational dependence ‘S’ appears to be more sensitive to orbital alignment as well as to distance separation between local molecular axes.

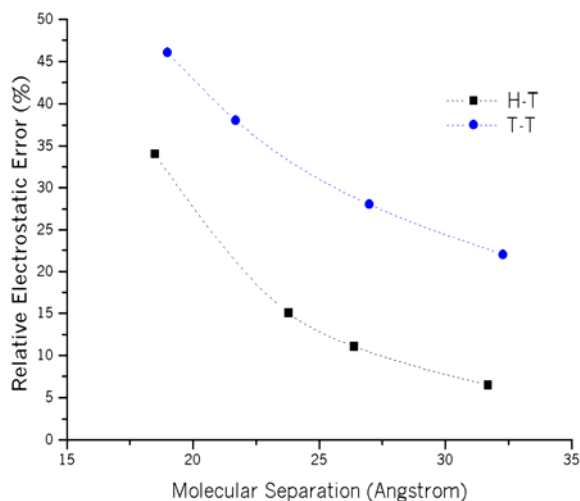


**Figure C.2.** Relative electrostatic energy error between DMA and MMMA methods of ACA HB motifs using monomer building blocks.

It is further realized that unoccupied/non-uniform modes for a particular order may also enhance the discrepancy between MMMA and AAAIP. Unoccupied modes were observed for the dipole interactions in the T-T dimer case where  $|Q_1| \approx 0$ , and for the octopole interactions where  $|Q_{3,2s}| \gg |Q_{3,\kappa}|$ . When compared to the H-T dimer, this mode imbalance did not occur. This may help explain why the T-T dimer has a much larger relative error than does the H-T dimer, constructed from the monomer building blocks.

These unoccupied or imbalanced modes can be compounded by large errors inherent in higher order moments. The introduction of higher errors at higher moments is intuitive, i.e., the charge is dispersed over larger volumes of space and require higher order differentiation of density to acquire. When lower order modes do not exist, as in the case of dipole interactions in the T-T dimer (Table 2.3b, 2.3d), the next higher order

interactions induce larger errors making  $\delta L^m |_2 \approx \delta L_t^m |_2$ . Since the electrostatic energy errors decrease as the intermolecular separation increases, the errors induced by the moments alone appear to be compensated at larger distances (Figure C.2).

The errors increase proportionally to the percentage of which a particular moment-moment interaction contributes to the total electrostatic energy, and proportionally to the relative electrostatic energy error between the AAAIP and MMMA methods (Figure C.2). This error description was imposed, assuming that the contribution per mode does not change over distance, and furthermore, that the error per mode was proportional to its percentage of total electrostatic energy.

## D: Calibration of INA Vibrational Spectra

The INA vibration spectra is calibrated here by finding a scaling factor appropriate for the molecular system and level of theory used. Since nicotinic acid (3-pyridine carboxylic acid) is a structural isomer of INA (4-pyridine carboxylic acid), nicotinic acid in the gas phase was used as the molecule of choice. By comparing the IR absorption frequency gas phase modes of nicotinic acid (NIST database) to vibrational calculations using UHF/6-31G(d) level of theory, frequency differences were optimized to produce a best-fit line. The *ab initio* calculations were already shown to produce a stable configuration of niacin; the vibrational modes, in turn, were produced from second derivatives of the energy eigenvalues, i.e., the force constant.

The computations are in good agreement with NIST gas phase IR data and a scaling factor has been derived for the IR spectra at this level of theory for this type of molecule. The scaling factor will be used in dimer vibrational modes to compare to our experimental values

Specifically, *ab initio* calculations of a stable configuration were performed with GAUSSIAN94 software program on a single processor DEC Alpha machine using UHF/6-31(d) level of theory (the details were discussed previously). From a stable atomic configuration, the energy eigenvalues and its derivatives were calculated with the same basis set about the stable configuration coordinates to determine the force constant



matrix  $f_{ij} = \frac{\partial^2 V}{\partial \xi_i \partial \xi_j}$ . The matrix is then re-diagonalized with mass weighted

coordinates, and the vibrational frequency modes  $\nu_{ij}$  computed, i.e.,

$$\nu_{ij} = \frac{1}{2\pi} \sqrt{\frac{1}{m_i m_j} \frac{\partial^2 V}{\partial \xi_i \partial \xi_j}}$$

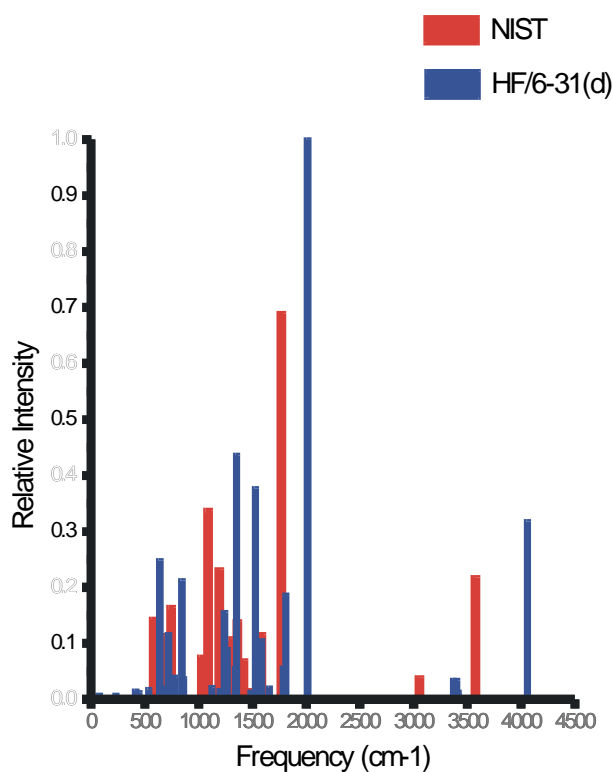


**Figure D.1.** IR frequency of relative intensities of *ab initio* (blue) and NIST (red) data for gas phase modes of niacin.

There are 36 internal modes for niacin out of which 34 were bar graph plotted along with 14 frequencies of maximum relative intensity from the NIST database (Figure D.1). Out of these frequencies, the low and high modes from both data groups were plotted against each other (Figure D.2). The high modes are well known to correlate to the carbonyl and

hydroxyl stretch, which can easily be correlated to the *ab initio* data by noting the relative coordinate change for the given mode.

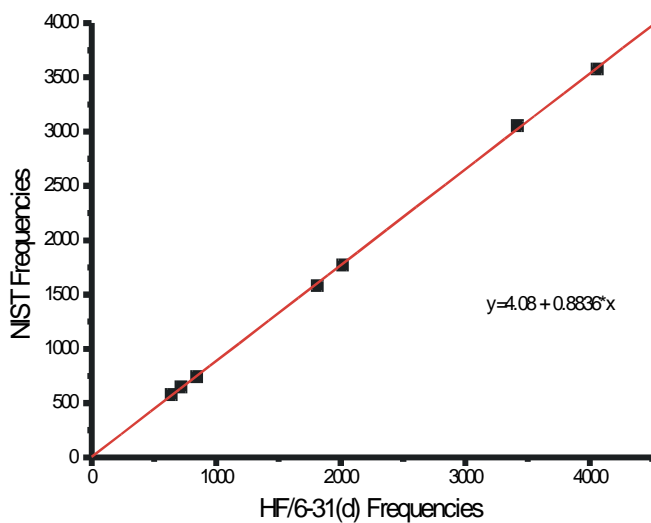


**Figure D.2.** Low and high frequencies from *ab initio* and NIST data with comparable relative intensities are plotted against each other.

Some of the vibrational frequencies for both the *ab initio* computations and NIST database were assigned modes according to well-established IR absorption range ‘finger printing’ of functional groups[142], shown respectively in Table D.1a and Table D.1b below.

IR (cm <sup>-1</sup> )	Mode Description	Predominant Mode (s)	Relative Intensity
843	+z displaced: N3, H7, H8, H9, H10, C11, H14; -z displaced: C1, C2, C4, C5, C6, O12, O13; all ring Cs, carbonyl O, hydroxyl O translate anti-symm to all ring Hs, N, carbonyl C, hydroxyl H all motion perpendicular to molecular plane.	scissor	0.213
1263	cw: C1, H10; cc: C4, H9; stretch: C1-C6, C4-C5; compress: N3-C4; all motion in molecular plane.	bending	0.090
1350	cw: C1, H10, O12; cc: C2, H9, H14; all motion in molecular plane.	bending	0.436
1527	cw: H10, C11; cc: H7, H14; carbonyl rotates anti-symm to hydroxyl rotation; all motion in molecular plane.	bending	0.377
1786	stretch: C1-C6, N3-C4; compress: C1-C2, C4-C5; all motion in molecular plane.	C=C stretch C—N stretch	0.057
1810	stretch: C5-C6, C2-N3; compress: C1 ? C4; all motion in molecular plane.	C=C stretch C—N stretch	0.187
2012	compress: C11-O12, i.e., carbonyl stretch; cc: O13, H14; hydroxyl rotation; all motion in molecular plane.	C=O stretch	1.000
4058	compress: O13, H14, i.e. hydroxyl stretch; all motion in molecular plane.	O—H stretch	0.318

**Table D.1a.** The IR normal mode frequencies for a single 3-pyridine carboxylic acid molecule was calculated using GAUSSIAN 94's UHF/6-31(d) level of theory.

IRF (cm <sup>-1</sup> )	~ Resonance Width (cm <sup>-1</sup> )	Relative Intensity	Mode Description
578	9	0.21	
650	5	0.17	C—H of alkene; bending mode.
744	13	0.24	C—H of alkene; C—H bending on ring; bending mode.
1029	9	0.11	C—O of carboxylic acid, alcohol; C—O bending/stretching mode.
1087	13	0.49	C—O of carboxylic acid, alcohol; C—O bending/stretching mode.
1190	13	0.34	C—O of carboxylic acid, alcohol; C—N of amine; C—O bending/stretching mode // C—N bending/stretching mode.
1301	18	0.16	C—O of carboxylic acid, alcohol; C—N of amine; C—O bending/stretching mode // C—N bending/stretching mode.
1359	9	0.20	C—N of amine; C—H of alkane; C—N bending/stretching mode// C—H bending/stretching mode.
1417	13	0.10	C—H of alkane; C—H bending/stretching mode.
1582	22	0.17	C=C stretching on ring ; stretching mode.
1770	8	1.00	C=O stretch of an acid anhydride; stretching mode.
3576	23	0.32	O—H stretch of monomeric alcohol, phenol; stretching mode.

**Table D.1b.** The IR frequency gas phase modes for 3-pyridine carboxylic acid (niacin) are extracted from NIST Chemistry WebBook spectrum (<http://webbook.nist.gov/chemistry>) .

From Figure D.3, we obtain a scaling factor  $\alpha = 0.8836$ . Using this scaling factor on the modes calculated for niacin from GAUSSIAN94, these are plotted with NIST database frequencies. There is an improved correlation with frequency regions, rather than the frequencies individually. This is not surprising since the experimental data are not pure stretching or bending modes, but hybrid modes where some mixing has occurred.

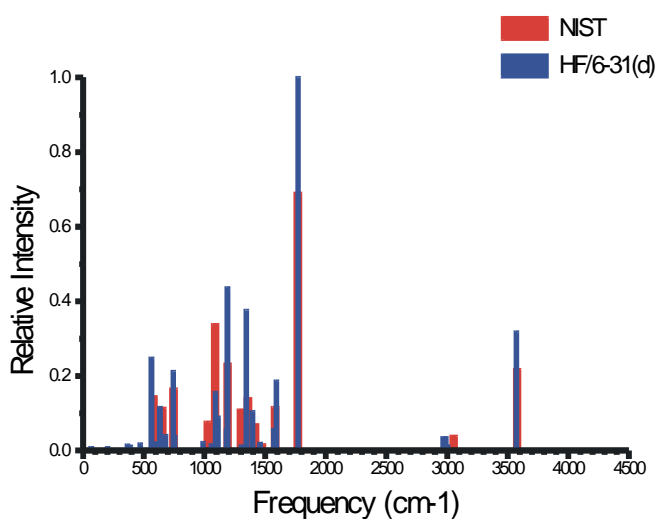


**Figure D.3.** IR frequency of relative intensities of *ab initio* (blue) (after scaling) and NIST (red) data for gas phase modes of niacin.

## E: X-ray Diffraction Details

Yellow plate-like single crystal was selected and mounted on the tip of glass. Diffraction data were collected at 233 K using SMART 1000 three-circle diffractometer (Mo  $K\alpha$  radiation, graphite monochromator) equipped with a CCD area detector[143]. 2468 frames were measured with 30 sec exposition,  $0.3^\circ$  frame width and 512 pixels frame size. Experimental details are given in APPENDIX F: Table F.1. X-ray Diffraction Data; atomic coordinates and displacement parameters have been deposited along with full list of bond lengths and angles.

The crystal structure of the 9-acridinecarboxylic dihydrate was solved by direct methods in the  $Pc$  space group. The non-centrosymmetric space group was chosen because the requisite [four molecules per unit cell] for a centrosymmetric group would yield an unreasonably high density for organic crystals. Refinement of the structure model yield  $R(F)$  of 14% in isotropic and 7% in anisotropic approximations, along with strange atomic displacement ellipsoids, a somewhat distorted geometry and uninterpretable residual Fourier peaks, revealed an inadequate model. Difference Fourier peaks from isotropic refinement showed presence of a shadow molecule superimposed on the initial molecule in such a way that all atoms except those of the carboxylic group from both orientations lie within  $0.5 \text{ \AA}$  from each other. In the following refinement, the geometry of both molecules was restrained to be similar by using the SAME instruction[144], and displacement parameters of identical atoms from both molecules were set to be identical

using the EADP instruction. Final refinement yielded  $R(F)=3.66\%$  with reasonable molecular geometry and displacement parameters. Resulting ratio of occupation factors for both molecules was refined to  $0.593(5) : 0.407(5)$ . Displacement ellipsoids of the main molecule are shown in Figure 4.1a, while superimposed molecules are depicted in Figure 4.1b.

Both superimposed molecules form a centrosymmetric pair so that the superimposed model could be described in the centrosymmetric group  $P2_1/c$ . However, in this case the ratio of occupation factors is set at 1:1, which yields higher  $R(F) = 4.2\%$ . An alternative model was tested in  $P2_1$ , another non-centrosymmetric subgroup of  $P2_1/c$ , also yielding higher  $R(F) = 4.1\%$ . Treatment of the ordered model as a merohedral twin in both non-centrosymmetric groups makes results much worse than disordered models. The latter shows that these crystals have disordered molecules within mosaic domains and not disordered orientation of ordered domains. Thus the title structure presents the case of whole-molecule disorder, which is discussed below.

## F: Table F.1. X-ray Diffraction Data

Crystal data	1220
Chemical formula	$C_{14}H_9NO_2 \cdot 2(H_2O)$
$M_r$	259.25
Cell setting, space group	Monoclinic, Pc
Temperature (K)	233 (2)
a, b, c (Å)	7.5568 (17), 16.930 (4), 4.7471 (10)
$\beta$ (°)	93.661 (4)
V (Å <sup>3</sup> )	606.1 (2)
Z	2
$D_x$ (Mg m <sup>-3</sup> )	1.421
Radiation type	Mo K $\alpha$
$\mu$ (mm <sup>-1</sup> )	0.11
Crystal form, colour	Plate, yellow
Crystal size (mm)	0.35 × 0.18 × 0.02
Data collection	
Diffractometer	Three-circle diffractometer
Data collection method	$\pi$ and $\omega$ scans
Absorption correction	Multi-scan (based on symmetry-related measurements)
$T_{\min}$	0.889
$T_{\max}$	0.998
No. of measured, independent and observed reflections	4933, 2300, 1472
Criterion for observed reflections	$I > 2\sigma(I)$
$R_{\text{int}}$	0.025
$\theta_{\max}$ (°)	27.5
Intensity decay (%)	MISSING



Refinement	
Refinement on	$F^2$
$R[F^2 > 2\sigma(F^2)], wR(F^2), S$	0.037, 0.084, 1.00
No. of reflections	2300 reflections
No. of parameters	251
H-atom treatment	Constrained to parent site
Weighting scheme	Calculated $w = 1/[\sigma^2(F_o^2) + (0.016P)^2 + 0.179P]$ , $P = (\max(F_o^2, 0) + 2F_c^2)/3$
$(\Delta/\sigma)_{\max}$	<0.0001
$\Delta\rho_{\max}, \Delta\rho_{\min}$ ( $e \text{ \AA}^{-3}$ )	0.12, -0.14
Absolute structure	(Flack, 1983)
Flack parameter	
Rogers parameter	

Computer programs: SMART (Bruker, 1999); SAINT (Bruker, 1999); SAINT; SHELXS-97 (Sheldrick, 1990); SHELXL-97 (Sheldrick, 1997); Platon (Spek, 1990); SHELXL-97.

## **G: Materials Preparation Details**

The materials preparation discussed are: chemical source preparation, silver film preparation and molecular film (deposition conditions). A significant portion of chemical source preparation is chemical purification and characterization. Silver film preparation, on the other hand, has been investigated thoroughly and a dedicated stand-alone system for its production has made it relatively easy to produce. Characterization of the organic source has been achieved using mass spectroscopy (MS) methods. This method has been very useful in obtaining the correct sublimation temperature during deposition and verifying the purity of the organic source.

ACA hydrate from Aldrich-Sigma Chemical Company is a yellow powder of needle-like crystallites. The purity of 9-acridinecarboxylic acid for the experiment involved extracting ACA from ACA hydrate without causing a chemical reaction and fragmenting ACA. This was meticulously performed by heating the sample under various conditions and cycles as the source was pumped on. MS measurements were continuously made while temperature points and partial pressures were recorded.

By loading the powder into a custom pyrex tube that mounted to the vacuum chamber through VCR hardware, the ACA powder was directly observed. The pyrex tube itself was placed in an external oil bath and heated to a set temperature for each particular run. The MS values were confirmed through the Mass Spectrometer facility by Noel

Whittaker. The nominal temperature for ACA was 120 C° to both drive off the water without fragmenting the compound, and for sublimation.

For the Ag (111) film preparation, high quality films were routine. Ag (111)/mica were silver films grown epitaxially by vapor deposition on grade V4 Muscovite mica in a dedicated stand-alone system in MRSEC. Through trial runs performed specific to the stand-alone system, MRSEC developed a procedure to producing high quality Ag (111)/mica film. The films were generally 300-400 nm thick with large defect free terraces.

Once the silver films were produced, they were spot welded onto a UHV/STM sample holder. The Ag/mica samples were then cleaned by several cycles of argon ion sputtering (1000 V, 0.5  $\mu$ A) and subsequent annealing to 500°C in-situ. Using Low Energy Electron Diffraction (LEED) and Auger Electron Spectroscopy (AES), the Ag (111) films were quality checked to be later used as silver substrates for molecular films. Fast cooling cycles during the annealing process was considered to decrease the amount of step bunching by as much as 10%.

Numerous source deposition systems were attempted. However, the one chosen was the least expensive. A homemade, Knudson-type source delivery system was made and installed on the load-lock for ACA deposition onto Ag (111) through sublimation. After outgassing the ACA through conductive heating (in-situ) at T=120 C°, molecular ACA films were readily prepared with relative ease. This produced a deposition at a rate of 0.3

monolayer/min where one monolayer (ML) of ACA coverage is equivalent to one ACA per 8 Ag substrate atoms.

## H: Descriptive Overview of STM and XPS

Scanning tunneling microscopy (STM) and x-ray photoelectron spectroscopy (XPS) measurements are two of the state-of-the-art UHV instruments used to characterize our N-heteroaromatic adlayer structures on Ag (111). The silver film support is a pristine 2-D surface on which the organic molecules can land and then diffuse to their final destination. To image molecules with  $\sim 0.5 \text{ \AA}$  resolution using STM, requires prudent tip preparation and quality molecular films. The latter required by XPS as well. The high quality molecular film preparation of 9-acridinecarboxylic acid on Ag (111) requires chemical purification, silver film preparation and characterization. XPS as well requires quality molecular films.

Using STM, a negative bias voltage is applied to the scanning tip and tunneling current flows from the tip to the local molecule, then to the silver substrate to complete the circuit. Now the LUMO state is accessible for electrons to (partially) occupy and the STM image reflects a density of states, sensitive to the flux of electrons from the tip (Figure H.1).

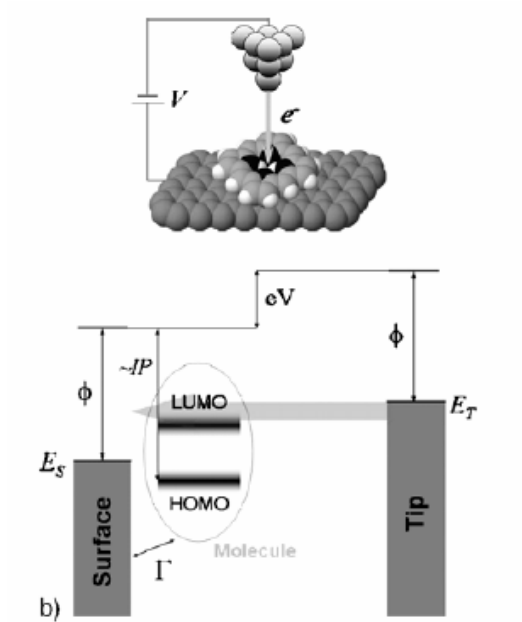


**Figure H.1.**  
Electron tunnel from the negatively biased tip to the molecule on the surface.

Tip height position is a measure of the probability that electrons tunnel through to the LUMO state, and is expressed as,

$$I \approx \frac{4\pi e}{\hbar} |M_T|^2 \rho_t(\varepsilon) \int_{eV}^0 \rho_s(\varepsilon) d\varepsilon \quad (\text{H.1})$$

or,

$$I \approx e^{-\sqrt{\kappa z}} \quad (\text{H.2})$$

where I is the tunneling current and distance z is the distance between the tip (electrode) and the molecule. When the STM controller is set to constant current mode, the height z is adjusted to bring the tunneling current back to the set point current  $I_0$ . Thus the bright

(dark) lobes mean the particle is far away from (very near) the surface. This is analogous to their being a large (small) tunneling current before the set-point current  $I_0$  kicks in.

XPS, on the other hand, relies on the photoelectric effect. From XPS measurements, the identification of particular atoms (or functional groups) and their oxidation states can be identified by the bindings energies assigned to atomic elements (or functional groups) and their binding energy shifts, respectively. Through intensity integration over the binding energies of a core electron of an atom, a compositional analysis of the surface can be made and the percentage of the chemical binding states of that particular atom can be found.

$$h\nu = E_{BE} + E_{KE} + E_{WF} \quad (\text{H.3})$$

where  $E_{BE}$  is the binding energy of the core electron,  $E_{KE}$  is the kinetic energy of the ejected core electron and  $E_{WF}$  is the work function of the spectrometer[145].

## Bibliography

1. Aviram, A. and M.A. Ratner, *Molecular rectifiers*. Chemical Physics Letters, 1974. **29**(2): p. 277-283.
2. Metzger, R.M., et al., *Unimolecular electrical rectification in hexadecylquinolinium tricyanoquinodimethanide*. Journal of the American Chemical Society, 1997. **119**(43): p. 10455-10466.
3. Hung, L.S., C.W. Tang, and M.G. Mason, *Enhanced electron injection in organic electroluminescence devices using an Al/LiF electrode*. Applied Physics Letters, 1997. **70**(2): p. 152-154.
4. Jabbour, G.E., et al., *Highly efficient and bright organic electroluminescent devices with an aluminum cathode*. Applied Physics Letters, 1997. **71**(13): p. 1762-1764.
5. Collier, C.P., et al., *Electronically configurable molecular-based logic gates*. Science, 1999. **285**: p. 391-394.
6. Bumm, L.A., et al., *Are single molecular wires conducting?* Science, 1996. **271**: p. 1705-1707.
7. Malinsky, J.E., et al., *Self-assembly processes for organic LED electrode passivation and charge injection balance*. Advanced Materials, 1999. **11**(3): p. 227-231.



8. Walzer, K. and M. Hietschold, *STM and STS investigation of ultrathin tin phthalocyanine layers adsorbed on HOPG(0001) and Au(111)*. Surface Science, 2001. **471**: p. 1-10.
9. Hanessian, S., et al., *Molecular recognition and self-assembly by "weak" hydrogen bonding: unprecedented supramolecular helicate structures from diamine/diol motifs*. Journal of the American Chemical Society, 1994. **116**: p. 4495-4496.
10. Seto, C.T. and G.M. Whitesides, *Molecular self-assembly through hydrogen bonding: supramolecular aggregates based on the cyanuric acid-melamine lattice*. Journal of the American Chemical Society, 1993. **115**: p. 905-916.
11. Ray, P.C. and P.K. Das, *Probing molecular self-assembly by hyper-Rayleigh scattering in solution*. Chemical Physics Letters, 1997. **281**: p. 243-246.
12. Zerkowski, J.A., et al., *Design of organic structures in the solid state: hydrogen-bonded molecular "tapes"*. Journal of the American Chemical Society, 1990. **112**: p. 9025-9026.
13. Furukawa, M., H. Tanaka, and T. Kawai, *Formation mechanism of low-dimensional superstructure of adenine molecules and its control by chemical modification: a low-temperature scanning tunneling microscopy study*. Surface Science, 2000. **445**: p. 1-10.
14. Marti, E.M., et al., *Bonding and assembly of the chiral amino acid S-proline on Cu(110): the influence of structural rigidity*. Surface Science, 2002. **501**: p. 191-202.

15. Kuhnle, A., et al., *Chiral recognition in dimerization of adsorbed cysteine observed by scanning tunneling microscopy*. *Nature*, 2002. **415**: p. 891-893.
16. Kumar, A., H.A. Biebuyck, and G.M. Whitesides, *Patterning self-assembled monolayers: applications in materials science*. *Langmuir*, 1994. **10**: p. 1498-1511.
17. Aizenberg, J., A.J. Black, and G.M. Whitesides, *Control of crystal nucleation by patterned self-assembled monolayers*. *Nature*, 1999. **398**: p. 495-498.
18. Pereira, R.V., A.P.G. Ferreira, and M.H. Gehlen, *Excited-State Intramolecular Charge Transfer in 9-Aminoacridine Derivative*. *Journal of Physical Chemistry A*, 2005. **109**: p. 5978-5983.
19. Kuruvilla, E., J. Joseph, and D. Ramaiah, *Novel Bifunctional Acridine-Acrinium Conjugates: Synthesis and Study of Their Chromophore-Selective Electron-Transfer and DNA-Binding Properties*. *Journal of Physical Chemistry B*, 2005. **109**: p. 21997-22002.
20. Xu, B., et al., *Chiral Symmetry Breaking in Two-Dimensional C<sub>60</sub>-ACA Intermixed Systems*. *Nano Letters*, 2005. **5**(11): p. 2207-2211.
21. Xu, B., et al., *Coverage Dependent Supramolecular Structures: C<sub>60</sub>: ACA Monolayers on Ag(111)*. *Journal of the American Chemical Society*, 2006. **128**(26): p. 8493-8499.
22. Crenshaw, J.M., D.E. Graves, and W.A. Denny, *Interaction of Acridine Antitumor Agents with DNA: Binding Energies and Groove Preferences*. *Biochemistry*, 1995. **34**(41): p. 13682-13687.

23. Stanslas, J., et al., *Antitumor Polycyclic Acridines. 7.<sup>1</sup> Synthesis and Biological Properties of DNA Affinic Tetra- and Pentacyclic Acridines*. Journal of Medicinal Chemistry, 2000. **43**: p. 1563-1572.
24. Negron-Encarnacion, I., R. Arce, and M. Jimenez, *Characterization of Acridine Species Adsorbed on (NH<sub>4</sub>)<sub>2</sub>SO<sub>4</sub>, SiO<sub>2</sub>, Al<sub>2</sub>O<sub>3</sub>, and MgO by Steady-State and Time-Resolved Fluorescence and Diffuse Reflectance Techniques*. Journal of Physical Chemistry A, 2005. **109**: p. 787-797.
25. Shukla, R., M. Mishra, and S.N. Tiwari, *Study of acridine-DNA biopolymer interactions*. Progress in Crystal Growth and Characterization of Materials, 2006. **52**: p. 107-113.
26. Avouris, P. and J.E. Demuth, *Electronic excitations of benzene, pyridine, and pyrazine adsorbed on Ag(111)*. Journal of Chemical Physics, 1981. **75**(10): p. 4783-4794.
27. Demuth, J.E., K. Christmann, and P.N. Sanda, *The vibrations and structure of pyridine chemisorbed on Ag(111); the occurrence of a compressional phase transformation*. Chemical Physics Letters, 1980. **76**(2): p. 201-206.
28. O'Shea, J.N., et al., *Hydrogen-bond induced surface core-level shift in pyridine carboxylic acids*. Surface Science, 2001. **486**: p. 157-166.
29. Li, H., *N-Heteroaromatic Acid Adlayer Structures Under Hydrogen Bonding Influence: A Comprehensive UHV-STM/XPS/RAIRS Study*, in *Chemistry & Biochemistry*. 2006, University of Maryland: College Park, MD.
30. Xu, B., et al., *Morphology Selected Molecular Architecture: Acridine Carboxylic Acid Monolayers on Ag (111)*. Journal of Physical Chemistry B, 2006. **110**(3):

- p. 1271-1276.
31. Keeling, D.L., et al., *Assembly and Processing of Hydrogen Bond Induced Supramolecular Nanostructures*. Nano Letters, 2003. **3**(1): p. 9-12.
  32. Prins, L.J., et al., *An Enantiomerically pure hydrogen-bonded assembly*. Nature, 2000. **408**: p. 181.
  33. Yokoyama, T., S. Yokoyama, and T. Kamikado, *Selective assembly on a surface of supramolecular aggregates with controlled size and shape*. Nature, 2001. **413**: p. 619-621.
  34. Vinogradov, S.N. and R.H. Linnell, *Hydrogen Bonding*. 1971, New York: Van Nostrand Reinhold Company.
  35. White, H.E., *Pictorial Representations of the Electron Cloud for Hydrogen-Like Atoms*. Physical Review, 1931. **37**: p. 1416-1424.
  36. Nobeli, I. and S.L. Price, *A non-empirical intermolecular potential for oxalic acid crystal structures*. Journal of Physical Chemistry A, 1999. **103**(32): p. 6448.
  37. van Mourik, T., S.L. Price, and D.C. Clary, *Diffusion Monte Carlo simulations on uracil-water using an anisotropic atom-atom potential model*. Faraday Discussions, 2001. **2001**(118): p. 95.
  38. Kosov, D.S. and P.L.A. Popelier, *Convergence of the multipole expansion for electrostatic potentials of finite topological atoms*. Journal of Chemical Physics, 2000. **113**(10): p. 3969.
  39. Bindu, V., K. Smitha, and T. Pradeep, *Tilted orientation of molecular chains at the surface of a series of perfluoropolyether liquids: an X-ray photoelectron spectroscopic investigation*. Molecular Physics, 1998. **93**(1): p. 85.

40. Cardini, G., P. Baglioni, and G. Taddei, *Crystalline structures of condensed films at liquid interfaces*. Chemical Physics Letters, 1982. **93**(6): p. 533.
41. Baglioni, P., G. Cardini, and G. Gabrielli, *Hydrogen-bonded two-dimensional molecular crystals at liquid interfaces*. Journal of Physical Chemistry, 1982. **86**(24): p. 4684.
42. Smith, L.A., et al., *Crystallisation of sodium dodecyl sulphate from aqueous solution: phase identification, crystal morphology, surface chemistry and kinetic interface roughening*. Journal of Crystal Growth, 2004. **263**: p. 480.
43. Hudson, B.S., D.A. Braden, and D.G. Allis, *The Crystalline Enol of 1,3-Cyclohexanedione and Its Complex with Benzene: Vibrational Spectra, Simulation of Structure and Dynamics and Evidence for Cooperative Hydrogen Bonding*. Journal of Physical Chemistry A, 2004. **108**(36): p. 7356.
44. Kishimoto, N., et al., *Probing the Shape and Stereochemistry of Molecular Orbitals in Locally Flexible Aromatic Chains: A Penning Ionization Electron Spectroscopy and Green's Function Study of the Electronic Structure of Biphenyl*. Journal of Physical Chemistry A, 2005. **2005**(109): p. 10535.
45. Phillips, J.M. and M.D. Hammerbacher, *Methane adsorbed on graphite. I. Intermolecular potentials and lattice sums*. Physical Review B (Condensed Matter and Materials Physics), 1984. **29**(10): p. 5859.
46. Wurger, A., *Molecular Ordering in Amphiphile Monolayers and Alkanes*. Physical Review Letters, 1999. **83**(23): p. 4816.

47. Boeyens, J.C.A. and D.C. Levendis, *Rotational disorder in crystalline pyrene as a model for layered aromatic structures*. Journal of Chemical Physics, 1985. **83**(5): p. 2368.
48. Rowley, R.L., Y. Yang, and T.A. Pakkanen, *Determination of an ethane intermolecular potential model for use in molecular simulations from ab initio calculations*. Journal of Chemical Physics, 2001. **114**(14): p. 6058.
49. Roszak, S., et al., *New theoretical insight into the interactions and properties of formic acid: Development of a quantum-based pair potential for formic acid*. Journal of Chemical Physics, 2005. **123**: p. 144702.
50. Klymenko, V.E. and V.M. Rozenbaum, *Orientations of linear nonpolar molecules in a regular chain*. Journal of Chemical Physics, 1999. **110**(12): p. 5978.
51. Suhai, S., *Cooperative effects in hydrogen bonding: Fourth-order many-body perturbation theory studies of water oligomers and of an infinite water chain as a model for ice*. Journal of Chemical Physics, 1994. **101**(11): p. 9766.
52. Liu, J.-X. and J.J. Elliott, *Screening Effects on Hydrogen Bonding in Chain Molecular Fluids: Thermodynamics and Kinetics*. Industrial & Engineering Chemistry Research, 1996. **1996**(35): p. 2369.
53. Cerda, J., et al., *Novel Water Overlayer Growth on Pd (111) Characterized with Scanning Tunneling Microscopy and Density Functional Theory*. Physical Review Letters, 2004. **93**(11): p. 116101.

54. Banaszak, B.J., R. Faller, and J.J. de Pablo, *Simulation of the effects of chain architecture on the sorption of ethylene in polyethylene*. Journal of Chemical Physics, 2004. **120**(23): p. 11304.
55. Pint, C.L., *Different melting behavior in pentane and heptane monolayers on graphite: molecular dynamics*. Physical Review B (Condensed Matter and Materials Physics), 2006. **73**(4): p. 45415.
56. Gay, J.G. and B.J. Berne, *Modification of the overlap potential to mimic a linear site-site potential*. Journal of Chemical Physics, 1981. **74**(6): p. 3316.
57. Levine, I.N., *Quantum Chemistry*. 2000, Upper Saddle River: Prentice-Hall, Inc.
58. Sagui, C., L.G. Pedersen, and T.A. Darden, *Towards an accurate representation of electrostatics in classical force fields: Efficient implementation of multipolar interactions in biomolecular simulations*. Journal of Chemical Physics, 2004. **120**(1): p. 73.
59. Cubero, E., F.J. Luque, and M. Orozco, *Is polarization important in cation-pi interactions ?* PNAS, 1998. **95**: p. 5976.
60. Harrison, J.F., *Local moments from a Hirshfeld partitioning of the electron density: comparison to DMA for N<sub>2</sub>, O<sub>2</sub> and F<sub>2</sub>*. Molecular Physics, 2005. **103**(6): p. 1099.
61. Stone, A.J., Y. Tantirungrotechai, and A.D. Buckingham, *The dielectric virial coefficient and model intermolecular potentials*. Physical Chemical Chemical Physics, 1999. **2000**(2): p. 429.

62. Hodges, M.P., A.J. Stone, and E.C. Lago, *Analytical Potentials for HF Dimer and Larger HF Clusters from ab Initio Calculations*. Journal of Physical Chemistry A, 1998. **102**: p. 2455.
63. Hodges, M.P. and A.J. Stone, *A new representation of the dispersion interaction*. Molecular Physics, 2000. **98**(5): p. 275.
64. Using the AAAIP analysis, Stone et al. showed that for the water dimer the electrostatic energy contribution was ~ 40 % of the total energy of absolute sums, while the repulsion energy contribution was ~ 33 %. The remaining energy was distributed between dispersion, induction and charge transfer[Stone, 1996].
65. Kaplan, I.G., *Intermolecular Interactions: Physical Picture, Computational Methods and Model Potentials*. 2006, West Sussex: John Wiley & Sons.
66. Stone, A.J., *The Theory of Intermolecular Forces*. 1996, New York: Oxford University Press.
67. Wheatley, R.J. and J.B.O. Mitchell, *Gaussian multipoles in practice: Electrostatic energies for intermolecular potentials*. Journal of Computational Chemistry, 1994. **15**(11): p. 1187.
68. Saitow, K., et al., *Attractive and Repulsive Intermolecular Interactions of a Polar Molecule: Short-Range Structure of Neat Supercritical CHF<sub>3</sub> Investigated by Raman Spectroscopy*. Journal of Physical Chemistry A, 2004. **2004**(108): p. 5770.
69. Cabaleiro-Lago, E.M. and M.A. Rios, *Potential functions for describing intermolecular interactions in cyanoacetylene clusters*. Journal of Chemical Physics, 1998. **109**(19): p. 8398.



70. Soderhjelm, P., G. Karlstrom, and U. Ryde, *Comparison of overlap-based models for approximating the exchange-repulsion energy*. Journal of Chemical Physics, 2006. **124**: p. 244101.
71. Wales, D.J., A.J. Stone, and P.L.A. Popelier, *Potential energy surfaces of several van der Waals complexes modelled using distributed multipoles*. Chemical Physics Letters, 1995. **1995**(240): p. 89-96.
72. Spomer, J., J. Leszczynski, and P. Hobza, *Base stacking in Cytosine Dimer. A Comparison of Correlated Ab Initio Calculations with Three Empirical Potential Models and Density Models and Density Functional Theory Calculations*. Journal of Computational Chemistry, 1996. **17**(7): p. 841-850.
73. Harris, D.C. and M.D. Bertolucci, *Symmetry and Spectroscopy: An Introduction to Vibrational and Electronic Spectroscopy*. 1989, New York: Dover Publications, Inc.
74. Cioslowski, J., *General and Unique Partitioning of Molecular Electronic Properties into Atomic Contributions*. Physical Review Letters, 1989. **62**(13): p. 1469-1471.
75. Jones, H.W., *Exact formulas for multipole moments using Slater-type molecular orbitals*. Physical Review A (General Physics), 1986. **33**(3): p. 2081-2083.
76. Almlöf, J. and P.R. Taylor, *General contraction of Gaussian basis sets. II. Atomic natural orbitals and the calculation of atomic and molecular properties*. Journal of Chemical Physics, 1990. **92**(1): p. 551-560.
77. Jug, K., *Charge distributions and multipole moments in molecules*. Theoretica Chimica Acta, 1975. **39**(4): p. 301-312.

78. Alberts, I.L., *Theoretical organic chemistry*. Annual Reports on the Progress of Chemistry, Section B, 2000. **96**: p. 477-495.
79. Meier, R.J., *Are current DFT methods sufficiently reliable for real-world molecular systems ?* Faraday Discussion, 2003. **124**: p. 405-412.
80. Kaczmarek, A. and A. Sadlej, *Monomer basis-set truncation effects in calculations of interaction energies: A model study*. Journal of Chemical Physics, 2004. **120**(17): p. 7837-7848.
81. Morozov, A., K. Tsemekhman, and D. Baker, *Electron Density Redistribution Accounts for Half the Cooperativity of Alpha Helix Formation*. Journal of Physical Chemistry B, 2006. **2006**(110): p. 4503-4505.
82. Mei, X. and C. Wolf, *Neutral and Ionic Supramolecular Structures of Unsaturated Dicarboxylic Acids and Acridine: Significance of Molecular Geometry and Proton Transfer*. European Journal of Organic Chemistry, 2004. **2004**(21): p. 4340-4337.
83. Rovira, C. and J.J. Novoa, *A density functional study of crystalline acetic acid and its proton transfer polymorphic forms*. Journal of Chemical Physics, 2000. **113**(20): p. 9208.
84. Abe, Y. and K. Tashiro, *Computer Simulation of Structure and Ferroelectric Phase Transition of Vinylidene Fluoride Copolymers. IV. The Factors Governing the Ferroelectric Phase Transition of VDF-TrFE Copolymers*. Journal of Polymer Science, 2000. **39**: p. 689.

85. Asfin, R.E., et al., *Particular Features of the  $\nu(\text{OH})$  Absorption Band of Strongly Hydrogen-Bonded Complexes in the Gas Phase, Low-Temperature Matrices, and Crystalline Films at 12-600 K*. *Optics and Spectroscopy*, 2005. **99**: p. 56.
86. Jensen, F., *Introduction to Computational Chemistry*. 2001, New York: John Wiley & Sons.
87. -18.60 kJ/mol for the T-T conformer and -10.82 kJ/mol for the H-T conformer.
88. Del Bene, J.E. and M.J.T. Jordan, *Vibrational spectroscopy of the hydrogen bond: an ab initio quantum-chemical perspective*. *International Reviews in Physical Chemistry*, 1999. **18**(1): p. 119-162.
89. Tsuzuki, S., et al., *Effects of basis set and electron correlation on the calculated interaction energies of hydrogen bonding complexes: MP2/cc-pV5Z calculations of H/sub 2/O-MeOH, H/sub 2/O-Me/sub 2/O, H/sub 2/O-H/sub 2/O, MeOH-MeOH, and HCCOH-HCOOH complexes*. *Journal of Chemical Physics*, 1999. **110**(24): p. 11906-11910.
90. Sinnokrot, M.O., E.F. Valeev, and C.D. Sherrill, *Estimates of the Ab Initio Limit for pi-pi Interactions: The Benzene Dimer*. *Journal of the American Chemical Society*, 2002. **124**(36): p. 10887-10893.
91. Rashkin, M.J. and M.L. Waters, *Unexpected Substituent Effects in Offset pi-pi Stacked Interactions in Water*. *Journal of the American Chemical Society*, 2002. **124**(9): p. 1860-1861.
92. Bevitt, J., et al., *An ab initio Study of Anharmonicity and Field Effects in Hydrogen -Bonded Complexes of the Deuterated Analogues of HCL and HBr with*

- NH3 and N(CH3)3*. Journal of Physical Chemistry A, 2001. **105**(13): p. 3371-3378.
93. Head-Gordon, M., *Quantum Chemistry and Molecular Processes*. Journal of Physical Chemistry, 1996. **100**: p. 13213-13225.
94. Frisch, M.J.; Trucks, G. W.; Schlegel, H. B.; Scuseria, G. E.; Robb, M. A.; Cheeseman, J. R.; Montgomery, J. A.; Vreven, T.; Kudin, K.; Burant, K. N.; Burant, J. C.; Milliam, J. M.; Iyengar, S. S.; Tomasi, J.; Barone, V.; Mennucci, B.; Cossi, M.; Scalmani, G.; Rega, N.; Petersson, G. A.; Nakatsuji, H.; Hada, M.; Ehara, M.; Toyota, K.; Fukuda, R.; Hasegawa, J.; Ishida, M.; Nakajima, T.; Honda, Y.; Kitao, O.; Nakai, H.; Klene, M.; Li, X.; Knox, J. E.; Hratchian, J. P.; Cross, J. B.; Adamo, C.; Jaramillo, J.; Gomperts, R.; Stratmann, R. E.; Yazyev, O.; Austin, A. J.; Cammi, R.; Pomelli, C.; Ochterski, J. W.; Ayala, P. Y.; Moroduma, K.; Voth, G. A.; Salvador, P.; Dannenberg, J. J.; Zakrzewski, V. G.; Dapprich, S.; Daniels, A. D.; Strain, M. C.; Farkas, O.; Malick, D. K.; Rabuck, A. D.; Raghavachari, K.; Foresman, J. B.; Ortiz, J. V.; Bui, Q.; Baboul, A. G.; Clifford, S.; Cioslowski, J.; Stefanov, B. B.; Liu, G.; Liashenko, A.; Piskorz, P.; Komaromi, I.; Martin, R. L.; Fox, D. J.; Keith, T.; Al-Laham, M. A.; Peng, C. Y.; Nanayakkara, A.; Challacombe, M.; W. Gill, P. M.; Johnson, B.; Chen, W.; Wong, M. W.; N.; Gonzalez, C.; Pople, J. A. *Gaussian 03*, Gaussian, Inc.: Wallingford, CT, 2004.
95. -50.08 kJ/mol for the T-T conformer and -30.75 kJ/mol for the H-T conformer.

96. Li, H., et al., *Isonicotinic Acid Molecular Films on Ag(111): 1. XPS and STM Studies of Orientational Domains*. Journal of Physical Chemistry C, 2007. **111**(5): p. 2102-2106.
97. Koczon, P., et al., *Experimental and theoretical IR and Raman spectra of picolinic, nicotinic and isonicotinic acids*. Journal of Molecular Structure, 2003. **655**: p. 89-95.
98. Cambridge Crystallographic Data Centre library for obtaining bond lengths and angles of isonicotinic acid was used to approximate the centre ring of 9-acridinecarboxylic acid (ACA) in its starting geometry.
99. For the starting geometry, H-bond lengths were approximately the same as those in the optimized Hartree-Fock calculation of head-to-tail dimers of isonicotinic acid.
100. Salem, L., *The Molecular Orbital Theory of Conjugated Systems*. 1966, New York: W. A. Benjamin, Inc.
101. An earlier model of the charge density change of consecutive atoms of an aromatic ring is directly proportional to the mutual polarizability  $\pi_{r,s}$  between atoms r and s, i.e.,  $\pi_{r,s} = \partial q_s / \partial \alpha_r$  where  $q_s$  is the total charge density along all s-atom occupied interactions and  $\alpha_r$  is the Coulomb integral of r-atom, and fluctuates in sign for consecutive atoms around the ring[Salem, 1996].
102. Cotton, F.A., E.V. Dikarev, and W.-Y. Wong, *W<sub>2</sub>Cl<sub>4</sub>(NR<sub>2</sub>)<sub>2</sub>(PR'<sub>3</sub>)<sub>2</sub> Molecules. 7. Preparation, Characterization, and Structures of W<sub>2</sub>Cl<sub>4</sub>(NHR)<sub>2</sub>(NH<sub>2</sub>R)<sub>2</sub> and W<sub>2</sub>Cl<sub>4</sub>(NHR)<sub>2</sub>(PMe<sub>3</sub>)<sub>2</sub> (R=sec-Butyl and Cyclohexyl) and <sup>31</sup>P{<sup>1</sup>H} NMR Studies of*

- Trans-to-Cis Isomerizations of  $W_2Cl_4(NHR)_2(PMe_3)_2$* . Inorganic Chemistry, 1997. **36**: p. 3268-3276.
103. Flacco, D.L., S.W. Hunt, and K.R. Leopold, *Microwave Investigation of Sulfuric Acid Monolayers*. Journal of the American Chemical Society, 2002. **124**(16): p. 4504-4511.
104. Hulme, A.T. and S.L. Price, *Toward the Prediction of Organic Hydrate Crystal Structures*. Journal of Chemical Theory and Computation, 2007. **3**: p. 1597-1608.
105. Nagy, P.I., et al., *Theoretical Conformational Analysis for Neurotransmitters in the Gas Phase and in Aqueous Solution. Norepinephrine*. Journal of the American Chemical Society, 2003. **125**(9): p. 2770-2785.
106. Evans, D., *Hierarchical Intermolecular Interaction Models of N-Heteroaromatic STM Adlayer Structures*, in *Chemical Physics*. 2007, University of Maryland: College Park, MD.
107. Lehn, J.-M., *Toward Self-Organization and Complex Matter*. Science, 2002. **295**: p. 2400-2402.
108. Gimzewski, J.K. and C. Joachim, *Nanoscale Science of Single Molecules Using Local Probes*. Science, 1999. **283**: p. 1683-1688.
109. Joachim, C., J.K. Gimzewski, and A. Aviram, *Electronics using hybrid-molecular and mono-molecular devices*. Nature, 2000. **408**: p. 541-548.
110. Collier, C.P., et al., *Electronically Configurable Molecular-Based Logic Gates*. Science, 1999. **285**: p. 391-394.

111. Hecht, S., *Welding, Organizing, and Planting Organic Molecules on Substrate Surfaces- Promising Approaches towards Nanoarchitectonics from the Bottom up*. *Angewandte Chemie International Edition*, 2003. **42**(1): p. 24-26.
112. De Feyter, S. and F.C. De Schryver, *Two-dimensional supramolecular self-assembly probed by scanning tunneling microscopy*. *Chemical Society Reviews*, 2003. **32**: p. 139-150.
113. Barth, J.W., et al., *Supramolecular architectures and nanostructures at metal surfaces*. *Applied Physics A: Materials Science & Processing*, 2003. **76**(5): p. 645-652.
114. Bain, C.D., et al., *Formation of monolayer films by the spontaneous assembly of organic thiols from solution onto gold*. *Journal of the American Chemical Society*, 1989. **111**(1): p. 321-335.
115. Batteas, J.D., et al., *Photoinduced charge separation in a porphyrin-tetraviologen supramolecular array*. *Journal of the American Chemical Society*, 1990. **112**(1): p. 126-133.
116. Scudiero, L., et al., *Scanning Tunneling Microscopy, Orbital-Mediated Tunneling Spectroscopy, and Ultraviolet Photoelectron Spectroscopy of Metal (II) Tetraphenylporphyrins Deposited from Vapor*. *Journal of the American Chemical Society*, 2001. **123**(17): p. 4073-4080.
117. Hipps, K.W. and U.J. Mazur, *Unoccupied Orbital Mediated Tunneling: Resonance-like Structures in the Tunneling Spectra of Polyacenes*. *Journal of Physical Chemistry*, 1994. **98**(23): p. 5824-5829.

118. Suzuki, T., et al., *Electronic structure of pentacene adsorbates on Au(111) surfaces*. Applied Physics Letters, 2003. **83**(21): p. 4342-4344.
119. Schroeder, P.G., et al., *Energy level alignment and two-dimensional structure of pentacene on Au(111) surfaces*. Journal of Applied Physics, 2002. **91**(5): p. 3010-3014.
120. Wagner, R.W., et al., *Molecular Optoelectronic Gates*. Journal of the American Chemical Society, 1996. **118**(16): p. 3996-3997.
121. Theobald, J.A., et al., *Controlling molecular deposition and layer structure with supramolecular surface assemblies*. Nature, 2003. **424**: p. 1029-1031.
122. Barth, J.W., et al., *Building Supramolecular Nanostructures at Surfaces by Hydrogen Bonding*. Angewandte Chemie International Edition, 2000. **39**(7): p. 1230-1234.
123. Dmitriev, A., et al., *Modular Assembly of Two-Dimensional Metal-Organic Coordination Networks at a Metal Surface*. Angewandte Chemie International Edition, 2003. **42**(23): p. 2670-2673.
124. Baski, A.A. and H. Fuchs, *Epitaxial growth of silver on mica as studied by AFM and STM*. Surface Science, 1994. **313**(3): p. 275-288.
125. Liao, H.M., R.N.S. Sodhi, and T.W. Coyle, *Surface composition of AlN powders studied by X-ray photoelectron spectroscopy and Bremsstrahlung-excited Auger electron spectroscopy*. Journal of Vacuum Science & Technology A- Vacuum Surfaces and Films, 1993. **11**(5): p. 2681-2686.
126. Bonello, J.M. and R.M. Lambert, *The structure and reactivity of quinoline overlayers and the adsorption geometry of lepidine on Pt {111}: model molecules*



- for chiral modifiers in enantioselective hydrogenation*. Surface Science, 2002. **498**(3): p. 212-228.
127. Gelius, U., et al., *Molecular Spectroscopy by Means of ESCA III. Carbon compounds*. Physica Scripta, 1970. **2**(1-2): p. 70-80.
128. Kowbel, W. and C.H. Shan, *The mechanism of fiber-matrix interactions in carbon-carbon composites*. Carbon, 1990. **28**(2-3): p. 287-299.
129. Schnadt, J., et al., *Structural study of adsorption of isonicotinic acid and related molecules on rutile TiO<sub>2</sub> (110) II. XPS*. Surface Science, 2003. **544**(1): p. 74-86.
130. Wühn, M., J. Weckesser, and C. Wöll, *Bonding and orientational ordering of long-chain carboxylic acids on Cu (111): investigations using x-ray absorption spectroscopy*. Langmuir, 2001. **17**(24): p. 7605-7612.
131. McQuarrie, D.A., *Statistical Mechanics*. 1976, New York: Harper & Row.
132. Kashiwagi, T., F. Du, and J.F. Douglas, *Nanoparticle networks reduce the flammability of polymer nanocomposites*. Nature Materials, 2005. **4**(12): p. 928.
133. Mossa, S., G. Ruocco, and M. Sampoli, *Molecular dynamics simulation of the fragile glass former orthoterphenyl: A flexible molecule model. II. Collective dynamics*. Physical Review E (Statistical, Nonlinear, and Soft Matter Physics), 2001. **64**(2): p. 021511.
134. Kalyuzhnyi, Y.V., *Thermodynamics of the polymer mean-spherical ideal chain approximation for a fluid of linear chain molecules*. Molecular Physics, 1998. **94**(4): p. 735.

135. Kalyuzhnyi, Y.V. and P.T. Cummings, *Multicomponent mixture of charged hard-sphere chain molecules in the polymer mean-spherical approximation*. Journal of Chemical Physics, 2001. **115**(1): p. 540.
136. Pickett, G.T. and K.S. Schweizer, *Liquid-state theory of anisotropic flexible polymer fluids*. Journal of Chemical Physics, 1999. **110**(14): p. 6597.
137. Chatterjee, A.P. and K.S. Schweizer, *Liquid-State Theory of Semidilute and Concentrated Polymer Solutions*. Macromolecules, 1998. **1998**(31): p. 2353.
138. Xiang, T. and B.D. Anderson, *Mean molecular potentials in a model lipid bilayer: A molecular dynamics simulation*. Journal of Chemical Physics, 1995. **103**(19): p. 8666.
139. Scalmani, G. and M.J. Fisch, *Geometries and properties of excited states in the gas phase and in solution: Theory and application of a time-dependent density functional theory polarizable continuum model*. Journal of Chemical Physics, 2006. **124**: p. 094107.
140. Nguyen, T.H., D.E. Hibbs, and S.T. Howard, *Conformations, Energies, and Intramolecular Hydrogen Bonds in Dicarboxylic Acids: Implications for the Design of Synthetic Dicarboxylic Acid Receptors*. Journal of Computational Chemistry, 2005. **26**(12): p. 1233.
141. Price, S.L., *Electrostatic forces in molecular interactions*, in *Molecular Interactions: From van der Waals to Strongly Bound Complexes*, S. Scheiner, Editor. 1997, John Wiley & Sons: West Sussex, U. K.
142. Roberts, R.M., et al., *Modern Experimental Organic Chemistry*. Fourth ed. 1985: Saunders College Publishing.

143. Bruker, *SMART and SAINT*. 1999, Madison, Wisconsin: Bruker AXS Inc.
144. Sheldrick, G.M., *SHELXL-97*. 1997: University of Gottingen, Germany.
145. Briggs, D., *Handbook of X-Ray and Ultraviolet Photoelectron Spectroscopy*. 1978, London, Great Britain: Heyden & Sons Ltd.